N° d'ordre : 004 - 2012 Année 2012

THESE DE L'UNIVERSITE DE LYON

Délivrée par

L'UNIVERSITE CLAUDE BERNARD LYON 1

ECOLE DOCTORALE

Interdisciplinaire Sciences-Santé

Pour l'obtention du

DIPLOME DE DOCTORAT

(Arrêté du 7 Août 2006)

Présentée et soutenue publiquement le 10 janvier 2012

par

Marilena Ioana MARINESCU

Multimodal characterization of superparamagnetic particles of iron oxide for inflammation imaging: Application to experimental cerebral ischemia.

JURY :

Dr Florence GAZEAU	Rapporteur
Dr Klaus PETRY	Rapporteur
Dr Emmanuel BARBIER	Rapporteur
Dr Anne DENCAUSSE	Examinateur
Dr Françoise PEYRIN	Examinateur
Dr Marlène Wiart	Examinateur
Dr Marie-Geneviève BLANCHIN	Directeur de thèse
Pr Yves BERTHEZENE	Directeur de thèse

UNIVERSITE CLAUDE BERNARD - LYON 1

Président de l'Université	**M. A. Bonmartin**
Vice-président du Conseil d'Administration	M. le Professeur G. Annat
Vice-président du Conseil des Etudes et de la Vie Universitaire	M. le Professeur D. Simon
Vice-président du Conseil Scientifique	M. le Professeur J-F. Mornex
Secrétaire Général	M. G. Gay

COMPOSANTES SANTE

Faculté de Médecine Lyon Est – Claude Bernard	Directeur : M. le Professeur J. Etienne
Faculté de Médecine et de Maïeutique Lyon Sud – Charles Mérieux	Directeur : M. le Professeur F-N. Gilly
UFR d'Odontologie	Directeur : M. le Professeur D. Bourgeois
Institut des Sciences Pharmaceutiques et Biologiques	Directeur : M. le Professeur F. Locher
Institut des Sciences et Techniques de la Réadaptation	Directeur : M. le Professeur Y. Matillon
Département de formation et Centre de Recherche en Biologie Humaine	Directeur : M. le Professeur P. Farge

COMPOSANTES ET DEPARTEMENTS DE SCIENCES ET TECHNOLOGIE

Faculté des Sciences et Technologies	Directeur : M. le Professeur F. De Marchi
Département Biologie	Directeur : M. le Professeur F. Fleury
Département Chimie Biochimie	Directeur : Mme le Professeur H. Parrot
Département GEP	Directeur : M. N. Siauve
Département Informatique	Directeur : M. le Professeur S. Akkouche
Département Mathématiques	Directeur : M. le Professeur A. Goldman
Département Mécanique	Directeur : M. le Professeur H. Ben Hadid
Département Physique	Directeur : Mme S. Fleck
Département Sciences de la Terre	Directeur : Mme le Professeur I. Daniel
UFR Sciences et Techniques des Activités Physiques et Sportives	Directeur : M. C. Collignon
Observatoire de Lyon	Directeur : M. B. Guiderdoni
Ecole Polytechnique Universitaire de Lyon 1	Directeur : M. P. Fournier
Ecole Supérieure de Chimie Physique Electronique	Directeur : M. G. Pignault
Institut Universitaire de Technologie de Lyon 1	Directeur : M. le Professeur C. Coulet
Institut de Science Financière et d'Assurances	Directeur : M. le Professeur J-C. Augros
Institut Universitaire de Formation des Maîtres	Directeur : M. R. Bernard

Remerciements

Je remercie chaleureusement les Professeurs Isabelle Magnin et Didier Revel pour m'avoir accueilli au sein de leur laboratoire et pour avoir suivi avec intérêt mon travail au cours de ces quatre années. Qu'ils trouvent ici l'expression de ma profonde reconnaissance.

Je suis très heureuse que Madame Florence Gazeau, directrice de recherche CNRS, ait accepté d'être rapporteur de ce travail et je l'en remercie chaleureusement. Je suis particulièrement reconnaissante à Monsieur Klaus Petry, directeur de recherche INSERM, d'avoir accepté d'être rapporteur de cette thèse. Qu'il trouve ici l'expression de mes sincères remerciements. Je remercie vivement Monsieur Emmanuel Barbier, directeur de recherche INSERM, pour avoir accepté d'être rapporteur de ce travail. Je remercie par ailleurs chaleureusement Madame Françoise Peyrin, directrice de recherche INSERM, pour avoir accepté de participer au jury. Je suis enfin particulièrement honoré de compter Madame Anne Dencausse parmi les juges de ce travail et je l'en remercie sincèrement.

J'exprime toute ma gratitude aux Professeur Yves Berthezène et Docteur Marlène Wiart qui m'ont dirigée et conseillée avec beaucoup de patience tout au long de cette thèse. Je remercie particulièrement Marlène Wiart pour m'avoir montré ce qu'était le monde de la recherche et pour m'avoir fait profiter de sa grande expérience dans le domaine de l'IRM. Ce manuscrit sous sa forme actuelle doit beaucoup à ses remarques judicieuses.

J'exprime mes remerciements chaleureux à Madame Marie-Geneviève BLANCHIN, directrice de recherche CNRS, pour avoir co-encadré ce travail, pour m'avoir accueilli au sein de son équipe, d'abord en tant que stagiaire, puis comme doctorante.

Je salue le Professeur Norbert Nighoghossian pour m'avoir accueilli au sein de son équipe et pour m'avoir fait partager son savoir en Neurologie.

J'exprime ici ma profonde reconnaissance à Monsieur Sorin Ciuca pour m'avoir conseillé et encouragé à m'orienter vers la recherche. Qu'il trouve ici le témoignage de ma profonde gratitude.

Je tiens à remercier mes co-thésards Anne Durand, Adrien Riou et Tae-Hee Cho pour tout le travail accompli ensemble et pour avoir réussi à créer une super ambiance au sein et en dehors du labo. Un grand merci à Fabien Chauveau pour sa disponibilité et son aide durant ces années de doctorat.

Je remercie également tous ceux qui m'ont soutenu et m'ont fait partager leur bonne humeur durant leur séjour au B13, au CERMEP et au LPMCN : Adrian, Bénédicte, Cyril, Dragos, Jean-Baptiste, Laure, Monica, Radu, Salem, et tout ceux que j'oublie dans cette liste non exhaustive.

Je dédie cette thèse

A mes parents, Maria et Vidor,
qui m'ont donné la chance de réaliser ce parcours et qui ont toujours cru en moi
pour leur amour, leur soutien et leurs encouragements dans mes moments de doute

A Horia,
pour son soutien et son amour, qui m'aident à avancer,
à accomplir des projets, à devenir une meilleure personne.

Table of contents

French summary 7

Chapter I 12

Ischemic Stroke 12

I. Clinical and epidemiological aspects 13

I.1 Clinical aspects of ischemic stroke 13

I.2 Epidemiological aspects of stroke 13

II. Physiopathology of ischemic stroke 14

II.1 Introduction 14

II.2 Ischemic Penumbra 18

III. Mechanisms of cell death in cerebral ischemia 25

IV. Approved and potential treatment of ischemic stroke 25

IV.1 Reperfusion with tissue plasminogen activator 26

IV.2 Neuroprotective drugs 27

Chapter II 31

Post-Ischemic neuroinflammation imaging using USPIO 31

I. Inflammatory response in stroke 32

I.1 Cells of the mononuclear phagocyte system 32

I.2 Inflammatory Mechanism 36

I.3 Post-Ischemic inflammatory reaction 37

II. Superparamagnetic iron oxide (SPIO) contrast agent 44

II.1 SPIOs classification 44

II.2 USPIO Synthesis 46

II.3 USPIOs coating 47

II.4 USPIOs metabolism 48

II.4 USPIOs effects on MR signal 49

II.5 Cell labeling with USPIO 50

III. USPIO dedicated imaging techniques 53

III.1 USPIO-enhanced MRI of post-ischemic neuroinflammation 53

III.2 USPIO detection by Synchrotron Radiation Micro-Computed Tomography (SR-µCT) 59

III.3 USPIO detection by Transmission Electron Microscopy (TEM) 62

Chapter III **67**

Monitoring therapeutic effects in experimental stroke by serial USPIO-enhanced MRI **67**

I. Introduction **68**

II. Materials and methods **69**

III. Results **74**

IV. Discussion **81**

V. Conclusion **84**

Chapter IV **85**

Detection of iron oxide nanoparticles in the brain using synchrotron radiation X-ray micro-computed tomography **85**

I. Introduction **86**

II. Materials and Methods **86**

III. Results **91**

IV. Discussion **100**

Chapter V **102**

TEM study of long term spleen storage of P904 ..... **102**

I. Introduction **103**

II. Materials and methods **103**

III. Results **105**

IV. Discussion **109**

Conclusion and perspectives **111**

Publications and Communications **128**

Articles in journals **129**

Conference Proceedings **130**

Curriculum Vitae **131**

French summary
Résumé en français

Les accidents vasculaires cérébraux représentent la troisième cause de mortalité et la première cause de handicap acquis chez l'adulte dans les pays industrialisés. La plupart des AVC ont une origine ischémique (88% des cas). L'ischémie cérébrale déclenche une réponse inflammatoire qui pourrait contribuer de manière significative aux dommages neurologiques. Cette réaction inflammatoire est dominée par les cellules mononuclées phagocytaires : la microglie, cellules immunocompétentes du parenchyme cérébral, et les macrophages qui dérivent du sang et infiltrent le tissu cérébral lésé.

L'imagerie par résonance magnétique (IRM) couplée à l'administration intraveineuse des nanoparticules d'oxyde de fer superparamagnétiques (ultrasmall superparamagnetic particles of iron oxides, USPIO) permet de détecter l'activité phagocytaire des macrophages de manière non invasive. Cette technique pourrait être transposable dans la clinique, car certains USPIOs peuvent être administrés aux patients. Plusieurs études menées chez le petit animal ont montré que cette approche permettait d'appréhender la réponse inflammatoire suite à une ischémie cérébrale. Cependant, aucune équipe n'a à ce jour étudié le potentiel de cette approche pour le suivi d'un traitement anti-inflammatoire.

Dans ce contexte, l'objectif de la thèse était de **démontrer la faisabilité de monitorer les effets d'un traitement anti-inflammatoire avec les nanoparticules d'oxyde de Fer comme marqueurs de l'activité phagocytaire macrophagique suite à une ischémie cérébrale chez la souris**. Pour cela, nous avons réalisé un **suivi longitudinal en IRM** d'un groupe de souris traité avec la minocycline (un antibiotiques aux propriétés anti-inflammatoires) et d'un groupe contrôle traité avec du sérum physiologique. Nous avons montré une diminution significative de l'étendue des signaux RM liés aux USPIO (mesurée par seuillage automatique des cartographies R2) dans le groupe traité. En revanche, la valeur quantitative du R2 ne variait pas entre les deux groupes. L'évaluation post-mortem en immunohistologie et relaxométrie a permis de confirmer les résultats obtenus en IRM.

L'IRM est une technique très sensible pour la détection du Fer, mais présente deux inconvénients majeurs : d'une part, la localisation précise des USPIO est rendue difficile par les effets de « blooming » (disparition du signal RM à distance de l'agent de contraste) et d'autre part, la quantification du Fer est perturbée par la non-linéarité de la relation entre la concentration de Fer et le signal RM. Nous avons donc proposé de compléter l'approche IRM par une technique inédite à notre connaissance dans le domaine de l'imagerie cérébrale des USPIO : la **tomographie par rayonnement Synchrotron**. Nous présentons ici les tous

premiers résultats montrant la faisabilité de l'approche, ainsi qu'une étude comparée de la sensibilité des deux techniques pour la détection des USPIO dans le cerveau.

Enfin, l'interprétation du signal RM lié aux USPIOs reste un sujet à controverse, notamment en raison d'une connaissance incomplète de leur devenir après ingestion par les macrophages. Dans la dernière partie de notre travail, nous rapportons nos résultats concernant **la biotransformation des USPIOs** dans la rate de la souris dans les 40 premiers jours suivant leur injection intraveineuse. Ces résultats ont été obtenus en **microscopie électronique par transmission (MET)**, qui permet grâce aux méthodes de diffraction de différentier le Fer administré sous forme de maghémite du Fer recyclé dans la ferritine.

Cette thèse a été réalisée au laboratoire Creatis (UMR CNRS 5220, U1044 Inserm, Université Lyon 1, INSA de Lyon), sous la direction du Pr Yves Berthezène et de Marlène Wiart dans le cadre du projet ANR TecSan 2007 INFLAM (INFLAMmation in brain and vessels with iron nanoparticles and cell trafficking: a multi-scale approach of tissue microenvironment, iron nanostructure and iron biotransformations). Une partie des travaux expérimentaux a été réalisée au Laboratoire de Physique de la Matière Condensée et Nanostructures (UMR CNRS 5586, Université Lyon 1), sous la direction du Pr Marie-Geneviève Blanchin.

Organisation de la thèse

Cette thèse débute par deux chapitres introductifs : le premier sur l'ischémie cérébrale et le second sur les techniques d'imagerie dédiées à l'investigation de l'inflammation post-ischémique à l'aide des USPIO. Ces deux chapitres de rappels bibliographiques sont suivis par trois chapitres présentant le travail de recherche effectué pendant la thèse.

L'étude présentée dans le chapitre 3 teste l'hypothèse selon laquelle l'IRM couplée à l'injection des USPIO permettrait de suivre les effets d'un traitement anti-inflammatoire après une ischémie cérébrale chez la souris.

Trois doses de minocycline (un antibiotique avec des propriétés anti-inflammatoires) (N = 12) ou de sérum physiologique (N = 12) ont été administrées par voie intrapéritonéale une fois toutes les 3 heures en commençant 5 minutes après l'occlusion permanente de l'artère cérébrale moyenne chez la souris. L'agent de contraste P904 (Guerbet, Aulnay-Sous-Bois, France) a été administré par voie intraveineuse (2 mmol Fe / kg) 5 heures après la chirurgie. Les souris ont été suivies de manière longitudinale en IRM à J0 (pré-contraste), J1 et J2 (post-contraste). A la fin du protocole IRM, les cerveaux ont été prélevés pour l'examen immunohistologique et le dosage du fer. Comme attendu, le traitement par la minocycline a diminué de manière significative: (1) la taille de la lésion ischémique, (2) la perméabilité aux IgG de la barrière hémato-encéphalique et (3) le marquage F4/80 des macrophages. La co-localisation du double marquage anti-F4/80 et bleu de Perls suggérait l'internalisation des USPIO par les macrophages à J2 post-ischémie. Deux paramètres ont été testés pour évaluer l'apport de l'IRM réhaussée avec les USPIO pour le suivi *in vivo* des effets de la minocycline : l'étendue de la prise de contraste (mesurée par seuillage des cartographies R2) et les variations de R2 dans le temps. L'étendue des hypersignaux R2 ($> 35\ s^{-1}$) induits par les USPIO à J1 et J2 post-ischémie était significativement réduite dans le groupe traité (minocycline) par rapport au groupe contrôle. En revanche, aucune différence significative entre les deux groupes n'a été détectée avec la mesure du R2 à J1 et J2. Cette étude a montré que les USPIOs pouvaient être utilisés comme biomarqueurs pour la détection des effets thérapeutiques dans un AVC expérimental.

Le chapitre 4 présente une étude de faisabilité d'utilisation de la tomographie par rayonnement synchrotron (Synchrotron Radiation micro-Computed Tomography, SR-μCT) pour fournir une cartographie de la distribution des USPIOs dans le cerveau de la souris.
Quatre types d'échantillons ont été imagés : (i) des fantômes avec différentes concentrations de P904, (ii) des cerveaux de souris ayant reçu des injections stéréotaxiques de P904 dans une gamme de concentration (n=10), (iii) des cerveaux de souris ayant reçu des injections stéréotaxiques de macrophages marqués avec les NPMA (n=6), (iv) des cerveau de souris présentant une ischémie cérébrale et injectés par voie intraveineuse avec du P904 (n = 8).L'imagerie des fantômes a permis d'établir la limite de détection de la concentration en Fer de la technique. Les images en contraste de phase ont permis une localisation plus précise qu'en IRM des USPIO à l'égard de la topographie du cerveau pour les échantillons avec injections stéréotaxiques. En ce qui concerne le modèle animal d'ischémie, la SR micro-CT en contraste de phase s'est révélée moins sensible que l'IRM, mais a permis de détecter toutes les concentrations, y compris les plus faibles. La tomographie par rayonnement Synchrotron présente une résolution spatiale dans le plan dix fois supérieure à l'IRM (8 μm vs 80 μm) pour un temps d'acquisition raisonnable (20 minutes). L'étude quantitative a été plus difficile, notamment en raison de difficultés techniques liées aux injections stéréotaxiques. Néanmoins, le couplage des deux techniques apparaît prometteur et des travaux futurs devraient permettre d'améliorer l'acquisition et le post-traitement des images de SR micro-CT.

Le chapitre 5 présente une étude en microscopie électronique en transmission (MET) sur des échantillons de rate de souris athéromateuse (ApoE-/-). Quatre animaux ont reçu une injection intraveineuse de P904 à la dose de 1000 μmol Fe/kg. Une série d'échantillons de rate a été prélevée et préparée pour la visualisation en MET 3h, 2 jours, 30 jours et 40 jours après. Des agglomérations des nanoparticules dans des phagolysosomes ont été trouvées à tous les temps. A partir de J2 après injection, des zones denses aux électrons avec un motif de diffraction correspondant à la maghémite et des zones moins denses aux électrons avec un digramme de diffraction moins définie coexistent dans nombreux lysosomes. Ces résultats suggèrent une biotransformation continue locale des nanoparticules, le plus probablement dans la ferritine.

Chapter I

Ischemic Stroke

I. Clinical and epidemiological aspects

I.1 Clinical aspects of ischemic stroke

According to WHO, stroke is defined as rapidly developing clinical signs of focal (at times global) disturbance of cerebral function, lasting more than 24 h or leading to death with no apparent cause other than that of vascular origin.[1]

Cerebral ischemia results from the interruption or reduction of oxygen supply, due to a decrease in cerebral blood flow and/or more rarely with hypoxia. We distinguish schematically ischemic stroke, a consequence of focal ischemia by occlusion of one or more cerebral arteries, and hypoxia-anoxia overall. Neuronal cell death is caused by a series of pathophysiological events, called ischemic cascade (see II.1), like energy failure, excitotoxicity, oxidative stress, inflammation, apoptosis.

I.2 Epidemiological aspects of stroke

Of all strokes, 87% are ischemic, 10% are intracerebral hemorrhage and 3% are subarachnoid hemorrhage strokes.[2] In Western countries, stroke represents the leading cause of disability, the second cause of dementia[3] and the third cause of death.[4, 5] An estimated 17 million people die of cardiovascular diseases (CVD), particularly heart attacks and strokes, every year (Figure 1). Nearly three-quarters of all strokes occur in people over the age of 65. The risk of having a stroke more than doubles each decade after the age of 55.

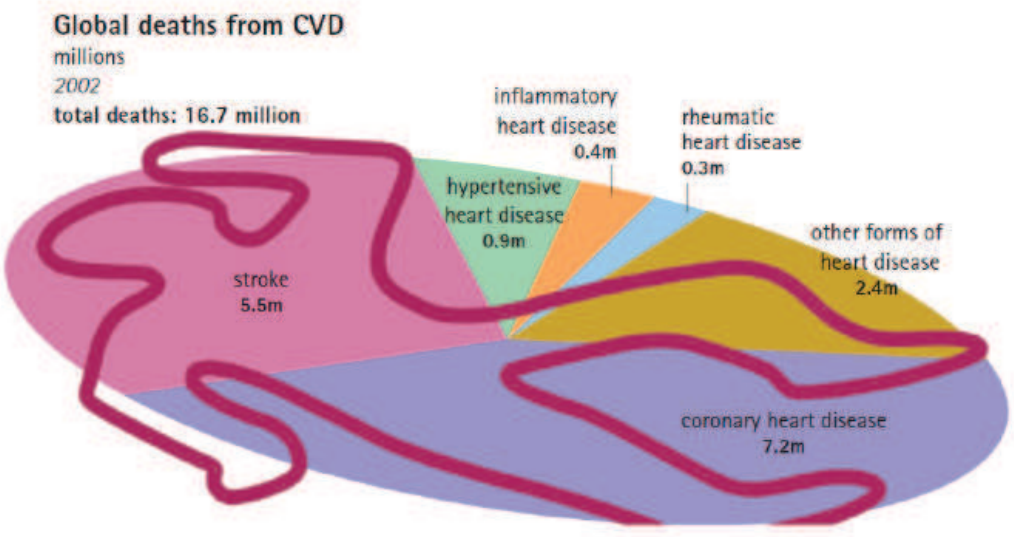


Figure1. Specific mortality of vascular disease in 2002. Strokes account for about one third of overall cardiovascular mortality. World Health Organization. The Atlas of Heart Disease and Stroke, 2006.

- *Incidence (number of new cases)*

The worldwide annual stroke incidence has been estimated at 9.0 million in the year 2004, of which 2.0 million occur in Europe *(WHO 2008)*, and 0.6 in the USA.[2]

- *Mortality*

Stroke caused 5.7 million deaths worldwide in the year 2004, 9.7% of all deaths (58.8 million), and second only to all cancers together (7.4 million, 12.6%) and ischemic heart disease (7.2 million; 12.2%) *(WHO 2008)*. Age-adjusted mortality rates vary by a factor of 10 among countries.[6] Stroke causes 1/18 (5.6%) of all deaths in the USA. A 15% fall in absolute number of deaths, and a 45% decrease in age-adjusted death rate have been observed from 1997 to 2007.[2]

- *Prevalence (number of total cases)*

The worldwide prevalence of stroke has been estimated at 30.7 million in the year 2004, and 12.6 million are living with moderate to severe disability. A total of 9.6 million stroke survivors live in Europe *(WHO 2008)*. The prevalence of stroke in the USA has been estimated as 7 million stroke patients, 3% of the population aged 20 or over.[2] This figure is expected to increase to 4% by the year 2030.[7]

- *Cost*

Cost of stroke patients has been estimated to constitute between 1.6% and 6.9% of total healthcare costs in developed countries, with the latest estimates at around 3% *(Evers et al. 2004)*. The direct medical costs of stroke in the USA are estimated at US$ 28.3 Billion in the year 2010, and this is expected to more than triple to US$ 95.6 Billion by the year 2030 (2008 currency). During the same time, the indirect costs of stroke are estimated to increase from US$ 25.6 Billion to 44.4 Billion.[7]

II. Physiopathology of ischemic stroke

II.1 Introduction

The main mechanisms of vessel occlusion that result in ischemic stroke are embolism (clot or other material that travels from another part of the body to the brain or neck) and/or in situ thrombosis (blood clot that forms in a blood vessel of the brain or neck around atherosclerotic plaques). An embolus is most frequently a thrombus, but it can also be a number of other substances including fat (e.g., from bone marrow in a broken bone), air or cancer cells. An ischemic stroke may also be caused by stenosis which is a severe narrowing

of an artery in or leading to the brain. A complete mechanistic and topographic classification of cerebral infarcts affecting cerebral hemispheres is represented in Figure 2. The territory of the middle cerebral artery (MCA or Sylvian) is most often touched (55 to 75% of hemispheric stroke), and often in isolation (55%). The MCA infarction can affect the whole (total MCA stroke) or part of the territory (MCA stroke superficial or deep). **The frequency of clinical MCA stroke explains the majority of MCA occlusion animal models. This model of focal cerebral ischemia was used in this work.**

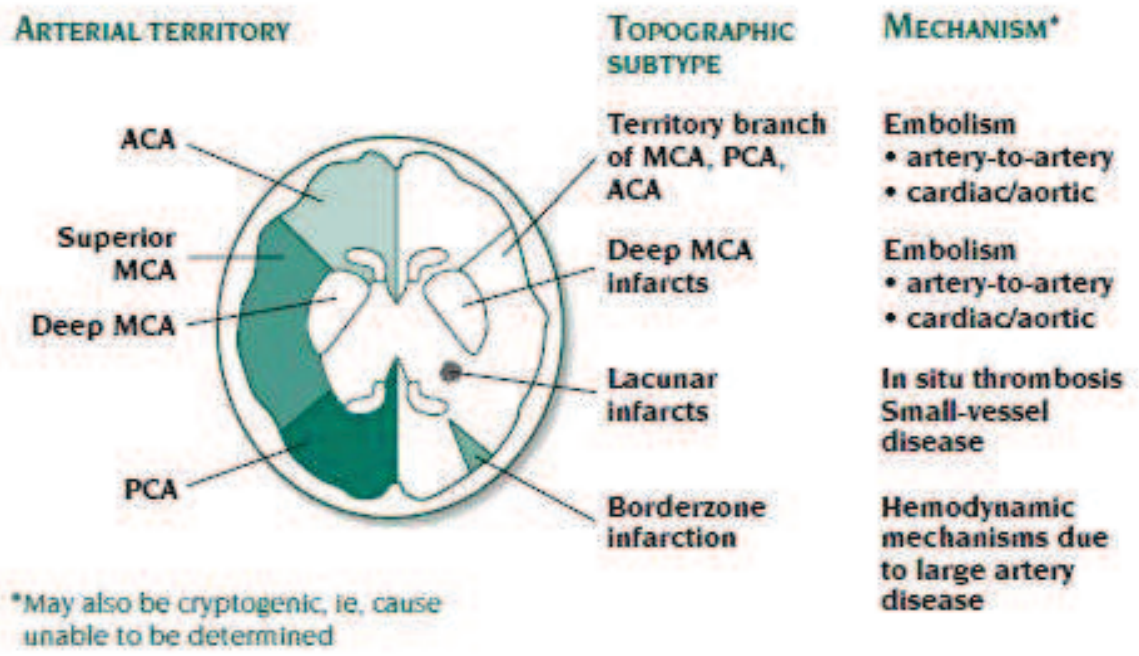


Figure 2. Topographic classification of cerebral infarcts affecting cerebral hemispheres. ACA- anterior cerebral artery, PCA- posterior cerebral artery, MCA- middle cerebral artery. Reproduced from GA. Donnan, Dialogues in Cardiovascular Medicine, 2003

Hemodynamic parameters

- Perfusion or regional cerebral blood flow (rCBF)

In physiology, perfusion is the process of nutritive delivery of arterial blood to a capillary bed in the biological tissue. Perfusion measurement techniques based on radioactive tracers such as oxygen-15 marked water ($H_2{}^{15}O$) measure the regional blood flow, which led to the identification of perfusion to the blood flow in the tissue. The concept of perfusion sometimes extends to other parameters such as the exchange between blood and tissue, the use of glucose

by the cells or their oxygen consumption. These parameters are obviously related, but they should not be confused with perfusion.

CBF is defined as the volume of blood moving through a given unit volume of brain per unit time. CBF has units of milliliters of blood per 100 grams of brain tissue per minute (ml/100g/min). The mean value of blood flow in the brain is about 50 ml/100g/min.

- *Regional cerebral blood volume (rCBV)*

It represents the volume of tissue occupied by blood, expressed in ml/100 g of tissue. The mean regional blood volume is 5 ml/100 g of tissue. rCBV is greater in gray matter than in white matter.

- *Oxygen consumption (CMRO2)*

Cerebral oxygen consumption represents the volume of oxygen extracted from the blood in a given time per mass unit of tissue (in ml/100 g tissue / min). On average in the healthy brain the CMRO2 represents 3 ml/100 g tissue / min. This parameter represents the cellular respiration (mainly that of neurons).

- *The oxygen extraction fraction (OEF)*

The oxygen extraction ratio is given by the difference between the arterial and venous oxygen reported to the amount of arterial oxygen expressed as a percentage. All regions of brain extract the same fraction of the arterial O_2, about 40%. The rOEF expresses the adequacy or inadequacy between the circulatory oxygen supply and the tissue energy requirement.

- *Mean transit time (MTT)*

The mean transit time represents the mean time required for blood to pass through the tissue, from the arterial input to the venous output. The mean transit time value in the brain is about 6 seconds. MTT is defined as the ratio of cerebral blood volume to cerebral blood flow (CBV/CBF).

This hemodynamic parameters can be evaluated using several techniques such as: i) *SPECT- Single photon emission computed tomography* (this technique relies on the injection of a radioactive gamma isotope (tracer) that binds to the target organ, allowing a selective review of regional function); ii) *PET- Positron Emission Tomography* (uses of radioactive isotopes of elements that are found naturally in most molecules: ^{11}C, ^{15}O, ^{13}N, ^{18}F) ; iii) *CT- computed*

tomography (based on the measurement of X-ray attenuation by biological tissue) using dynamic imaging during first pass of a iodinated contrast agent; iv) *Transcranial Doppler Ultrasound* (using ultrasounds to instantly detect and quatify the blood flow); v) *MRI* (non-invasive imaging method with a high spatial resolution) using dynamic imaging during first pass of a paramagnetic (or superparamagnetic) contrast agent.

Importance of cerebral blood flow (CBF)

Deficiency in cerebral blood flow (CBF), caused by blockage of an artery that supplies blood to the brain, leads to reduced intake of oxygen, glucose and to an accumulation of brain metabolites ending in an ischemic stroke.[8]

Normal CBF in humans is approximately 50 to 60 ml/100g/min and varies depending on region (20 ml/100g/min in white matter, 70 ml/100g/min in grey matter). Experimental studies on cats and baboons allowed to establish the existence of ischemia thresholds.[9] Certain functional perturbations occur once blood flow decreases below these thresholds (see Table 1). Critical reduction in CBF (to 40% of normal) deprives brain of substrates (glucose and oxygen), and within minutes the energy demands exceed the capacity of the brain to generate adenosine triphosphate (ATP). There is tissue acidosis due to lactate excess, which triggers off a failure of ionic pumps, resulting in the generation of free radicals, neurotransmitters (glutamate) and inflammatory mediators. When the CBF is reduced at 30%, neurons become electrically silent but nonetheless viable. In case of normal CBF restoration, neurons recover and ensure new electrical activity. The concept of ischemic penumbra (chapter 1, II.2) is based on this potential neuron recovery. It has been termed 'penumbra' by analogy with the partly illuminated area around the complete shadow of the moon at full eclipse.

CBF less than 20% of normal (8-10 ml/100g/min) leads to irreversibly damaged tissue responsible for glial and neuronal death.[10] The severity, duration, and speed of CBF reduction will decide the degree of energetic and structural alteration.

	Reduction	Functional Perturbations
CBF	50%	• Reduction of protein synthesis
	40%	• Anaerobic glycolysis with lactate production • Reduction in adenosine triphosphate (ATP) production • Tissue acidosis due to lactate excess • Ionic pumps failure resulting in free radicals and neurotransmitters (glutamate) release
	40% - 30%	• Electrophysiological activity is compromised
	30%	**Threshold of electrical failure** • Neurons are electrically silent but nonetheless viable forming the so called penumbra
	Reperfusion → Potential recovery of neurons and electrical activity restart	
	20%	**Threshold of membrane failure** • Sodium pump function is impaired by neuronal energy failure • Extracellular potassium increase and intracellular penetration of sodium, calcium and chlorine • Intracellular edema

Table 1. Functional perturbation of the brain produced by CBF decrease

II.2 Ischemic Penumbra

II.2.1 Concept

It has been now 30 years since the ischemic penumbra was first defined in stroke. It was originally described by Astrup in 1981 as a portion of the ischemic zone with reduced cerebral blood flow (CBF) with absent electrical activity but preserved ion homeostasis and transmembrane electrical potentials. Since then it underwent several modifications with a particular focus on energy metabolism, CBF thresholds and protein synthesis.[11] Another definition of ischemic penumbra is: functionally compromised but structurally intact tissue surrounding a core of infarcted tissue. One widely accepted definition for penumbra describes the area as ischemic tissue potentially destined for infarction but not yet irreversibly injured and the target of acute therapies. The ischemic brain tissue surrounding the penumbra is represented in Figure 3.

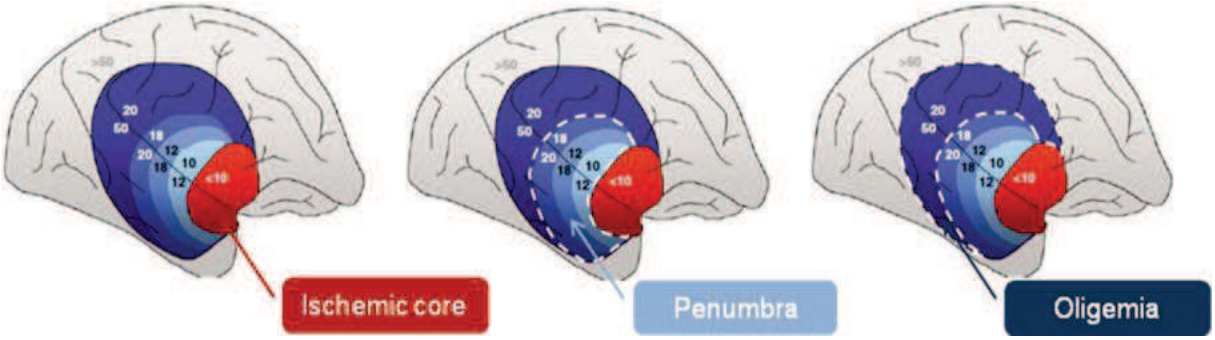


Figure 3. Representation of penumbra in an ischemic baboon brain with CBF values according to different regions.
Adapted from Moustafa and Baron, 2008

The ischemic penumbra is a dynamic process. It exists for a short period even in the center of ischemia from which the conversion into irreversible necrosis propagates over time to the neighboring tissue.[12] Some residual perfusion persists in the ischemic area dependent on collateral vessels and local perfusion pressures.[9] Thus the penumbra area may remain viable for several hours after an ischemic event making it a potential target for therapeutic agents for reperfusion and/or neuroprotection (see chapter I, III). Without timely institution of either reperfusion or pharmacologic intervention the penumbra would inevitably transform into an infarcted area (Figure 4).

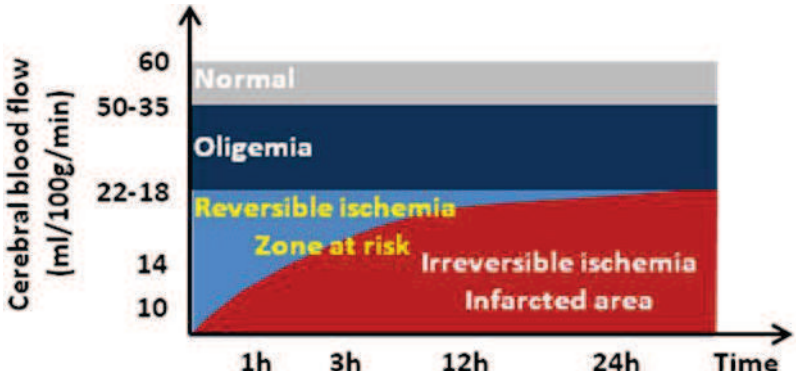


Figure 4. Representation of penumbra: time-space dependence

The future of the area at risk is unpredictable and depends primarily on early restoration of cerebral perfusion, thus limiting the consequences of the ischemic process (oxidative damage, inflammation, apoptosis). Its evolution is influenced by several factors: heterogeneity of stroke, occlusion sites, role of collateral circulation, tolerance to ischemia depending on the tissue (gray matter versus white matter), which varies from one individual to another and from

one region to another, genetic factors, level of expression of genes involved in cerebral ischemia.[13]

During the past 20 years, positron emission tomography (PET) and magnetic resonance imaging (MRI) have helped to identify the ischemic penumbra. However, the results obtained by these methods are still debated and failed to find the thresholds of ischemia within the original definition that came from the experimental data.

II.2.2 Methods of evaluation

II.2.2.1 Positron Emission Tomography

PET imaging starts with the injection of an active tracer, a biological molecule which carries a positron emitting isotope, for example ^{11}C or ^{18}F. Within minutes, the molecule accumulates in an area of the body for which it has an affinity. The radioactive nuclei decay by emission of positrons. These positrons collide now with free electrons, usually no farther away than 1 mm from the point of emission. The collision results in a conversion from matter to energy and emits two high energy gamma rays in opposite directions. These gamma rays can be detected with an array of detectors which surrounds the patient. PET neuroimaging is based on an assumption that areas of high radioactivity are associated with brain activity.

PET is theoretically the most appropriate tool to study the ischemic penumbra. It is limited by a poor spatial resolution (voxel size: 250 to 1000 mm^3) but provides precise quantification of metabolic and hemodynamic parameters (CBF, CBV, CMRO2 and OEF) within the infarct and the infarct periphery.

The penumbra is characterized by:[10]

• CBF between 7-8.5 ml/100g/min and 17-22 ml/100g/min

• a relative preservation of oxygen consumption (CMRO2)

• an increase in oxygen extraction rate (> 70%) (Figure 5).

Based on validated thresholds for CBF, OEF, CMRO2 or flumazenil (FMZ) uptake, PET classifies the abnormal brain tissue into four subtypes: (i) the core (defined as the irreversibly damaged tissue already present at time of imaging); (ii) the penumbra (defined as that severely hypoperfused tissue at risk of, but that can still be saved from, infarction); (iii) the oligemia (defined as mildly hypoperfused and not at-risk of infarction under normal circumstances); and (iv) the hyperperfused tissue (defined as that tissue with CBF higher than that in the contralateral homologous tissue, and taken to represent effective reperfusion).[14]

Furlan et al. were the first to validate the identification of the penumbra with PET.[15] The total volume of the penumbra was correlated with initial neurological deficit; the volume of the penumbra escaping from the final infarct, 2 months after, showed a close correlation with the final neurological recovery. The use of FMZ labeled with ^{11}C, benzodiazepine central ligand receptor, has contributed to the characterization of tissue viability.[16] The failure of FMZ uptake was predictive of progression to infarction in the penumbra.

Limits of the method

The limited number of PET machines, the complexity, cost and duration of tests, the lack of immediate data, the radiation, and the need for arterial catheterization limit the routinely application of PET in the emergency treatment.

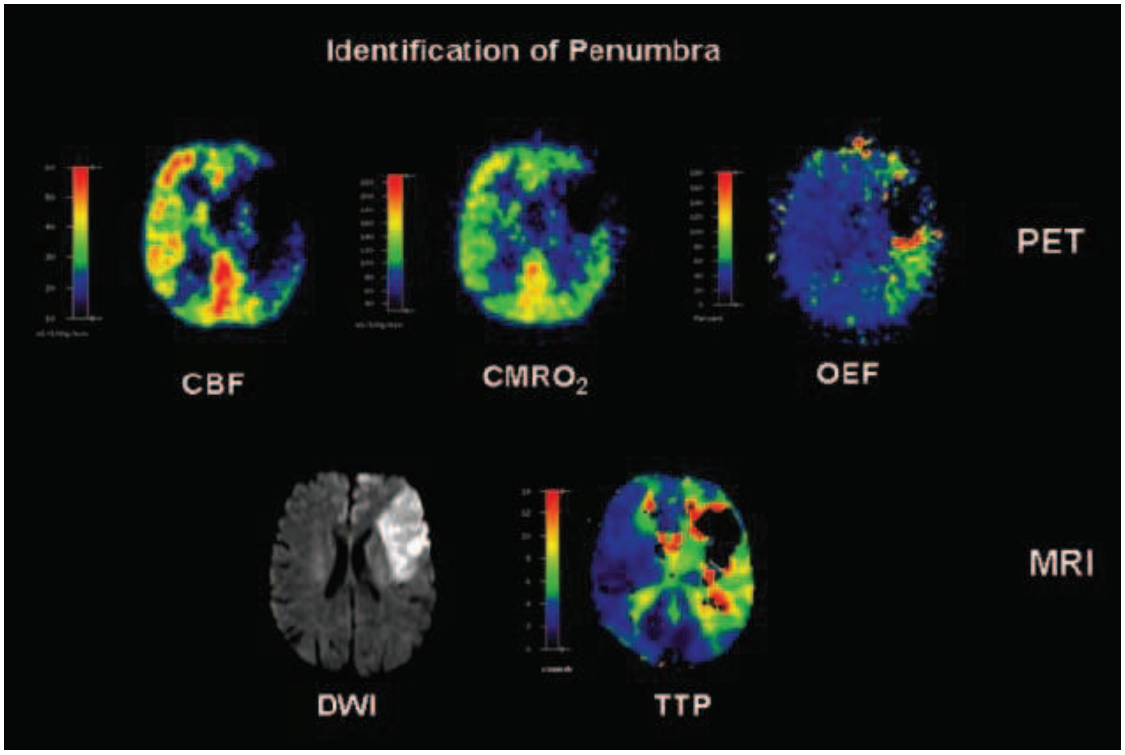


Figure 5. Imaging of the penumbra with PET and MRI. The penumbra is characterized by hypoperfusion (CBF), preserved $CMRO_2$, and elevated OEF. These findings correspond grossly to the mismatch between DWI hyperintensity and a TTP delay of 4 seconds compared with the unaffected hemisphere. Reproduced from Heiss et al.,Stroke, 2004

II.2.2.2 Magnetic Resonance Imaging

The MR examination is performed in the presence of a magnetic field. The proton spins of the water molecules will be aligned on the direction of this field and create a macroscopic magnetization. By applying one or more radio-frequency pulses, the net

macroscopic magnetization of proton spins is perturbed out of its alignment parallel to the applied field. The MR image is obtained by collecting the signal of the relaxation back to the initial state using a radiofrequency coil. The relaxation back to equilibrium of the magnetization is governed by two exponential time constants: T1, longitudinal relaxation time, for the component along the *z* axis, and T2 the transverse relaxation time, for the component perpendicular to *z*. Thus, tissue components with short T1 values will be associated with higher signal intensities compared to those components that have longer T1 values on T1-weighted MR images. As for the other time constant, short T2 values are associated with low signal intensities on T2-weighted MR images, since the magnetization available for detection is smaller. In the presence of magnetic inhomogeneities the transverse relaxation is governed by a shorter time constant, T2* (called the apparent transverse relaxation time). The contrast of an MR image can be related to one of the time constants or to the proton density of tissue components. This is called image weighting and is obtained through manipulation of the MR sequence parameters such as the repetition time (TR) and echo time (TE).

Multimodal MRI sequences, including diffusion and perfusion weighted images (DWI and PWI), aims to apprehend the profile of bioenergy and hemodynamic ischemic stroke.[17-22]

- Diffusion weighted imaging (DWI)

DWI is based on the microscopic movement (Brownian motion) of water molecules. In normal diffusion, water protons move between the dephasing and the rephasing gradients, resulting in signal attenuation. If there is restricted diffusion, such as in acute infarction, the signal attenuation is decreased, resulting in hyperintensity on diffusion-weighted images. The degree of diffusion-weighting is called the b value. If the b value is zero, there is no diffusion weighting and the images are similar to T2-weighted images. Conversely, if the b value is high, there is heavy diffusion-weighting. Diffusion-weighted images are a combination of diffusion information and T2 signal intensity. This double phenomenon can be eliminated by generating an apparent diffusion coefficient (ADC) map. [23]

The apparent diffusion coefficient is a measure of water diffusion and is calculated by differences in the rate of change of signal intensity at various b values. It is termed "apparent" because the measured value does not indicate pure diffusion, but reflects capillary perfusion and other processes. Low ADC values reflect restricted diffusion and appear hypointense on ADC map (but hyperintense on DWI) within hours. [24] Likewise, non-restricted diffusion

appears hyperintense on an ADC map (but hypointense on DWI). The reason for the early decline in ADC is thought to be cytotoxic oedema.[25]

- *Perfusion weighted imaging*

It evaluates the blood flow in the cerebral microvasculature and detects areas of perfusion abnormalities. There are two major methods currently used to determine PWI: bolus-tracking PWI and arterial spin-labeling techniques (ASL-PWI). Bolus-tracking, which is also called first-pass bolus method or susceptibility-based perfusion imaging, requires the i.v injection of a paramagnetic contrast agent, for example a gadolinium chelate. The difference between the increased magnetic susceptibility of the contrast agent and the lower susceptibility of the surrounding tissues creates local field inhomogeneities, which result in signal loss on T2*-weighted images. From the data obtained time-signal intensity curves are create and various hemodynamic parameters can be calculated (TTP, MTT, rCBF, rCBV).

DWI combined with PWI and magnetic resonance angiography (MRA) of neck and intracranial vessels permits precise diagnosis of stroke mechanism, such as carotid or MCA occlusion, dissection, distal branch occlusion and small vessel disease.

The concept of mismatch, based on the subtraction of perfusion and diffusion volumes, has emerged as a simple way to identify the area at risk in emergency.[17, 22] The abnormal diffusion is assimilated to final ischemic injury. In this model, the penumbra corresponds to the hypoperfused area with normal diffusion (Figure 6). Sequential studies have shown that in the absence of rapid reperfusion, the initial lesion has an extension at the expense of the hypoperfused zone.[19, 20]

Unlike PET, perfusion MRI does not allow an absolute quantitative evaluation of cerebral hemodynamics. The main parameters used (TTP: time to peak, MTT, CBF, CBV) give only a semi-quantitative hemodynamic information; most of the times, they are reported to the contralateral hemisphere values. Thus, it is not possible to distinguish accurately the penumbra from the oligemia zone (mildly hypoperfused area without risk of progression to infarction), part of it being included in the mismatch. As for the lesions detected by diffusion imaging, they do not necessarily correspond to necrosis. Longitudinal MRI studies have shown that about 30-50% of the initial lesion volume seen in DWI was reversible.[21]

To sum up, the diffusion/perfusion mismatch is a rough approximation of the ischemic penumbra because: i) the perfusion techniques and data evaluation are not truly quantitative

and vary among centers; ii) the thresholds used for defining perfusion abnormalities have not been validated against PET thresholds; and iii) abnormal diffusion regions early after stroke onset can be reversed by timely intervention in both animals and humans.[26]

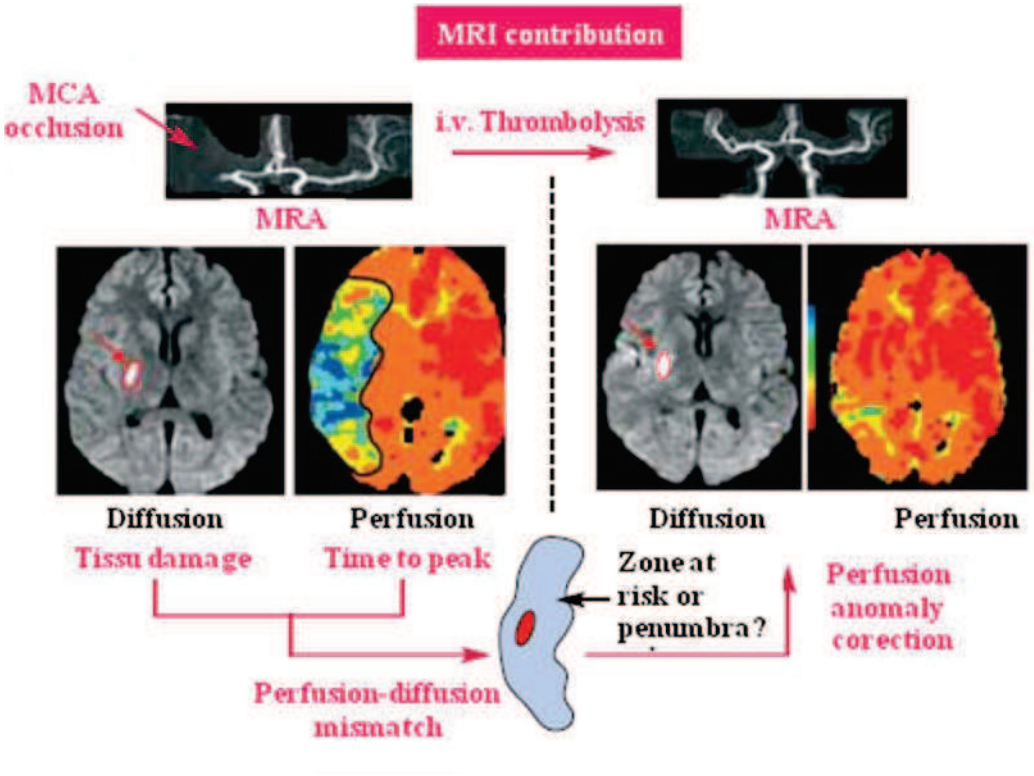


Figure 6. Mismatch correction in MRI after recanalization by thrombolysis. Reproduced from Wiart, 2005.

Imaging of the penumbra plays a crucial role in the development of new therapies, selecting those most likely to benefit.[27] The awareness of limitations in current penumbra assessment inclines toward new biomarkers development to characterize it. In this context, though controversial, MRI remains to date the most pragmatic imaging method.

In this context, the broad aim of our work is to identify new markers of brain response to cerebral ischemia, specifically those related to inflammation (blood brain barrier integrity, phagocyte cells activation), using MRI with the help of contrast agents.

III. Mechanisms of cell death in cerebral ischemia

Cell death can occur by necrosis or apoptosis.[28] These two mechanisms have distinct histological and biochemical signature.

Necrosis, or cytoplasmic cell death, is a passive pathological phenomenon resulting from a major disruption of biochemical systems that regulate cellular homeostasis (ion transport, energy production, pH maintenance). It consists of i) cell, organelle, and mitochondrial swelling or dilatation, ii) cytoplasmic vacuolation, iii) breaks of cell membranes, iv) disintegration of organelle and v) late and random DNA fragmentation, vi) cell bursting.[29]

Apoptosis, or programmed cell death, is a rather physiological phenomenon, essential for embryonic development, immune system and homeostasis of multicellular organisms. Nevertheless, it also characterizes many pathological conditions. Apoptosis is the primary mechanism of cell death in neurodegenerative diseases.[30, 31] The role of apoptosis in cerebral ischemia is currently the subject of numerous studies.[32] Apoptosis in mammalian cells is mediated by specific proteases, caspases (cysteine-dependent aspartate-specific proteases). Caspases are present as inactive precursors. When the initiator caspases (caspase 8 or 9) are activated by oligomerization, they cleave the precursors of effector caspases (caspases 3, 6, 7), triggering the cells suicide. Distinct morphologic features of apoptosis include: i) cell shrinking, ii) plasma membrane blebbing, iii) nuclear and cytoplasmic condensation, iv) clumping of chromatin at nuclear membrane, v) fragmentation of chromosomal DNA at internucleosomal intervals, vi) fragmentation of the cell into apoptotic bodies, and vii) degradation of the apoptotic body by lysosomal enzymes.[28]

The administration of caspase inhibitors during and after arterial occlusion in experimental models have reduced ischemic damage[33], suggesting that apoptosis could be a therapeutic target.

IV. Approved and potential treatment of ischemic stroke

Two therapeutic strategies are considered when confronting an ischemic stroke: i) thrombolysis, to try and restore blood flow to the compromised region, and ii) neuroprotection which involves the use of drugs to interfere with one or more of the mechanisms in the ischemic cascade (Figure 7).

To date, the only efficient treatment of stroke is thrombolysis, which consists in de-obstructing the vessel with the help of a pharmacological agent and inducing blood reflow and reperfusion of the affected ischemic tissue.

Neuroprotection consists in protecting the cerebral tissue from deleterious consequences of cerebral ischemia. Among potential neuroprotective agents, anti-inflammatory drugs appear very promising based on experimental data.

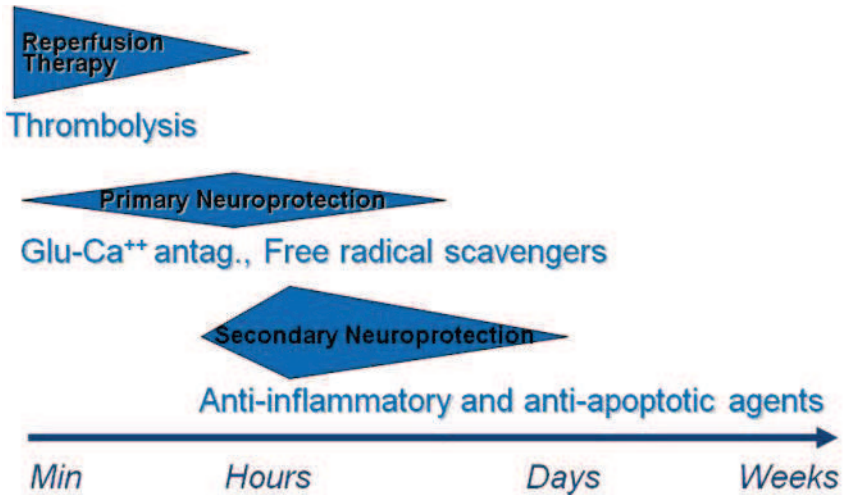


Figure 7. Time-depending therapeutical strategies when confronting cerebral ischemia. Adapted from Idecola ISC, 2007

IV.1 Reperfusion with tissue plasminogen activator

The reperfusion aims to dissolve, remove, or shatter the clot blocking the blood flow. Tissue plasminogen activator (tPA) is a clot-dissolving protein that cleaves the inactive plasminogen into the active enzyme plasmin. Plasmin then cleaves fibrin clots. This protein is naturally produced by cells in the walls of blood vessels and it can also be manufactured synthetically by genetic engineering techniques.

Thrombolytic therapy for stroke was first tested in the year 1958 with plasmin[34] and a full dozen different agents affecting the various steps of the coagulation and fibrinolytic cascades have been tested in humans since.[35] Thrombolysis with tPA is the treatment of choice for acute stroke within 4.5 hours of symptom onset.[36-38] Although approved by North American and, conditionally, by European authorities, only a small proportion of patients receive this therapy, mainly because of delayed arrival at and limited access to specialized stroke units.

A main concern of thrombolysis with tPA is that many patients do not reperfuse even when given the drug and up to 5% will experience hemorrhagic complications as the result of the drug administration. Part of this is the relative inefficiency of intravenous tPA, which only achieves reperfusion in 25 to 30% of patients with middle cerebral artery occlusions. An intravenous/intra-arterial rescue strategy has been reported in the IMS study (The IMS Study

Investigators, 2004), and increases the efficacy with which vessels are opened[39, 40]. Therefore, besides thrombolysis, new treatments are being developed to be used either as monotherapy or in conjunction with tPA.

IV.2 Neuroprotective drugs

Neuroprotective drugs aim at salvaging the ischemic brain by: i) prolonging the time window for reperfusion therapies, ii) limiting reperfusion injury and the risk of hemorrhage, iii) minimizing the deleterious effects of the ischemic cascade, including inflammation.

As stated before, ischemia leads to excessive activation of excitatory amino acid receptors, accumulation of intracellular calcium, and release of other toxic products that cause cellular injury. By preventing excitatory neurotransmitter release, neuroprotective agents may reduce deleterious effects of ischemia on cells. The most commonly studied neuroprotective agents for acute stroke block the N-methyl-D-aspartate (NMDA) receptor. Dextrorphan was the first NMDA antagonist studied in human stroke patients.[41] Unfortunately, dextrorphan caused hallucinations and agitation; it also produced hypotension, which limited its use. Glutamate NMDA receptor antagonists such as Selfotel, Aptiganel, Gavestinel and others failed to show neuroprotective efficacy in human clinical trials or produced intolerable central nervous system adverse effects.

Other neuroprotective agents prevent potentially detrimental events associated with blood flow restoration. Returning blood contains leukocytes that may occlude small vessels and release toxic products. Agents that prevent white blood cells from adhering to vessel walls, limit formation of free radicals, or promote neuronal repair may protect the brain from additional injury during reperfusion.

Several anti-inflammatory strategies to decrease ischemic damage have been proposed.[42] The tetracycline family of antibiotics has been shown to reduce leukocyte infiltration and improve experimental stroke outcome.[43] Minocycline is a second generation antibiotic from tetracycline family that possesses anti-apoptotic and anti-inflammatory properties. It's plasmatic half-life in rodents is approximately 2h contrary to humans where in general the half-life is 6- to 9-fold longer than in mice.[44] Its anti-inflammatory effects were showed in experimental animal models of stroke (see Table 2). Minocycline is currently evaluated in a clinical trial (Minocycline to Improve Neurologic Outcome in Stroke).[45]

Animal model			*Minocycline*		*Analysis*	*References*
Species	***Strain***	***Stroke Model***	***Dose (mg/kg)***	***Injection time***		
Rat	SD	tMCAO (90 min)	2 x 45 i.p on day 1 and 22.5 i.p for 2 days	T0-12h or T0+2h or T0+4h	TTC, IHC, Reverse Transcriptase–PCR	Yrjanheikki 1999[46]
Minocycline: i) did not affect rectal temperature, arterial blood pressure, plasma glucose, or arterial blood gases, ii) treatment started at T0-12 h reduced the size of the infarct in the cerebral cortex by 76% and in the striatum by 39%, iii) treatment started at T0+2h resulted in a reduction in the size of cortical (by 65%) and striatal (by 42%) infarct, iv) treatment started at T0+4h resulted in a cortical infarct size reduction by 63%.						
Rat	Wistar	embolic	45 i.p at T0+1h, T0+4h and 22.5 i.p at T0+24h, T0+32h		Infarct volume measurement	Wang 2003[47]
Minocycline: i) significantly reduced the infarct volume by 42%, ii) when administrated in combination with hypothermia, the infarct volume significantly reduced the infarct volume by 44%						
Rat	SD	tMCAO (90min)	10 i.v or 3 i.v	T0+4h or T0+5h or T0+6h	TTC, neurologic deficit exam	Xu 2004[48]
Minocycline at a dose of 3 mg/kg and 10 mg/kg i.v is effective at reducing infarct size within a 5 hour therapeutic time window after tMCAO. With a dose of 10 mg/kg the window to ameliorate neurological deficits is extended to 5 hours.						
Mouse	ddY	pMCAO	90 i.p	T0-60 min or T0+30 min or T0+4h	Neurologic deficit assessment, TTC, lipid peroxidation in forebrain homogenate	Morimoto 2005[49]
Minocycline: i) 60 min before or 30 min after the occlusion reduced the size of the infarct areas and that of the infarct volume, and also the brain swelling, ii) 4h after the occlusion, it did not significantly reduce any parameters, iii) inhibited both free radical production and lipid peroxidation in a concentration-dependent manner, iv) reduces the neuronal damage in part through an inhibition of oxidative stress.						

Mouse	FVB/N Balb/C wt MMP-9 ko	pMCA	45 i.p at T0-12h or T0+2h and 2x60 i.p every 12h and 6x45 i.p every 12h		TTC, Gelatin zymography	Koistinaho 2005[50]
Minocycline treatment started at T0-12h revealed that : i) at 24 hours after the onset of the ischemic insult the infarct volume was reduced by 33% , ii) at 72 hours after the onset of the ischemic insult infarct volumes in wt mice resulted in 50% reduction but it did not reduce the infarct size in MMP-9 ko. Minocycline treatment started at T0+2h after MCAO achieved no significant protection.						
Mouse	CB6/F1	dMCA (45min)	45 i.p at T0+30min, T0+12h and 2x22.5/day for 7 days		Behavioral studies, IHC, infarct volume assessment, SPRCT	Tang 2007[51]
Minocycline : i) reduces infarct volume, ii) improves sensorimotor function, iii) reduced annexin V uptake by 2- to 3-fold at each time point, iv) reduces apoptosis and inflammation. ^{99m}Tc-labeled annexin V SPECT can be used as a noninvasive tool to monitor apoptosis.						
Rat	SH	embolic	3 i.v over 5 min	T0+4h and T0+4h+ tPA at 6h	TTC, cerebral hemorrhage assessment, standard gel zymography (MMP-2 and MMP-9 levels)	Murata Y. 2008[52]
Minocycline: i) with delayed 6-hour tPA decreased plasma MMP-9 levels, ii) reduced infarction, iii) diminished brain hemorrhage.						
Rat	Wistar	tMCAO (3h)	3 iv or 45 ip	tPA+ i.v mino at T0+5min and at T0+12h or tPA +i.p mino at T0+12h	TTC, neurologic exam, gelatin zymography and MMP immunoblotting, ELISA for hemoglobin	Machado 2009[53]
Minocycline: i) did not affect t-PA fibrinolysis, ii) at 3 mg/kg iv decreased total protein expression of both MMP-2 and MMP-9, iii) decreased the incidence of hemorrhage, iv) improved neurologic outcome and v) appeared to decrease mortality.						
Rat	SD	tMCAO (2h)	90 i.p at T0 and 45 i.p daily until sacrifice		Behavioral testing, cerebral infarction assessment, inflammation assessment, immunofluorescent staining	Kim 2009[54]
Minocycline: i) does not deliver any benefits in infarct size and behavioral outcome, ii) post-ischemic treatment suppresses inflammation with decreased neurogenesis.						

Rat	SD	tMCAO (30 min)	20 i.v or 100 i.v	T0+60min	Behavioral tests, TTC, IHC	Matsukawa 2009[55]
Minocycline: i) at high dose induced toxicity for both neurons and astrocytes, iv) at low dose attenuated stroke-induced behavioral deficits, decreased apoptotic cell death and reduced cerebral infarction.						
Rat	SD	tMCAO (2h)	10 i.v at T0+1h and 10 i.v daily for 6 days		PET imaging (day 7) with [^{18}F] DPA-714 , TTC	Martin 2010[56]
Minocycline treatment: i) had no effect on the size of the infarcted area, ii) significantly decreased [^{18}F] DPA- 714 binding, suggesting that the drug exerts an anti-inflammatory activity. [^{18}F]DPA-714 PET is a useful biomarker to study novel anti-inflammatory strategies in experimental cerebral ischemia.						
Rat	SD	tMCAO (90 min)	45 i.p	T0+2h and T0+12 and every 12h for 5days	Functional assessment, IHC	Chu LS 2010[57]
Minocycline: i) accelerated the recovery of sensorimotor and cognitive functions; ii) attenuated the loss of neuron density; iii) inhibited astrogliosis in the boundary zone around the ischemic core; iv) did not affect infarct volume; v) significantly inhibited the increased 5-LOX expression in the proliferated astrocytes in the boundary zone, and in the macrophages/microglia in the ischemic core.						

Table 2. Literature review of minocycline treatment in experimental stroke. tMCAO – transient middle cerebral artery occlusion; pMCAO – middle cerebral artery occlusion; dMCA – distal middle cerebral artery occlusion; SD - Sprague-Dawley; ddY - Deutschland Denken Yoken; SH – spontaneous hypertensive; wt – wild type; ko-knockout; MMP-9 - matrix metalloprotease-9 gene; T0 - reperfusion/permanent occlusion;

Chapter II

Post-Ischemic neuroinflammation imaging using USPIO

I. Inflammatory response in stroke

Cerebral ischemia is accompanied by a marked inflammatory reaction which involves several types of immune cell (Table 3), in particular those of the mononuclear phagocyte system (neutrophils, monocytes, macrophages).

White blood cells (leucocytes)	Classification	Diameter (µm)	Lifetime	Role
Mast cells (MS)	connective tissue MS	8-20	30min-few years	Intimately involved in wound healing and defense against pathogens
	mucosal MS			
Granulocytes	**neutrophils**	**10-12**	**6h-few days**	**Defend against bacterial or fungal infection through phagocytosis**
	eosinophils	10-12	8-12days	Combat multicellular parasites
	basophils	12-15	few hours-few days	Responsible for allergic and antigen response by releasing the chemical histamine causing vasodilation
Lymphocytes	Thymus (T) cells	7-8	weeks to years	Involved in cell-mediated immunity (cytokines)
	Bone (B) cells			Responsible for humoral immunity (antibodies)
	Natural Killer (NK) cells			Act against tumors and virally infected cells (activated in response to interferons (cytokines))
Monocytes		**7.79-9.99**	**hours to days**	**- Phagocytosis** **- Migration from bloodstream to tissue and differentiation into tissue resident macrophages**

Table 3. Overview of immune system cells

I.1 Cells of the mononuclear phagocyte system

I.1.1 Neutrophils (polymorphonuclear neutrophils)

Neutrophils account for approximately 70% of all white blood cells. Their metabolism is largely anaerobic (transformation of glycogen to lactic acid without oxygen). This is an advantage because they can survive in poorly oxygenated or anaerobic conditions, such as necrotic tissue. Neutrophils have a key role in phagocytosis when they encounter a foreign or an infected cell. Once the pathogen is ingested, the chemicals in the granules are released to destroy it. The life span of neutrophils is short: 10-12h into the bloodstream and 2 to 3 days in the tissues.

I.1.2 Monocytes

Monocytes constitute 3-8% of the leukocytes in the blood. They are produced by the bone marrow from haematopoietic stem cell precursors called monoblasts. Monocytes circulate in the bloodstream for about one to three days and then migrate into tissues where they mature into tissue resident macrophages. Monocytes and their macrophage and dendritic-cell progeny serve three main functions in the immune system: i) phagocytosis, ii) antigen presentation and iii) cytokine production. Typical cytokines produced by monocytes are TNF tumor necrosis factor (implicated in tumor regression), IL-1 interleukin-1 (responsible for the production of inflammation) and IL-12 interleukin-12 (response to antigenic stimulation).

In response to inflammation signals, monocytes can move quickly (approx. 8-12 hours) to sites of infection in the tissues and divide/differentiate into macrophages and dendritic cells to elicit an immune response

I.1.3 Macrophages

Monocytes circulate for several days before entering tissues to renew the resident tissue macrophages.[58] Macrophages result from differentiating monocytes. They have a 21 µm diameter and a half life going from a few days (activated stage) to a few months or years (immature stage). Macrophages are versatile cells that play many roles: i) as scavengers they rid the body of worn-out cells and other debris, ii) as initiators of an immune response they present an antigen stimulating lymphocytes and other immune cells that respond to pathogen, iii) as secretory cells they regulate the immune responses and the development of inflammation, iv) they carry receptors that allow them to be activated into single-minded pursuit of microbes and tumor cells, v) they have the ability to regenerate neuronal tissue.

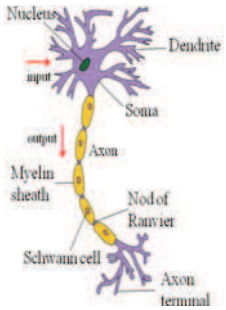
Macrophages can be identified by specific expression of a number of proteins including CD14, CD11b, F4/80 (mice)/EMR1 (human).

- *Tissue macrophages*

A majority of macrophages are strategically located in tissues that are most likely to have a microbial invasion or an accumulation of dust. Depending on their location macrophages have specific names: kupffer cells in liver, alveolar macrophages in lungs, osteoclasts in bone, microglia in brain.

- *Microglia - macrophages of central nervous system (CNS)*

A brief overview of central nervous system (CNS) cells and their role is represented in Table 4.

<table>
<tr><th>CNS cells</th><th colspan="2">Classification</th><th>Role</th></tr>
<tr><td rowspan="2">Neurons
(~86 * 10^9)

</td><td colspan="2">Structural
- Unipolar: dendrite and axon emerging from same process.
- Bipolar: axon and single dendrite on opposite ends of the soma.
- Multipolar: more than two dendrites</td><td rowspan="2">Processing and transmission of information by electrical and chemical signaling.</td></tr>
<tr><td colspan="2">Functional
<u>Direction</u>:
- Afferent neurons (sensory neurons) convey information from tissues and organs into the CNS.
- Efferent neurons (motor neurons) transmit signals from the CNS to the effecter cells.
- Interneurons connect neurons within specific regions of the central nervous system.

<u>Action on other neurons</u> :
- excitatory (glutamate release cells)
- inhibitory (GABA release cells)
- modulatory

<u>Neurotransmitter production</u> :
- Cholinergic neurons—acetylcholine
- GABAergic neurons— γ aminobutyric acid
- Glutamatergic neurons—glutamate
- Dopaminergic neurons—dopamine
- Serotonergic neurons—serotonin</td></tr>
<tr><td rowspan="3">Glial Cells
(~85* 10^9)</td><td rowspan="2">Macroglia</td><td>Astrocytes (astroglia)</td><td>- They regulate the external chemical environment of neurons: i) maintain extracellular ion balance; ii) recycle neurotransmitters released during synaptic transmission.
- Provision of nutrients to the nervous tissue (glucose).
- Role in the repair and scarring process of the brain following traumatic injuries.
- Biochemical support of endothelial cells that form the blood–brain barrier.
- May regulate vasoconstriction and vasodilation by producing substances such as arachidonic acid.</td></tr>
<tr><td>Oligodendrocytes</td><td>- Wrap tightly around axons to form the myelin sheath which provides insulation to the axon that allows electrical signals to propagate more efficiently.</td></tr>
<tr><td colspan="2">Microglia</td><td>- Brains immune cells: they use phagocytic and cytotoxic mechanisms to destroy foreign agents.</td></tr>
</table>

Table 4. Neural tissue

Microglia cells are the resident macrophages of the brain and account for up to 20% of the total glial cell population. They differentiate in the bone marrow from hematopoietic stem cells. Microglia cells are extremely plastic, and undergo a variety of structural changes based on their location and current role. Depending on their form three types of microglia can be distinguished:

- *Amoeboid* shape: within the perinatal white matter areas in the corpus callous during the development and rewiring of the brain when debris and apoptotic cells abound.[59]

- *Ramified* (resting) state: at strategic locations throughout the entire brain. They are unable to phagocytose cells and display little or no immunomolecules. The purpose of this state is to maintain a constant level of available microglia to detect and fight infection, while maintaining an immunologically silent environment.[60]

- *Activated* state: i) non-phagocytic phase when cells undergo morphological changes like thickening and retraction of branches, expression of immunomolecules, secretion of cytotoxic factors, recruitment molecules, and pro-inflammatory signaling molecules; ii) phagocytic phase when cells take on a large, ameboid shape, travel to the site of the injury, engulf offending material and display the resulting immunomolecules for T-cell activation. In addition they secrete pro-inflammatory factors to promote more cells to proliferate. Activated phagocytic microglia also interacts with astrocytes and neural cells to fight off the infection with minimal damage to the healthy brain cells.[59, 60]

Microglia is very sensitive to subtle alterations in their neuronal microenvironment. Its activation is considered a hallmark of CNS inflammation. Activated microglial cells become immunohistochemically indistinguishable from infiltrating myeloid cells (monocytes/ macrophages).[61] In particular, activated cells of the monocytic lineage, whether resident microglia or blood-borne macrophages, over express an outer mitochondrial membrane protein formerly known as the peripheral benzodiazepine receptor (PBR), now renamed "translocator protein (18kDa)" (TSPO 18kDa).[62] Radiolabeling of the prototypic PBR/TSPO ligand PK11195 with 11C enabled in vivo imaging of microglial activation using positron emission tomography (PET scan) (Camsonne 1984).

I.2 Inflammatory Mechanism

Inflammation is an immune response to injury or infection that is taking place in vascularized tissues aiming to limit the extension of the lesion and activate the repair process. The first four cardinal signs of inflammation were described by Celsus (around 40 AC): pain (dolor), heat (calor), redness (rubor) and swelling (tumor). Virchow in 1858 completed the list with the loss of function (functio LAES) of the affected organ.

Inflammation can be induced by exogenous or endogenous pathogens:

- microorganisms contamination (bacteria, viruses, fungi, parasites)
- physical (traumatisms, burns, radiation) or chemical (caustic, toxins, venoms) agents
- lack of vascularization: an inflammatory reaction secondary to ischemic necrosis (cells premature death).

Regardless of the origin of the attack, the mechanism of the inflammatory response can be divided into two phases: vascular and cellular phase.

- *Vascular phase*

Acute inflammation is characterized by marked vascular changes: i) vasodilation, ii) increased permeability and iii) slowing of blood flow, induced by the actions of various inflammatory mediators. These molecules trigger arteriole dilatation process which causes increased blood flow and slowed traffic at the site of inflammation. Vasodilation progresses to capillary level causing the redness and heat of inflammation. Increased vessel permeability permits the fluid and plasma proteins to move into tissues, causing swelling (edema). The endothelial cells activation provokes membrane expression of adhesion molecules (interleukins), inducing cellular phase.

- *Cellular phase*

Cellular stage is marked by movement of phagocytic white blood cells into the area of injury. The leukocytes specific cell-adhesion molecules (CAM) facilitate the adherence of immunitary cells to the endothelium. The first ones to arrive at the lesion site are granulocytes within 6 hours after the insult. They are progressively replaced by mononuclear cells.

I.3 Post-Ischemic inflammatory reaction

I.3.1 Course of action

There is evidence that inflammatory reactions can contribute to secondary ischemic injuries with eventual worsening of neurologic outcome.[63] Alternatively, inflammation under certain circumstances could promote functional recovery, by supporting neurogenesis and plasticity.[64]

Following insult there is an immune response at the site of injury characterized by the infiltration, accumulation and activation of inflammatory cells (neutrophils, monocytes/macrophages). Within hours after focal cerebral ischemia onset peripheral leukocytes adhere to the cerebral endothelium, cross the vessel wall and invade the damaged parenchyma.[65, 66] Once activated inflammatory cells start to secrete a large variety of cytotoxic agents such as cytokines (interleukin-1 (IL-1), -6 (IL-6), Tumor Necrosis Factor α (TNF)), chemokines (Cytokine-induced neurophil chemo-attractant (CINC) and the Monocyte chemo-attractant protein-1 (MCP-1)) and to promote the expression of adhesion molecules (selectins, integrins, and immunoglobulins), matrix metalloproteinases (MMPs) with an increased production of free radicals. At the same time astrocytes and microglia become activated. These neural and glial cells secret inflammatory mediators such as : i) cytokines, ii) nitric oxide (NO) through inducible nitric oxide synthase (iNOS), iii) reactive oxygen species (ROS) and iv) metalloproteinases (MMPs) contributing to further tissue damage.

The sequence of cellular events in post-ischemic inflammatory response is summarized in Figure 8. The results were obtained by flow cytometry and immunohistochemistry in a mouse model of transient ischemia (tMCAO) by Gelderblom et al.[67] These results are consistent with previous studies.[68-70]

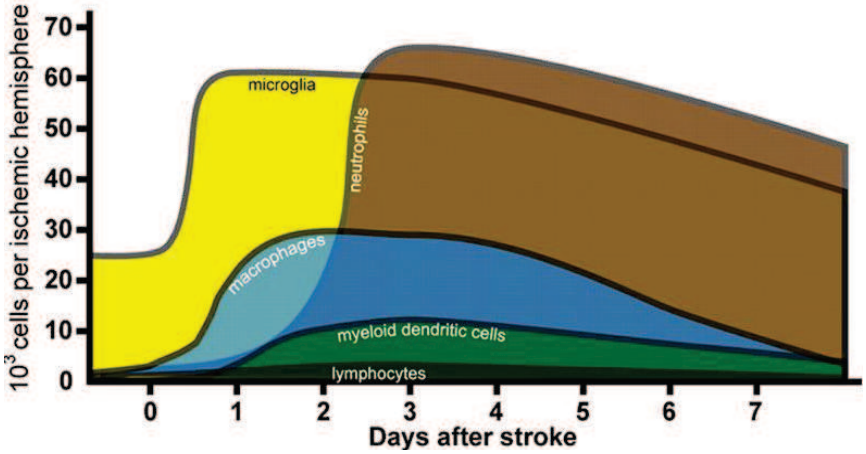


Figure 8. Temporal dynamics of poststroke inflammation in mice.
Reproduced from Gelderblom M et al., Stroke 2009

I.3.2 Molecules of the inflammatory response

Cytokines

Cytokines are molecules that mediate and modulate the inflammation and which control the immune response. They are secreted by neural cells (glial and neuronal), endothelial cells and leukocytes and by cells of the mononuclear phagocyte system[71, 72]. Schematically, some cytokines have a more pro-inflammatory and deleterious role (IL-1, IL-6, TNF-α) and others have a rather neuroprotective effect (IL-10, TGF-β).[73]

- *IL-1*

For example intraventricular injection of recombinant IL-1 after pMCAO heightens the edema and infarct size, while the influx and adherence of neutrophils are increased.[74, 75] These results suggest that the deleterious role of IL-1 over expression in cerebral ischemia may be related to its effect on leukocyte adhesion and the formation of cytotoxic edema.

- *TNF-α*

The kinetics of TNF-α expression are similar to that of IL-1, increasing from the first hours post-ischemia, with a second peak between 24 and 36 hours[76, 77]. Its inhibition reduces ischemic lesion volume, while the administration of TNF-α of syntheses increases it significantly.[78]

- *IL-6*

The production of IL-6 is parallel to that of TNF-α and IL-1. In the ischemic cerebral hemisphere of a pMCAO rat, the IL-6 production starts 3 hours post-occlusion. A peak of expression is reached after 12 hours and a high rate is maintained for more than 24 hours.[79]

- *IL-10*

IL-10 is one of the anti-inflammatory cytokines that inhibits IL-1 and TNF-α. Its synthesis is increased in case of cerebral ischemia.[80] In a mouse model of ischemic stroke, it was demonstrated that IL-10 synthesized by a subpopulation of T cells (regulatory T cells) limits the extension of ischemic injury.[81]

- *TGF-β*

TGF-β is mainly produced by microglial cells and astrocytes and in a smaller quantity by neurons. In mice models of ischemia, the expression of TGF-β in injured tissue increases within 6 hours after ischemia, and remains at a high level for 15 to 21 days.[82, 83] In a tMCAO mouse model, the overexpression of TGF-β results in a significant reduction in lesion volume.[84]

Chemokines

Chemokines represent a subclass of low molecular weight cytokines (8-10 kDa). Production and secretion of these factors are stimulated by the expression of pro-inflammatory cytokines such as IL-1 and TNF-α.[85, 86] The Cytokine-induced neurophil chemoattractant (CINC) and the Monocyte chemoattractant protein-1 (MCP-1) are respectively involved in the recruitment of neutrophils and macrophages / monocytes in inflammatory brain ischemia.[86, 87] Recent studies have linked the expression of MCP-1 and the lesion volume, suggesting that monocytes attracted to the ischemic tissue by the chemokine may be involved in the formation of lesions.

Adhesion molecules

- *Selectins*

Interactions between endothelial cells and formed elements of blood are mainly conditioned by the cell adhesion molecules. During ischemia, activated endothelial cells express selectins on their surface (mainly E and P in the initial stage). They will interact with circulating white blood cells that slow down in contact with the endothelium.[72] In various models of pMCAO and tMCAO in rats, the expression of P and E selectins increases.[88] The role of E and P selectins in leukocyte recruitment from the initial stage of ischemia was observed during their transient over-expression between 2 and 8 hours after ischemia, returning to baseline at the 24th hour.[89, 90] The P-selectin promote leukocyte adhesion to ischemic endothelium, this mechanism appears to play an essential role.[72, 91] They will interact with circulating white blood cells that slow down in contact with the endothelium [72]). In various models of pMCAO and tMCAO in rats, the expression of P and E selectins increases.[88] The role of E and P selectins in leukocyte recruitment from the initial stage of ischemia was observed during their transient over-expression between 2 and 8 hours after ischemia, returning to baseline at the 24th hour.[89, 90] The P-selectin promote leukocyte adhesion to ischemic endothelium, this mechanism appears to play an essential role.[72, 91]

- *Integrins*

Integrins connect the endothelial cells, astrocytes and the basal lamina, which form the blood-brain barrier (BBB, see the text below). These molecules are essential for maintaining the integrity of the cerebral microvasculature.[92] Integrins CD11b/CD18 (Mac-1) are the main adhesion molecules expressed at the membrane of leukocytes. They are activated by various chemo-attractive substances, in particular cytokines and chemokines. These molecules are essential for maintaining the integrity of the cerebral microvasculature.[92]

- *Components of immunoglobulin superfamily*

Intracellular adhesion molecules (ICAM) of the immunoglobulin superfamily are expressed by the endothelial cell membrane stimulated by cytokines. ICAM-1 (CD54) is an endothelial- and leukocyte-associated transmembrane protein known for its importance in stabilizing cell-cell interactions and facilitating leukocyte endothelial transmigration. Vascular cell adhesion molecule 1 (VCAM-1) protein mediates the adhesion of lymphocytes, monocytes, eosinophils and basophils to vascular endothelium.[92]

Free radicals

- *Nitric oxide (NO)*

NO plays a role of molecular messenger as well as a neurotoxin. As a molecular messenger, NO is involved in multiple brain functions: i) synaptic plasticity, ii) morphogenesis, iii) regulation of neurotransmission and iv) cerebral vaso-relaxation. Conversely, NO has been implicated as a toxic factor in infections of the central nervous system, in inflammatory and neurodegenerative diseases, and cerebral ischemia.[68]

During cerebral ischemia NO is involved in glutamate excitotoxicity and in the early stages of the ischemic cascade.[93] In neuronal and endothelial cells, these free radicals are responsible for membrane lipid peroxidation and protein oxidation, thus contributing to cell death.[94] During tMCAO, the expression of inducible nitric oxide synthases (iNOS) is maximal 12 hours after insult onset and normalized to the fourth day. In pMCAO, the peak is delayed at the 48th hour, followed by normalization on the seventh day.

I.3.3 Blood brain barrier after ischemia onset

The post-ischemic inflammation is closely linked to the blood-brain barrier status, which under normal conditions regulates the exchanges between the peripheral immune system and brain tissue. The integrity of the blood-brain barrier (BBB) protects neuronal microenvironment by limiting the penetration of blood cells and by isolating the brain parenchyma from any systemic conditions. The function of the BBB is based on the integrity of the cellular matrix consisting of endothelial cells, basal lamina and astrocytic extensions. Ischemia damages the matrix and disrupts intercellular interactions. The frequency of alterations of the BBB reported during stroke varies from 15 to 66% depending on the ischemia severity, exploration methods and time window evaluation.[95] Several mechanisms contribute to these alterations, which are schematically divided into two phases.

By the second hour post-ischemia, the endothelial basal lamina is dissolved [96] causing a rapid increase of BBB permeability.[97] The loss of the BBB generates an accumulation of vascular endothelial growth factor (VEGF), thrombin and catabolism enzymes. The neurons, glial and endothelial cells release a proteolytic enzyme MMP-9 responsible for digesting the basal lamina that will allow the infiltration of blood leukocytes and the vasogenic edema formation. After this first phase of early BBB destruction a second series of alterations occurs between 24 and 72 hours after ischemia onset.[98]

I.3.4 Neutrophils after ischemia onset

The recruitment of neutrophils to ischemic brain begins with neutrophil rolling on activated endothelial blood vessel walls, mediated by selectins, followed by neutrophil activation and adherence, mediated by integrins and immunoglobins. When adhered to cerebral blood vessel walls, neutrophils transmigrate into the cerebral parenchyma, a process facilitated by blood brain barrier (BBB) disruption. The recruitment of neutrophils can obstruct the microcirculation and prevent complete restoration of cerebral blood flow after reperfusion. This blockage may cause further tissue damage after ischemia. Once neutrophils penetrate into ischemic brain they cause tissue damage by releasing oxygen free radicals and proteolytic enzymes.

I.3.5 Microglia/macrophage behavior after ischemia onset

The temporal evolution of microglial response was described in a tMCAO (2h) rat model.[99] Microglia were absent in the first hour of reperfusion in severely ischemic areas. Between 2 and 10h post-reperfusion, amoeboid microglial cells gradually infiltrated into ischemic injury. At 22h after reperfusion two types of microglia cells could be identified: i) amoeboid shape cells predominantly located in the center of the lesion where severe neuronal damage occurred and ii) ramified microglia in the periphery of ischemic injury where morphologically intact neurons were located. At later times (46 - 166 hours post-reperfusion), the pan-ischemic injury became necrotic, and amoeboid microglia-like cells infiltrated the entire ischemic region. In contrast, branched looking microglial cells predominated in periphery of the infarct, where structurally intact neurons could be observed. This study shows that microglial activation is a heterogeneous process which seems to be correlated with the severity of neuronal damage. This study does not distinguish formally the infiltration of blood-borne macrophages of microglia. To clarify this question, Schroeter et al. performed a depletion of blood monocytes before the photothrombotic cerebral ischemia.[100] Thus, the early

phagocytic response (day 3) appeared to be constituted of microglial activation, whereas hematogenous macrophages were recruited later (day 6).

The differentiation between circulating macrophages and microglia was performed using chimeric mice (irradiation to deplete the marrow cells + bone marrow graft of transgenic mice expressing the fluorescence). Thus, microglial activation was observed from day 1, while the penetration of blood-borne macrophages to the lesion from day 4, with a peak at day 7 and then decreased. Moreover, even between D4 and D7, the vast majority of phagocytic cells corresponded to microglia. Using a model of pMCAO in mice Rupalla et al. also showed early microglial activation starting 30 minutes post-ischemia in the periphery of the infarct.[101]

I.3.6 Benefic/deleterious effects of microglia on ischemic injury

The impact of microglial activation and macrophage influx in cerebral ischemia remains controversial. It can be noted in the literature of the last 10 years theoretical and experimental arguments supporting both beneficial and deleterious role of microglia. These conflicting data reflect the diversity of molecular mechanisms regulating the activation and the response of microglia.[102]

Deleterious effects

Microglia in fact represents a major source of pro-inflammatory cytokines such as IL-1, IL-6 and TNF [78, 103, 104] , which are considered the main mediators of delayed neuronal post-ischemic death [105]. The effect of some of these pro-inflammatory cytokines is not formally defined. This is the case of IL-6 whose removal is not accompanied by a neuroprotective effect [106]. In addition to their phagocytic activity and synthesis of cytokines, activated microglia secrete many cytotoxic molecules that may participate in ischemic damage: free radicals, nitric oxide (NO) and glutamate.[107-109]

Intervention studies using minocycline to inhibit microglial activation showed a reduction in infarct volume in global [110] and focal [46] ischemia models. In a study conducted on rats that underwent tMCAO (90 minutes), the addition of minocycline 4 hours after ischemia onset reduced by 63% the lesion volume measured on day 3, and was associated with a reduction in microglial activation in the periphery of the ischemic injury. A reduction in lesion volume was also observed in a tMCAO (2h) mouse model treated with minocycline (intraperitoneal injection at 30 minutes and 12 hours post-MCAO; sacrifice mice on day 1).[111] The minocycline-treated mice also showed a reduction of the breakdown of the blood-brain barrier, and a less common hemorrhagic transformation compared to control mice.

Benefic effects

Despite the above data, there are many arguments advocating a beneficial role of microglia. Microglial cells secrete various neurotrophic factors (nerve growth factor (NGF), brain derived neurotrophic factor (BDNF), neurotrophin-3 (NT-3), neurotrophin-4 (NT-4)) that may contribute to the survival of vulnerable neurons.[112]

Lalancette-Hébert team showed in a tMCAO mouse model that the proliferation of a subpopulation of resident microglial cells exerted a neuroprotective effect otherwise suppressed by a selective anti-proliferative chemotherapy.[113] The study of cellular interactions between microglia and ischemic brain tissue revealed the neuroprotective effect of resident microglia related to their activity of phagocytosis of infiltrating neurotoxic neutrophils. This phagocytic activity directed against polymorphonuclear neutrophils in post-ischemic condition was also reported by other authors.[114, 115] This mechanism could actually represent an important microglial neuroprotective function. An argument in favor of potential positive role of microglia in the process of neuroplasticity is provided by Wake et al. These authors have seen a change in contacts between microglial extension and synapses after ischemia, and suggest that microglia actively participate in the elimination of synaptic connections in the cerebral ischemia.[116]

One way to reconcile these seemingly contradictory data on the role of microglia in cerebral ischemia is to consider the hypothesis of Lai and Todd stating that the severity of neuronal damage could affect the beneficial or deleterious microglial participation through a close dialogue between the two cell populations exposed to ischemia.

II. Superparamagnetic iron oxide (SPIO) contrast agent

Magnetic resonance (MR) contrast agents are applied in approximately 25% of all imaging procedures. Superparamagnetic iron oxide (SPIO) contrast agents have been the subject of intensive research over the last 20 years. Several kinds of optimizations (adjustment of particle core size, choice of surface coating material and the surface charge) made them valuable for a wide range of applications including: liver and spleen imaging[117], bone marrow[118], lymph node[119], vascular inflammation and MR angiography[120]. Their use as MRI contrast agents is only one of their many applications as their pharmacokinetics, physicochemical and proton relaxation properties recommend them for other nanomedical applications like: i) magnetic separation, ii) drug delivery, iii) hyperthermia treatments.[121] Currently, they are widely evaluated as MRI markers for the assessment of inflammatory and degenerative disorders associated with high macrophage phagocytic activity.[122]

In this work, superparamagnetic iron oxide nanoparticles were used for MR monitoring of a therapeutic effect in an experimental stroke model.

II.1 SPIOs classification

Superparamagnetic contrast agents consist of iron oxide crystals (diameter in the range 4-10 nm) usually maghemite (γ-Fe_2O_3) and / or magnetite (Fe_3O_4) in varying proportions (as maghemite is a result of oxidized magnetite). Stability and biocompatibility are conferred by a biomolecular coating which will be discussed below in the text. Distinct classes of iron oxide nanoparticles are defined depending on their hydrodynamic size:

- *Superparamagnetic Particles of Iron Oxide (**SPIO**):* correspond to particles with aggregated iron oxide cores and a mean hydrodynamic diameter greater than 50 nm.

They are quickly picked up by liver macrophages (Kupffer cells). These particles have a very short half-life in plasma and are used in clinics for liver tumor detection.[123-126] There are two kinds of SPIO agents, the large oral SPIO used for gastrointestinal imaging and smaller injectable colloidal suspensions. Two SPIO compounds are commercialized for intravenous use: dextran coated ferumoxides (Endorem® in Europe, Feridex® in the USA and Japan) and carboxydextran coated ferucarbotran (Resovist® in Europe and Japan (see Table 5).[123]

- *Ultrasmall Superparamagnetic Particles of Iron Oxide (**USPIO**):* corresponds to mono-dispersed or mono-crystalline iron oxide particles with a diameter between 10 and 50 nm.

The prototype of USPIO was developed by Weissleder et al. in 1990 in the need of having particles small enough to be able to migrate across a capillary wall. Several USPIO have been investigated in humans for several imaging applications: ferumoxtran-10 (dextran), VSOP (citrate)[127], feruglose (pegylated starch) or SHU555C (carboxydextran) (see Table 5). Because of their lower uptake by the liver and spleen cells, USPIOs are relevant for: i) detection of cancerous tumors, ii) identification of atherosclerosis plaques and iii) assessment of inflammation extent.[123] In vitro studies have shown that due to their smaller size, USPIOs are less internalized than SPIOs.[128-130] ***A member of this class of nanoparticles was used in our experimental studies.***

- *Very-small Superparamagnetic Iron Oxide Particles (**VSOP**):* diameter of about 7 nm. They offer interesting perspectives in magnetic resonance angiography[131] because of their smaller size, which gives them a long plasma half-life.[132]

- *Micron-Sized Iron Oxide Particles (**MPIO**):* diameter between 300 and 1,000 nm. Due to their size, a good cell internalization is obtained and thus with increased iron content cell detection is improved.[133-135]

Names	Company	Applications	Relaxometric properties 1.5 T $mM^{-1} s^{-1}$	T1/2 in human hours (μmol Fe/kg)	Coating agent	Hydrodynamic size (nm)
Ferumoxides AMI-25 Endorem®/Feridex®	Guerbet Advanced Magnetics	Liver imaging	r_1=10.1	2	Dextran T10	120–180
		Cellular labelling	r_2=120	(30)		
Ferumoxtran-10 AMI-227 BMS-180549 Sinerem®/Combidex®	Guerbet Advanced Magnetics	Metastatic lymph node imaging				
		Macrophage imaging	r_1=9.9	24–36		
		Blood pool agent	r_2=65	(45)	Dextran T10, T1	15–30
		Cellular labelling				
Ferumoxytol Code 7228	Advanced Magnetics	Macrophage imaging				
		Blood pool agent	r_1=15	10–14	Carboxylmethyl-dextran	30
		Cellular labelling	r_2=89	(18–74)		
Ferumoxsil AMI-121 Lumirem®/Gastromark®	Guerbet Advanced Magnetics	Oral GI imaging	n.a.	Oral	Silicon	300
Ferucarbotran SHU-555A Resovist®	Schering	Liver imaging	r_1=9.7	2.4–3.6	Carboxydextran	60
		Cellular labelling	r_2=189	(8–12)		
SHU-555C Supravist®	Schering	Blood pool agent	r_1=10.7	6		21
		Cellular labelling	r_2=38	(40)	Carboxydextran	
Feruglose NC100150 Clariscan®	GE-HC (abandoned)	Blood pool agent	n.a.	6 (36)	Pegylated starch	20
Ferristene Abdoscan®	GE-Healthcare	Oral GI imaging	n.a.	Oral	Sulphonated styrene–divinylbenzene copolymer	3500
VSOP-C184	Ferropharm	Blood pool agent	r_1=14	0.6–1.3	Citrate	7
		Cellular labelling	r_2=33.4	(15–75)		

Table 5. *Iron oxide nanoparticles commercially available or under clinical investigations. Relaxometric properties were measured at 1.5 T, 37 °C, in water or in plasma. Reproduced from Corot et al., Advanced Drug Delivery Reviews 58 (2006) 1471–1504)*

As a conclusion SPIOs and MPIOs are quickly captured by the liver Kupffer cells, to a lesser extent in the spleen and in small amounts in bone marrow and lymph nodes. Conversely, USPIOs are found in the liver in smaller amounts, with significant concentrations in the spleen and lymph nodes.[136]

II.2 USPIO Synthesis

Synthesis of superparamagnetic nanoparticles is a complex chemical process. The main challenge is to obtain a monodisperse size, since the properties of the nanoparticles strongly depend upon the dimension of the magnetic grains.[137] Another great challenge is to optimize a process that can be easily performed on an industrial scale, without any complex purification procedures or the use of dangerous reactants and solvents.

Numerous chemical methods (microemulsions, sol-gel syntheses, sonochemical reactions, hydrothermal reactions, hydrolysis and thermolysis of precursors, flow injection syntheses and electrospray syntheses) can be used to synthesize magnetic nanoparticles for medical imaging applications. The classical synthesis of SPIO agents involves the co-precipitation of iron oxide in an aqueous solution of ferrous and ferric salts. The formation can be written as follows:

$$Fe^{2+} + 2\ Fe^{3+} + 8OH^- \rightarrow Fe_3O_4 + 4\ H_2O$$

Magnetite (Fe3O4) is very sensitive to oxidation and is transformed into maghemite (γFe2O3) in the presence of oxygen, according to the following expression:

$$Fe_3O_4 + 2\ H^+ \rightarrow \gamma Fe_2O_3 + Fe^{2+} + 2\ H_2O$$

The advantage of the method is that large quantities can be synthesized; it is thus applied on an industrial scale for the synthesis of commercially available products. Although this classical co-precipitation method allows modification of the mean size of nanoparticles by adjusting pH, ionic strength, temperature, or the ratio of Fe (II) over Fe (III), control of particle size distribution is limited. Recently developed methods that will not be discussed here enable a more precise control of size dispersity, but are not yet applicable on an industrial scale.[138]

II.3 USPIOs coating

After synthesis of the magnetic nanoparticle, coating is required to prevent destabilization and agglomeration of the colloid. There are several classes of stabilizers that can be used: inorganic materials (silica, gold), monomeric stabilizers (carboxylates, phosphates) and polymer stabilizers (dextran, polyethylene glycol, polyvinyl alcohol, alginate, chitosan) [138]. Superparamagnetic particles dedicated for in vivo use are generally coated with dextran and dextran derivatives thanks to their good biocompatibility. The biocompatible coating material allows a safe intravenous administration. The nature of the coating also needs to be optimized in order to prevent any aggregation and sedimentation of the superparamagnetic nanoparticles providing a stable solution for injection. Together with the geometric arrangement on the surface, the nature of the coating plays a significant role in pharmacokinetic and biodistribution properties.[123]

- *Dextran coating*

This coating is composed of hydroxyl groups attached to iron nuclei via hydrogenated atoms that stabilize the envelope.[139] Dextran unrelated or partially attached constitutes an extra layer representing most of the hydrodynamic diameter, which explains the difference between the

size of the particle (core 6 nm for Ferumoxtran-10 [139]) and the high final hydrodynamic diameter (35 nm [140]).

The affinity between particles and cells membranes is more or less important. To quantify this affinity, the zeta potential (potential difference between the average surface of the particle and the surrounding water, expressed in mV) is usually given. For example, for Ferumoxides (Endorem, Guerbet) the zeta potential is -32mV while for smaller particles like Ferumoxtran-10 (Sinerem, Guerbet) it is close to 0 mV.[141] These may help explain their low uptake by macrophages, their longer half-life and their relative safety even at high doses.[142]

- *Anionic coating*

As stated above, the addition of polymer around the surface of the crystal increases the hydrodynamic diameter. To obtaining crystals of smaller sizes changing the surface charge of nanoparticles is recommended. For example anionic particles (Anionic Maghemite NanoParticles: ANMP) synthesized at the Matière et Systèmes Complexes (MSC) Laboratory, Paris, are citrate, so that the core of maghemite is 8 nm and the hydrodynamic diameter 30 nm.[143, 144] These particles have two times more iron than Ferumoxtran-10 for a comparable hydrodynamic diameter. The major advantage of using anionic particles lies in the fact that their zeta potential is large (-30 mV), resulting in better affinity with the cells membrane and allowing better internalization.

II.4 USPIOs metabolism

The intracellular metabolism of the particles depends on their chemical composition. The ferumoxtran-10 is metabolized via the lysosomal pathway in 7 days.[145] The envelope of biodegradable polymers dextran is destroyed by enzymatic reaction; the nucleus of iron oxide is recycled, gradually incorporated into the pool of body iron then reused for including the synthesis of hemoglobin. This catabolism is essential since this exogenous source of iron is potentially toxic to brain cells.[146] If the particles currently available have proven their lack of long-term toxicity, it is necessary to evaluate iron metabolism and the bioenzymatic environment involved in iron storage for each iron oxide nanoparticle under development (research subject referred to in Chapter 5). It is not possible to predict the pharmacokinetics, or intracellular distribution of a given particle with reference to the properties of other particles.

II.4 USPIOs effects on MR signal

The superparamagnetism is a size-dependant property of magnetic nanoparticles. This phenomenon occurs when crystals are smaller than a magnetic mono-domain, usually between 4 and 18 nm. Superparamagnetic nanoparticles are anisotropic and their magnetic moment tends to align along the privileged (easy) axes of magnetization. Their magnetization at each time-point is not zero, even in the absence of an external magnetic field but time-average magnetization is null because the magnetic moment jumps from one easy direction to another. When an external field is applied the magnetic domains are oriented along the axis of the field. The superparamagnetic particles have no remanent magnetization thus when the external magnetic field is removed the magnetic moments of individual domains lose their collective orientation and the net magnetic moment becomes zero.

When using an USPIO, signal intensity depends on various factors, like: particle size and composition, concentration of particles in the imaging voxel and sequence parameters.
The *efficiency* of a contrast agent is defined by its relaxivity (the slope of the dependence of water relaxation rates on the concentration of the contrast agent [147]), as follows:

$$R_{1,2} = R^0_{1,2} + r_{1,2} \cdot C$$

where: $R_{1,2}$ (s^{-1}) describe the longitudinal (1/T1) and transverse (1/T2) relaxation rates of protons in the presence of the contrast agent ; $R^0_{1,2}$ ($1/T^0_{1,2}$) are the relaxation rates in the absence of the contrast agent; C (mM) is the contrast agent concentration; $r_{1,2}$ ($s^{-1}mM^{-1}$) is the relaxivity, a measure of how much the proton relaxation rate is increased per unit of concentration of contrast agent [123, 148].

Nanoparticles longitudinal relaxivity is important; they decrease the longitudinal relaxation time T1 and induce hyperintensities on T1-weighted images (Muller et al., 1991). Their transverse relaxivity is high, with a strong decrease of the transverse relaxation time T2 inducing hypointensities on T2-weighted images. The T2 effect is predominant, but each type of particle presents a particular T1/T2 ratio that will condition the signal changes for a given type of sequence. The magnetic susceptibility or T2* effect is related to significant differences in magnetization between two adjacent structures of the same MR image. This difference in magnetization results from the heterogeneous distribution of nanoparticles which increases the local magnetic field gradients. These gradients accelerate the transverse phase shift of the surrounding spins and produce a significant signal drop out, which is far more

extensive on MR images than the actual volume occupied by the particles. T2* effect is also increased by the compartmentalization of the product in the cell or by particle aggregation.[149]

The effect of USPIO internalization into macrophages on relaxivity was evaluated by Brisset et al, using T1, T2 and T2 * imaging at high field MRI (4.7 T and 7T). Two contrast agents were evaluated: Ferumoxtran-10 (Sinerem ®, Guerbet, France) and the AMNP (anionic maghemite nanoparticles, UMR CNRS 7612, France). The study was conducted on agarose phantoms containing free USPIO or macrophages labeled with USPIO at different concentrations, as well as mice stereotaxically injected with labeled macrophages. The in vitro study showed that the relationship between iron concentration and the respective relaxivities r1, r2 and r2 * was linear in the range from 0 to 36 mM. The r1 relaxivity of free Ferumoxtran-10 decreased significantly between 4.7 T and 7T, while the r2 relaxivity decreases moderately, in agreement with the NMRD profile (Corot et al. 2006). The same result was found for the free AMNP, but with an even sharper decrease. For a given field, the internalization of USPIO resulted in a decrease in relaxivities r1 and r2 and higher relaxivities r2 *. These results were consistent with those published in clinical fields of 1.5 T and 3T (Billotey et al. 2003, Simon et al. 2006). The in vivo study showed a match between the relative quantitative measurement of T2 and the number of injected cells.

II.5 Cell labeling with USPIO

II.5.1 In vivo labeling of phagocyte cells

Compared to other MR contrast agents, USPIO toxicity is low. Also, the amount needed for clinical imaging is lower than the physiological iron stores.

The different biological events taking place after USPIOs administration is represented in Figure 9.

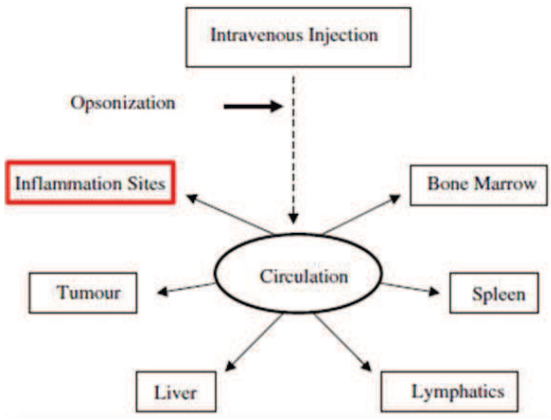


Figure 9. The fate of nanoparticles following intravenous injection. Reproduced from C.Berry and A.Curtis, 2003

After being injected into the blood stream the nanoparticles rapidly undergo an opsonization process which consists in being coated by components of the circulation such as plasma proteins. The role of this process is to render the particles recognizable by the reticuloendothelial system (RES) which then removes them from the circulation. The opsonization can be influenced by: i) particle size[150, 151] and ii) coating - hydrophilic particles can resist this coating process and are cleared more slowly[152]; the most common coatings are derivatives of dextran, polyethylene glycol (PEG), polyethylene oxide (PEO), poloxamers and polyoxamines.[153]

In vivo administration of nanoparticles leads to their phagocytosis by macrophages, whether within the blood-pool (circulating monocytes) or locally at the inflammation site (tissue macrophages/activated microglia in the brain). Macrophages can thus be labeled and monitored in vivo with exogenous magnetic contrast agents. Importantly, this technique can be applied in patients, as several (U)SPIOs are already being used in humans.

II.5.2 In vitro labeling of macrophages

Ex vivo cell labeling is a good choice: i) to mark cells that can't be marked in vivo (lymphocytes for example), ii) to improve iron concentration of phagocytic cells. The quality and efficiency of cell labeling depends on: the nanoparticles core coating, the incubation time, the cell type and its differentiation stage.[123, 154] The simple incubation labeling method is the easiest to implement because it involves the addition of contrast material directly into the cell culture medium. This technique is used to label phagocytic cells that spontaneously internalize contrast medium. Raynal et al. have shown that in vitro SPIOs uptake by macrophages is 10 times more important compared to USPIOs uptake.[129] This difference is mainly due to the final hydrodynamic diameter of the contrast agent as the type of coating and the iron oxide core diameter were the same for both classes of nanoparticles. Bowen et al. established a dose - incubation time relationship proportional to the amount of iron in the incubation bath for one line of SPIO or USPIO-labeled macrophages (Figure 10).[155]

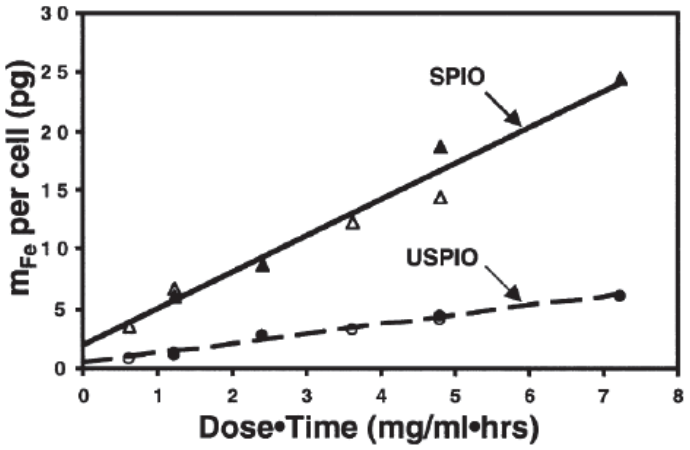


Figure 10. Cellular iron uptake curves indicating the mass of iron per cell that is taken up per unit dose and incubation time. Reproduced from Bowen et al.,2002

Non-phagocytic cells can also be labeled with a charged surface contrast agent such as AMNP (Table 6).[144]

Cell types (origin)	d (μm)	K (μM)$^{-1}$	m_0 (pg)	τ_t (h)	Φ_0	m_p (pg)
Immune cells						
Raw macrophages (mouse)	11.7 ± 0.8	17 ± 4	6 ± 0.2	1.3 ± 0.2	25 ± 5	33
Hybridomas (mouse)	12	44 ± 31	2.4 ± 0.2	0.4 ± 0.1	1.5 ± 0.3	5.5
Dendritic cells (human)	12.2 ± 1.6	29 ± 8	6.6 ± 0.4	0.9 ± 0.1	1.8 ± 0.5	15.2
OT-1 lymphocytes (mouse)	8.4 ± 0.6	43 ± 26	1.3 ± 0.1	2 ± 0.8	1.1 ± 0.5	2.2
EL4-B lymphocytes (human)	9.2 ± 1.5	30 ± 10	4.1 ± 0.2	1.4 ± 0.2	1.3 ± 0.4	8
Tumour cells						
HeLa ovarian carcinoma (human)	20.2 ± 2.6	17 ± 5	18 ± 0.3	1 ± 0.1	2.5 ± 0.2	37.5
PC3 prostatic carcinoma (human)	14.6 ± 2.3	16 ± 5	8.1 ± 0.2	0.4 ± 0.1	1.8 ± 0.3	13.4
HuH7 hepatic carcinoma (human)	11.6 ± 1.7	27 ± 11	3.4 ± 0.2	1.2 ± 0.1	1.5 ± 0.2	8.3
Therapeutic adult cells						
Hepatocytes (mouse)	20 ± 4	30 ± 13	21.3 ± 0.8	1.4 ± 0.2	1.9 ± 0.3	49
Gingival fibroblasts (human)	17 ± 3	24 ± 8	13.5 ± 0.6	1.6 ± 0.5	1.6 ± 1	28
Smooth muscle cells (rat)	14 ± 1	29 ± 8	5.8 ± 0.2	1.5 ± 0.1	1.9 ± 3	12.4
Therapeutic stem cells or progenitor cells						
Myogenic precursor cells (pig)	14 ± 2.5	22 ± 11	3.5 ± 0.2	1.8 ± 0.3	1.1 ± 0.3	4.8
Endothelial progenitor cells (human)	13.8 ± 2.1	39 ± 12	8.9 ± 0.3	1.4 ± 0.2	1.9 ± 0.3	20.5

Table 6. Cell types labeled with AMNP. d - cell diameter, K -the affinity constant of AMNP for the cell membrane, m_0 - the binding capacity on plasma membrane (in mass of attached particles), τ_t - the characteristic time for internalization, Φ_0 - the maximal fraction of internalized membrane, m_p - the predicted mass of iron per cell for a labeling condition of ^{147}=20 mM for 2 h at 37°C. Reproduced from Wilhelm and Gazeau, 2008

III. USPIO dedicated imaging techniques

III.1 USPIO-enhanced MRI of post-ischemic neuroinflammation

To date, few teams have monitored phagocytic cell trafficking after focal cerebral ischemia using MRI coupled with (U)SPIO injection.

- Pre-clinical studies

An early study in a pMCAO rat model, led by Doerfler et al. in 2000, showed no impact of USPIO administration on clinical scores and lesion size.[156] However, the dose was ten times as low as in the following studies, the aim being to use USPIO as a marker of perfusion, not inflammation. Table 7 synthesizes the studies published so far, to our knowledge, using a permanent model of focal cerebral ischemia.

Animal model		Contrast Agent			MRI			Reference
Species	**Stroke model**	**Name**	**Dose (µmol/kg)**	**Injection time**	**Imaging times**	**Field strength**	**Sequences**	
Rat	EC	Ferumoxtran-10	100	T0+5h	D0, D1, D2, D4, D7	4.7T	T2 map	Rausch et al. 2001[157]
Rat	PT	Ferucarbotran	200	MRI-24h	D1-9, D11, D12, D14	1.5T	T2, 3D CISS, Gd-T1	Kleinschnitz et al. 2003 [158]
Rat	PT	Ferumoxtran-10	300	MRI-24h	D6	7T	3D T2*	Schroeter et al. 2004 [159]
Rat	PT	Ferumoxtran-10	300	MRI-24h	D6	7T	T2*, 3D T2*	Saleh et al. 2004 [160]
Rat	PT	Ferucarbotran	300	T0, T0+2h, T0+24h	D1, D2, D5, D7, D14	1.5T	T2, 3D CISS	Kleinschnitz et al. 2005 [161]
Rat	PT	Ferumoxtran-10	300	MRI-24h	D6, D8, D11	4.7T	T2 map, T2, Gd-T1	Engberink et al. 2008 [162]
Mouse	EC	Ferumoxtran-10	2000	T0+5h,	D0, D1,D2, D3	7T	T2, T1, Gd-T1	Wiart et al. 2007 [163]
Mouse	EC	Ferumoxtran-10	2000	T0+5h,	D0, D1	7T	T2, T1, Gd-T1	Desestret et al. 2009 [164]

Table 7. Literature review of USPIO-enhanced MRI in the permanent middle cerebral artery occlusion (pMCAO) model. EC- Electrocoagulation; PT- Photothrombosis; T0 = Occlusion time; T0+5h = 5h after occlusion; MRI-24h = 24h before MRI; Gd-T1: T1-weighted MRI with gadolinium chelate injection (to assess BBB integrity); PB- Prussian Blue. Reproduced from Chauveau F. et al, Int J Clin Pharmacol

The first study reporting an USPIO injection to assess inflammation in a model of cerebral ischemia was performed in 2001 by Rausch et al.[157] This was a sequential study on rats after intravenous injection of Ferumoxtran-10 (Sinerem ®, Guerbet) 5 hours after permanent middle cerebral artery occlusion. On T2-weighted images, the authors have shown a transient T2 hypointense signal (from D1 to D4) first in the perilesional area then in the lesion core. A co-localization of hypointense signals with histological staining of macrophages (labeled with anti-ED1) and iron (PB, Prussian Blue staining) was found. The same team used the same methodology a year later in a model of transient ischemia (tMCAO), supposed to reduce the risk of alteration of the BBB.[165] Timing of the injection and the MRI protocol (days 1, 2, 3, 4 and 7) remained the same. Histological analysis included sections treated with: i) PB for iron detection, ii) an anti-ED1 immunostaining, assumed to be labeling exclusively the blood born macrophages and iii) an anti-immuno-lectin Griffonia for the resident microglial cells. Only signal changes in T1 were observed at 48 hours. These signals gradually disappeared from 72h. No signal change after USPIO injection has been reported on T2 sequences. At the histological level, Prussian Blue immunostaining was positive only at D7. The authors explained the 5 days delay in detecting the iron nanoparticles by arguing: (i) that USPIOs might have been released by the infiltrated macrophages recruited for scar formation and re-ingested by secondarily recruited macrophages, and (ii) that Prussian Blue might become sensitive to iron oxide nanoparticles only after degradation of their dextran coating, an enzymatic process that could take several days.

These first results were confirmed in a photothrombosis model of ischemia by Kleinschnitz et al. who has conducted two studies with SPIOs.
In the first one[158], several rats (n = 3 to 6) were imaged at different time points (D1, D2, D3 up to D14) after photothrombosis. The SPIO administration (0.2 mmol Fe / kg of Resovist ®, Schering) was performed 24 hours before the MRI. At the end of the MRI sessions, rats were sacrificed for immunohistochemical analysis (PB and anti-ED1 immunostaining). The results were as follows : i) no areas of signal loss were present in ischemic lesions at early stages 1 to 5 days after photothrombosis, ii) at day 5.5 and day 6 post-photothrombosis a small rim of signal loss appeared at the outer margin of the hyperintense ischemic lesions, ii) at day 7 and day 8 a hypointense moderate signal in the center of the lesion and a peripheral hyperintense signal on T2-weighted images was observed. The MRI signals were correlated with PB positive staining of iron between J5 and 8 days in the periphery and then in the center of the lesion. The presence of macrophages labeled with anti-ED1 has been demonstrated between

J5 and J14, but macrophages no longer exhibited intracellular iron deposition at late stage (J9-J15).

A second study[161] was conducted by the same team using the same animal model but with an increased dose of SPIO (0.8 mmol Fe/kg of Resovist®,) administrated at the beginning of and after photothrombosis (2h and 24h). MRI was performed at 3 hours, D1, D2, D5, D7 and D14. A markedly hypointense lesion was seen on T2-w images acquired immediately after PT in animals receiving SPIO at the beginning of illumination. After 3h, a hyperintense rim appeared around the hypointense core that gradually increased until 48 h after PT. These signals were interpreted as associated with a "trapping" of particles in vascular thrombus. A subgroup of rats injected with a 2h delay after completion of PT showed hyperintense cortical lesions on T2-w images, but displayed a small hypointense rim at their outer margin. This suggested an ongoing vessel thrombosis. More delayed injection of SPIO particles (24h after PT) showed only hyperintense lesions on T2-w MRI with no signal loss, which indicated cessation of SPIO accumulation at this advanced stage of infarct development.

Saleh et al.[160] injected 300 µmol/kg Ferumoxtran-10 (Sinerem®, Guerbet) in a photothrombotic rat model, this time 5 days post-photothrombosis. A 7T MRI performed 24h post-injection showed a signal drop surrounding the lesion, co-localized with corresponding histological staining of PB positive and ED-1 positive macrophages.

Our team was the first one to conduct a prospective study in a pMCAO mouse model during the first 72 hours post-ischemia.[166] The superparamagnetic iron nanoparticles used for this study were Ferumoxtran-10, (Sinerem® Guerbet, France). The results of this study will be detailed as they paved the way for this thesis.

The contrast agent was administrated intravenously (2 mmol Fe/kg) 5 hours after pMCAO. The MRI protocol comprised: Gradient-echo (GRE) images acquired using a FLASH sequence (time of echo/time of repetition (TE/TR)=3.5/157.5 ms; flip angle=50°); T2-weighted images acquired using a RARE sequence (TE/TR=75/3000 ms); T2 maps obtained from a multiple spin-echo sequence (TE [interecho delay]/TR=11.4/4000 ms; 8 echoes; number of experiments 2) by fitting a monoexponential function to the data; Diffusion-weighted spin-echo images (TE/TR=14/2000 ms , 3 *b*-values (138, 554, and 1060 s/mm^2 in slice direction)).

At the end of the MRI protocol, the brains were collected for histological examination. An anti-F4/80 immunostaining was performed to detect macrophages/microglia and Prussian Blue staining for iron detection.

At 5 hours post-injury, BBB disruption was confirmed by T1 enhancement of the entire lesion after gadolinium injection. At the same time point, GRE and T2 maps revealed a marked signal drop-out, demonstrating the presence of USPIO at the border of the lesion. Then, quite surprisingly, a strongly contrasted line was seen to migrate along the corpus callosum from the ipsi- to contralateral hemisphere. On T2 maps this line presented itself as a hypointense signal while on GRE images it was identified as hyperintense signal. At 48 and 72 hours post-injury a rim-like signal loss was observed around the lesion. The ipsilateral area of decreased T2 extended beyond the perilesional area to the whole cortex and striatum. Furthermore, the contralateral corpus callosum was hypointense in both GRE and T2-weighted images. Histologically, the spatiotemporal pattern of F4/80-positive phagocytic cells distribution was perfectly correlated with the MRI signal. At 48 and 72 hours, a larger number of F4/80+ cells were observed in the perilesional area, the striatum adjacent to the lesion, and the whole corpus callosum, including the contralateral part. Areas of T2 decrease were slightly larger than areas covered by macrophage/ microglia infiltration, probably because of partial volume effects. The PB staining at 48h showed the presence of iron in the corpus callosum, ipsilateral subarachnoid spaces, choroid plexus and periventricular areas. Co-localization between low signal intensities on MRI, F4/80 labeled macrophage and PB staining brought strong arguments in favor of nanoparticles intracellularity.

This study showed that MR tracking of phagocyte cells was feasible in mice. Furthermore this noninvasive technique demonstrated that there was a remote inflammatory response away from the lesion site. These findings provided a proof of concept of USPIO-enhanced MRI efficiency for in vivo study of inflammatory response to focal cerebral ischemia.

These findings showing that USPIO-enhanced MRI is capable of mapping the inflammatory response after cerebral ischemia onset constitute the starting point of this thesis. Hereafter (Chapter 3) USPIO-enhanced MRI was used not only to detect the inflammatory response but also to see if it was capable to monitor a therapeutic effect of an anti-inflammatory treatment.

Table 8 synthesizes the studies published so far, to our knowledge, using a transient model of focal cerebral ischemia. Results using this model, although more relevant for translational purpose, are much more heterogeneous and still controversery.

Animal model		**Contrast Agent**			**MRI**			**Reference**
Species	**Extent (min)**	**Name**	**Dose (µmol/kg)**	**Injection time**	**Imaging times**	**Field strength**	**Sequences**	
Rat	30	Ferumoxtran-10	300	T0+5h	D0, D1, D2, D3, D4, D7	4.7T	T2, T1	Rausch et al. 2002 [165]
No T2 hypointense signal throughout the experiment; Transient T1 hyperintense signal at D2 Macrophages detection (ED1) in the lesion from D1 to D7; Detection of iron (PB) in the perilesional area at D7 only								
Mouse	30/60	Ferumoxtran-10	160	MRI-2h	D0, D1, D2, D3	7T	T2, Gd-T1	Denes et al. 2007 [114]
- No T2 hypointense signal - Global post-gadolinium lesion enhancement at D1, D2 and D3 post-pMCAO - Early microglial activation demonstrated by immunohistological markers but no monocytic infiltration according to the authors								
Rat	60	Ferucarbotran	200	MRI-24h	D1-6, D8, D10, D14	3T	T2, 3D T2*, Gd-T1	Kim et al. 2008 [167]
- Transient T2/T2* hypointense signal from D3 to D4 in certain parts of the lesion - Global post-gadolinium lesion enhancement at D3 - Macrophages detection (ED1) in the lesion at D3 and D4; Iron detection (BP) at D3 and D4 in agreement with T2/T2* hypointense zones, in the vicinity of vessels								
Rat	30	Ferumoxide	286	T0-7days	D1-4,D7	7T	T2 map, 3D T2*	Henning et al. 2009 [168]
- T2/T2* hypointense signal that was maximal at D4 and constant until D7 in the perilesional area - Co-location of non-specific staining of macrophages (ED1) and activated microglia staining (IBA) in the whole lesion; Co-location of well-differentiated macrophage staining (ED2) and iron staining (BP) in perivascular regions, the meninges, and the choroid plexus.								
Rat	60	Ferumoxtran-10	300 / 600 / 1000	T0+3days, T0+6days	D3-4, D6-7	4.7T	T2, T2*, T1	Farr et al. 2011 [169]
- Dose dependent decrease in global T_2 values. - No focal regions of hypointensity (T_2 or T_2*), or hyperintensity (T_1), were observed in the ischemic boundary of USPIO-treated animals. - T_2 was comparable amongst all groups prior to contrast agent administration, and there was a trend towards increasing ratio values following USPIO administration that also appeared to increase with dose.								

Table 8. Literature review of USPIO-enhanced MRI in the transient middle cerebral artery occlusion (tMCAO) model. All transient models were performed with the intraluminal thread model. T0 = Reperfusion time; T0+5h = 5h after reperfusion; MRI-24h = 24h before MRI; Gd-T1: T1-weighted MRI with gadolinium chelate injection (to assess BBB integrity); PB- Prussian Blue. Reproduced from Chauveau F et al, Int J Clin Pharmacol

- *Clinical studies*

The first clinical study was published in 2004 by Saleh et al.[170] USPIOs (Ferumoxtran-10) were injected in 10 stroke patients at the end of the first week after symptom onset (6 to 9 days). MRI was performed at 1.5T before injection, then between 24h and 36h and again between 48h and 72h post-injection. Parenchymal enhancement was observed on T1-weighted imaging in most cases (8 out of 10). However, T2/T2* effects were not systematically observed and seemed to be associated with vessels. As in experimental studies, there was a mismatch between regions showing BBB disruption (as assessed by post-gadolinium T1 enhancement) and regions showing USPIO enhancement. The authors suggested that USPIO enhancement was due to the infiltration of magnetically-labeled macrophages.

Our team conducted a similar study, in which USPIOs were injected at D6 after stroke onset and MRI was performed 72h post-injection.[171] In the 10 included patients, USPIO response was heterogeneous and not related to subacute lesion volume. As in the study by Saleh et al.[160, 170], T1 enhancement was observed in most cases (9 out of 10), while T2/T2* effects were not systematically observed (5 patients out of 10). No obvious relationship was observed between regions with BBB disruption and those showing USPIO-induced signal changes: for example, 3 patients without BBB disruption showed enhancement following USPIO administration, whereas one patient with severe BBB disruption showed no USPIO-induced signal change.

In their second study, Saleh et al.[172] investigated an earlier time window: USPIOs were injected 2 to 3 days following symptom onset and MRI was performed at different post-injection time points (24h-36h, 48h-72h, 10-11 days). Only 3 of the 9 patients included in the analysis showed signal changes on post-injection MRI. None of these patients showed T1 enhancement following gadolinium chelate administration. As in the previous study, signal changes consisted in enhancement on T1-weighted images, with an increase in enhancement between the first two post-injection examinations, and a decrease between the last two.

A subsequent study involving the same earlier time-window (2 days after stroke onset with MRI performed 48h after) confirmed these findings.[173] T1 enhancement was observed inside the lesion in only 1 of the 5 included patients. In this patient, post-gadolinium enhancement was more extensive than post-USPIO enhancement.

In these early studies, the heterogeneity of USPIO-labeling was thought to reflect inter-individual variability of post-ischemic inflammation.[172] This interpretation is attractive because the MRI method could then assist in selecting patients for an anti-inflammatory treatment. However, other factors of inter-individual variability (such as genetic, systemic ...) could explain the observed differences and it is therefore appropriate to consider these small series with caution.

III.2 USPIO detection by Synchrotron Radiation Micro-Computed Tomography (SR-µCT)

The use of SR-µCT in life sciences dates back to the works of Feldkamp et al. (1989) who pioneered this technique to analyze trabecular specimens. Since then, it has been significantly improved in both computer processing capabilities and experimental set-ups to suit various applications like: i) studies of morphology and physiology of vascular network of the brain (Plourabouéet al., 2004), ii) tomographic microscopy of fossil embryos (Chen et al., 2006; Donoghue et al., 2006), iii) in-vivo µCT of living snails (Postnov et al., 2002), iv) studies of the digestive tract of cephalopods (Westermann et al., 2002), iv) visualization of molecular variations of the myelin structure in a rat brain. With respect to the USPIO imaging a few studies were carried on: i) visualization of stem cells previously labeled with nanoparticles of iron oxide, inside skeletal muscles of dystrophic mice after intra-arterial transplantation[174], ii) detection of 3D spatial distribution of rat cardiac progenitor cells, labeled with iron oxide nanoparticles, inside the infarcted rat heart early after injection [175]. ***These precedent studies showing a positive result with respect to USPIO detection by synchrotron radiation and the need of a more precise mapping of the USPIO in a stroke-induced mouse model encouraged us to test this imaging technique (see Chapter IV).***

The setup and functional principle of a synchrotron facility is depicted in Figure 13 (ESRF, Grenoble France).

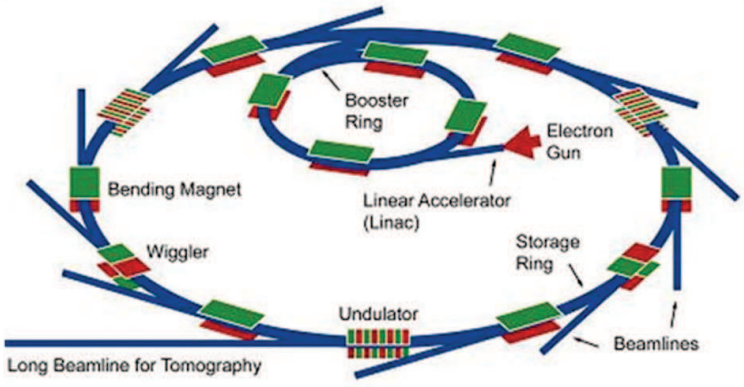


Figure 13. Assembly and functional principle of a synchrotron facility. Reproduced from Betz O. et al, J Microsc. 2007

Electrons are produced and emitted by an electron gun. They are accelerated first in a linear accelerator (linac) and then in a circular accelerator (booster ring) to reach the final energy level (6 GeV). These high-energy electrons are then injected into a large storage ring, where they circulate without gaining further energy and with a velocity close to that of the speed of light. Booster and storage rings are not perfectly round but consist of straight sections connected by curved ones in which dipole magnets bend the path of the electrons into the next straight section. To produce X-rays by means of the circulating electrons, they need to be decelerated or accelerated. The radiation is emitted in a well-defined direction, tangent to the electron storage ring, and is used in tangentially arranged experimental setups (beamlines) for diffraction, scattering or imaging experiments.[176]

X-ray microtomography

This technique has been used for large scale biological samples since the 1980s, when it was developed primarily for medical applications with a resolution of about 1 mm (Kalender, 2006). Since the arrival of synchrotron radiation, the resolution of tomography has improved dramatically, so that samples can now be imaged at submicrometer resolution, with effective pixel sizes down to about 0.25 μm.[176]

Contrast mechanisms of X-ray microtomography:

- *Absorption* (Figure 14 A)*: the traditionally exploited contrast mechanism in X-ray microtomography.* The intensity of the beam decreases exponentially with increasing propagation distance within homogeneous matter. The attenuation coefficient of the material determines the speed at which this exponential decrease occurs. For a given wavelength or energy of the X-rays, the absorption coefficient increases with the electron density of the material and with the atomic number of its constituting chemical elements: the higher the atomic number and atomic weight, the stronger the absorption, and thus the larger the difference in the atomic numbers, the larger the contrast. It is therefore not surprising that absorption contrast is *ideal for the medical imaging of high-density bone* surrounded by low density tissue, such as muscle and skin.[176]

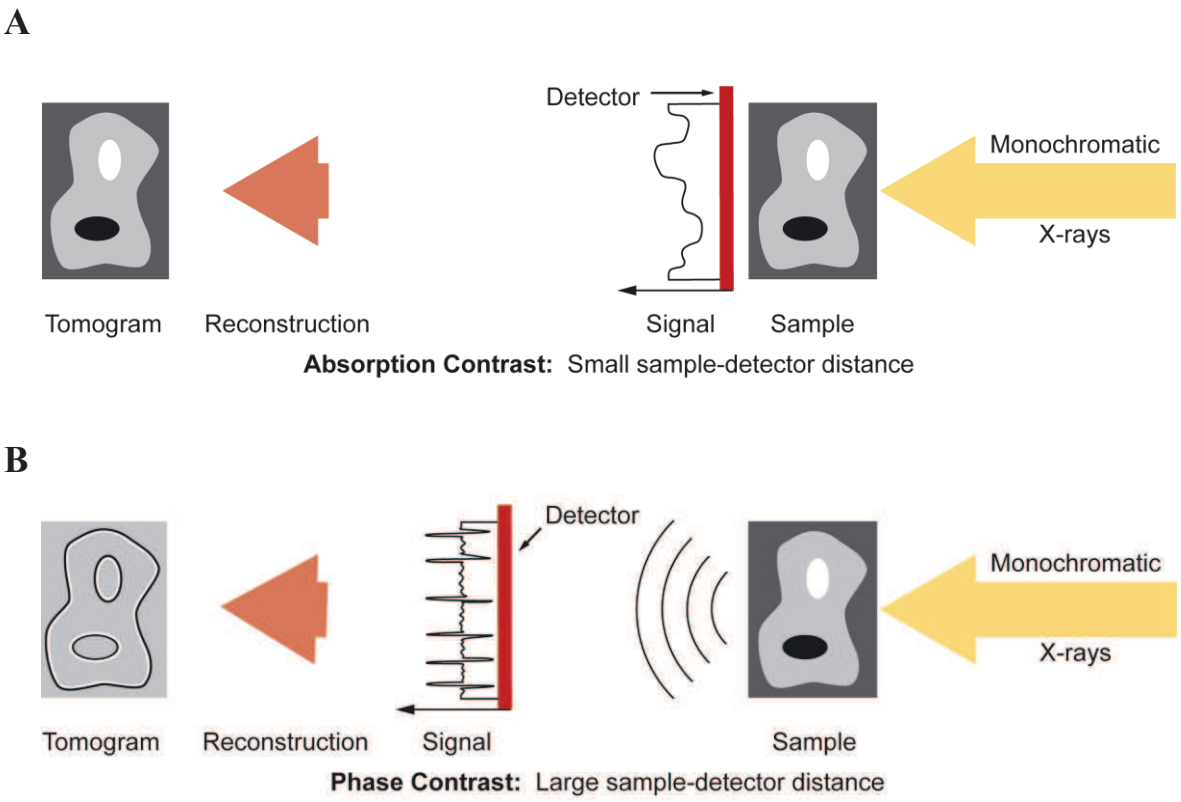


Figure 14 . Contrast mechanism exploited in synchrotron microtomography: A) conventional absorption tomography, B) phase contrast tomography.
Reproduced from Betz O. et al, J Microsc. 2007

- Phase contrast imaging (Figure 14 B)*:* takes advantage of the fact that the X-ray beam is not only absorbed when it penetrates matter, but also that the phase of the wave is affected. This effect is determined by the refractive index of the material. Except in the vicinity of absorption edges, the change in refractive index is proportional to the electron density or, to a good approximation, to the mass density. However, unlike absorption, phase changes do not influence the wave amplitude of the beam, and thus cannot be measured directly behind the sample. The image is instead created by the interference of the diffracted components of the beam with itself and the non-diffracted part of the beam. At the detection plane, these interferences are expressed in lateral intensity variations. Thus, a lateral coherence is required for this imaging technique; this property increases with a decrease in the source size of the beam and/or an increase in the source sample distance. In general, within an applicable range, the contrast increases with increasing distance between sample and detector. Hence, phase-contrast imaging enables the mapping of the changes in the refractive index. [177] Interfaces between materials with different densities correspond to discontinuities in the refractive index, which in turn lead to phase jumps causing Fresnel diffraction to occur,

appearing as white–black fringes in the images (Cloetens et al., 1997). The great advantage of phase-contrast imaging is that it produces edge-enhancement effects, which improve the visibility of small structures and which make it possible *to image materials with small variations in mass density and absorption contrast.* [176]

- Phase Tomography: procedure consisting in acquiring different scans at different distances followed by phase retrieval and reconstruction of phase map.

A quantitative relationship exists between the phase shift induced by the object and the recorded intensity and inversion of this relationship is called phase retrieval. Since the phase shift is proportional to projections through the threedimensional refractive index distribution in the object, once the phase is retrieved, the refractive index can be reconstructed by using the phase as input to a tomographic reconstruction algorithm. [178]

Unlike absorption, the phase is not simply related to image brightness. A holographic reconstruction procedure combining images taken at different distances from the specimen was developed.[179] It results in quantitative phase mapping and, through association with three-dimensional reconstruction, in holotomography, the complete three-dimensional mapping of the density in a sample. This tool in the characterization of materials at the micrometer scale is uniquely suited to samples with low absorption contrast and radiation sensitive system.

Grating interferometry

X-ray grating interferometry is a relatively new approach to phase contrast for hard X-rays (Figure 14 C). A periodic linear grid (or *grating*) G1 is used in transmission geometry to create a fine array of lines in the intensity distribution downstream of G1. If the incident beam is parallel, the period of this line pattern is either identical to the period of G1 or half that period, depending on the X-ray optical properties of G1. An object in the beam, positioned near the grid, will cause local distortions of this line pattern. If the distortions can be recorded on a detector, then this gives an image of the local beam propagation direction. Since usually the detector pixels are larger than the fringe spacing, and much larger than the fringe displacement, the fringes and their tiny displacement from unperturbed position cannot be resolved directly by the detector. Therefore, a second grid with absorbing lines placed in front of the detector is needed in order to get hold of the fringe position information. It transforms the average fringe position in front of each detector pixel into an intensity signal, and is therefore referred to as the "analyzer grid". The distance *D* between the two grids should be chosen so as to find the best tradeoff between sensitivity (which increases linearly with *D*) on

the one hand and spatial resolution as well as contrast on the other hand (both decreasing as *D* is increased). *An absorption image (as would be obtained without interferometer) and a phase-contrast image are obtained from the same set of raw images.*[180]

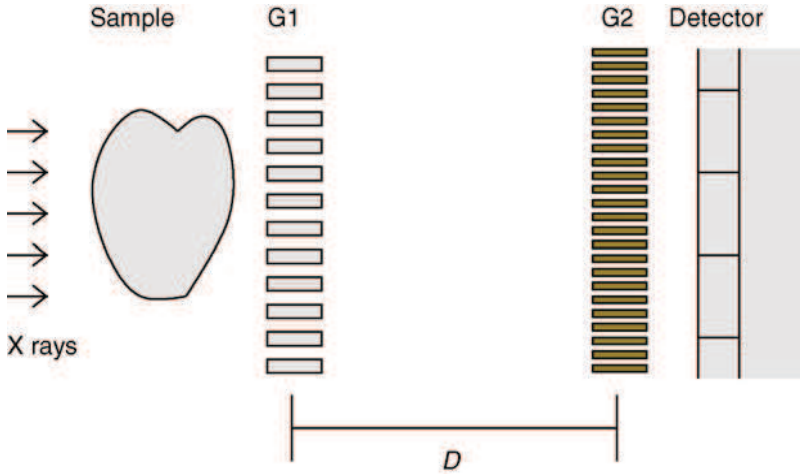


Figure 14C. Schematic setup of the interferometer. G1-beam splitter, G2- the analyzer, D-distance between the 2 grids (chosen to find an optimum tradeoff between sensitivity, spatial resolution, and contrast). Reproduced from Weitkamp et al, European J. of Radiology, 2008

III.3 USPIO detection by Transmission Electron Microscopy (TEM)

Current limitations of stroke imaging with direct iron oxide particles injection are represented by an incomplete understanding of iron biodistribution and corresponding imaging data, which depend on both physiopathological parameters (such as blood brain barrier integrity, inflammation status and cell trafficking) and nanoparticles properties (pharmacokinetics and contrast modulation).

Transmission electron microscopy (TEM) of USPIOs can yield information about: i) nanoparticle morphology (shape and size) by means of conventional TEM (CTEM), ii) particle structure (magnetite or maghemite) by means of selected area electron diffraction (SAED) and iii) nanostructure cristallinity (arrangement of atoms) by means of high resolution (HR) TEM imaging.

A series of precedent studies using TEM were carried on to investigate: i) iron content of liver, spleen and heart tissues of DBA/2 Hfe knockout mice [181], ii) intracellular pathway of anionic magnetic nanoparticles[144] , iii) the mechanism of nanoparticles uptake and their metabolism in the organism.[182]

Transmission electron microscopy uses a beam of highly energetic electrons to examine objects down to nanometric scale. The configuration of the electron microscope is given in

Figure 15A. TE microscope consists of a cilindrical ~2 meter tube completely devoided of air. The electron microscope visualises objects using a thin beam of rapidly moving electrons that interfere with the specimen placed in the tube. The electrons are emitted by the cathode at the top of the tube and then accelerated by the anod. They then pass through a small aperture, which forms them into a beam, and into the vacuum inside the tube. The beam is maintained along the tube by means of electomagnetic lenses (condensor, objective and projector lens). The electromagnetic field generated by the coils focuses the beam at the center of the tube.

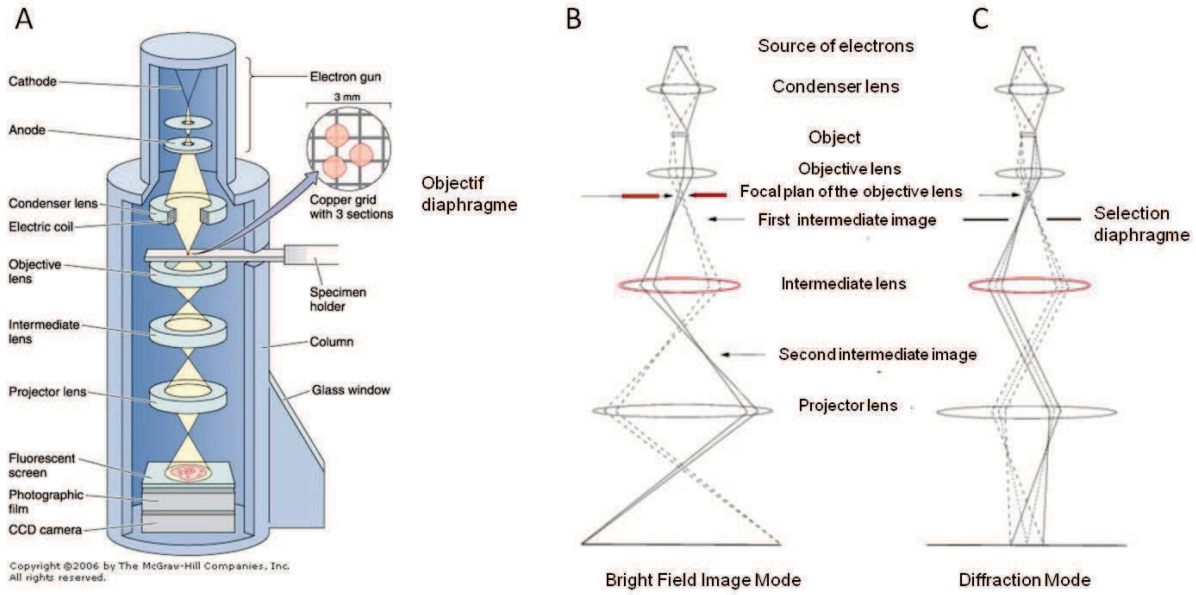


Figure 15 . Schematic view of a transmission electron microscop (A), bright field imaging mode (B) and selected area electron diffraction mode (C).

Electrons encounter the specimen and are either absorbed, scatered or pass through it (Figure 16). TEM imaging modes use only the electrons that pass through the specimen (lower part of the diagram in figure 16):

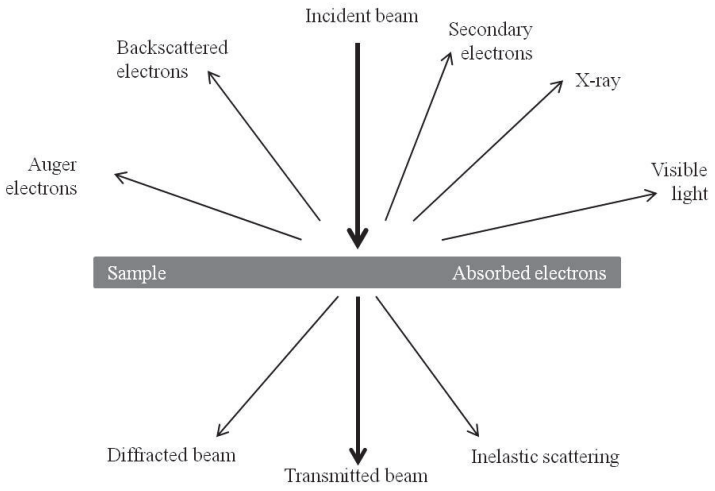


Figure 16 . Signals generated when a beam of electrons interacts with a thin specimen. Reproduced from Williams and Carter, Transmission Electron Microscopy A Textbook for Materials Science

- *Bright Field imaging mode uses the unscattered electrons* (transmitted beam)

The transmission of unscattered electrons is inversely proportional to the specimen thickness. Areas of the specimen that are thicker will have fewer transmitted unscattered electrons and so will appear darker, conversely the thinner areas will have more transmitted and thus will appear lighter [183]. Also the transmitted beam intensity in crystallized samples is largely controlled by diffraction phenomena described hereafter.

- *Diffraction imaging mode uses elastically scattered electrons* (diffracted beam)

The scattered electrons without energy loss are used to obtain the *diffraction diagram*. All electrons follow and are thus scattered according to Bragg's Law[184]:

$$n \cdot \lambda = 2 \cdot d \cdot \sin(\theta)$$

where: λ corresponds to the wavelength associated to the electron beam, θ corresponds to the angle between the incident beam and the diffracting crystal planes and d corresponds to the interplanar distance. All incident electrons that are scattered by the same atomic spacing will be scattered at the same angle. These scattered electrons can be collated using magnetic lenses to form a pattern of spots; each spot corresponding to a specific interplanar spacing. This pattern can then yield information about the orientation, atomic arrangements and phases present in the examined area.

The inelastically scattered electrons loose energy during their interaction with the specimen and are used for Electron Energy Loss Spectroscopy (EELS) measurements.

At the end of the tube the electrons are collected on fluorescent screens or detected by cameras to generate the image of the specimen.
The resolution of a microscope is defined as the distance between two details just separable from one another.The limit of resolution obtainable in a TEM is around 0.18 nm.

Experimental limitations

Due to the strong interaction between electrons and matter, the specimens have to be rather thin (50-100 nm) to ensure that they allow electrons to pass through. Consequently specimen preparation (especially in case of biological samples) may be long and delicate. Eventualy the electron bombardement may damage some specimens observation if no special care is given to monitoring of electron irradiation parameters: from this point of view biological samples may be quite fragile.

Conclusion

Human and experimental studies indicate that ischemic stroke triggers an inflammatory response that significantly contributes to the neurological outcome. Postischemic inflammatory response is dominated by phagocytic mononuclear cells: i) microglia, immune cells of the brain parenchyma, and ii) macrophages derived from blood, which infiltrate the injured brain tissue.

MRI coupled with injection of USPIOs has recently emerged as a promising tool for cellular imaging of inflammation. However, the ability of this technique to monitor drug effects has yet to be demonstrated. The following study therefore sought to evaluate if therapeutic effects could be monitored by serial USPIO-enhanced MRI in experimental stroke.

Chapter III

Monitoring therapeutic effects in experimental stroke by serial USPIO-enhanced MRI

Marilena Marinescu[1,2], Fabien Chauveau[1,2], Anne Durand[1,2], Adrien Riou[1,2], Anne Dencausse[3], Sébastien Ballet[3], Norbert Nighoghossian[1,2], Yves Berthezène[1,2], Marlène Wiart[1,2]

[1] Université de Lyon, Lyon, France

[2] CREATIS CNRS, UMR 5220; INSERM, U1044; INSA de Lyon; Lyon, France.

[3] Guerbet Group, Research Departement, Aulnay-sous-Bois, France

Submitted to Radiology

I. Introduction

Ischemic stroke accounts for 88% of all stroke cases in industrialized Western societies. To date, thrombolysis using recombinant tissue plasminogen activator (t-PA) is the only efficient treatment for acute stroke approved by Food and Drug Administration.[185] Considering the narrow intervention time-window up to 4.5 hours after stroke onset, only a small percentage of stroke patients are in a position to receive this therapy.[36] Stroke-induced brain damage progresses during the subacute stage up to several days after the attack, causing delayed expansion of the infarction. In addition, cerebral ischemia triggers an inflammatory response that significantly contributes to the neurologic outcome.[69] However, anti-inflammatory treatment has so far failed in clinical trials.[186] In this context, non-invasive imaging of inflammation associated with ischemic stroke lesions could be helpful in selecting and monitoring patients who may benefit from such therapy.

Magnetic resonance imaging (MRI) coupled with injection of ultrasmall superparamagnetic particles of iron oxide (USPIOs) has recently emerged as a promising tool for imaging of inflammation.[122] The USPIOs are ingested by phagocytic cells, whether within the blood-pool or locally at the inflammation site. These cells thus become magnetic and detectable on MRI. USPIO-enhanced MRI has been successfully applied for pre-clinical and clinical studies of cerebral inflammation following stroke.[187] To the best of our knowledge, however, the ability of this technique to monitor drug effects has yet to be demonstrated.

Several anti-inflammatory strategies have been proposed to decrease ischemic damage.[188] Minocycline is currently being evaluated in a clinical trial (Minos, Minocycline to Improve Neurologic Outcome in Stroke).[45] Its anti-inflammatory effects were demonstrated in experimental animal stroke models: minocycline inhibited microglia/macrophage activation (part of the inflammatory response)[46, 49], protected the brain-blood barrier (BBB)[53], diminished oxidative stress[49] and infarct size[49, 52], and extended the thrombolysis therapy time window.[52]

The present study sought to test the hypothesis that USPIO-enhanced MRI could monitor the therapeutic effects induced by minocycline treatment after focal cerebral ischemia in mice.

II. Materials and methods

All animals were treated in strict accordance with international and institutional guidelines.

Study design

Twenty-four Swiss mice were included in the study (weight: 25 to 30 g; Charles River, l'Arbresle, France). The experimental design is detailed in Figure 17. Briefly, on day 0 (D0), the animals underwent permanent middle cerebral artery occlusion (pMCAO, as detailed below). Minocycline (n=12) or its vehicle (n=12) was randomly administered as a 3-dose intraperitoneal injection once every 3 hours starting 5 minutes after pMCAO induction. USPIO contrast agent was administered intravenously 5h after pMCAO. MRI was performed 4h after pMCAO (pre-contrast) and repeated at D1 and D2 (post-contrast). Two quantitative measurements were extracted from the MRI data to compare minocycline-treated versus vehicle-treated animals: i) USPIO brain uptake as observed on transverse relaxation rate maps (R2=1/T2), and ii) R2 change over time. The imaging protocol was followed by animal sacrifice and brain preparation for histology (n=7 in each experimental group) or iron assay (n=5 in each experimental group). All investigators either inducing stroke or assessing MRI and postmortem data were blinded to treatment allocation. Surgery failure, defined by absence of lesion on pre-contrast MRI, was an exclusion criterion.

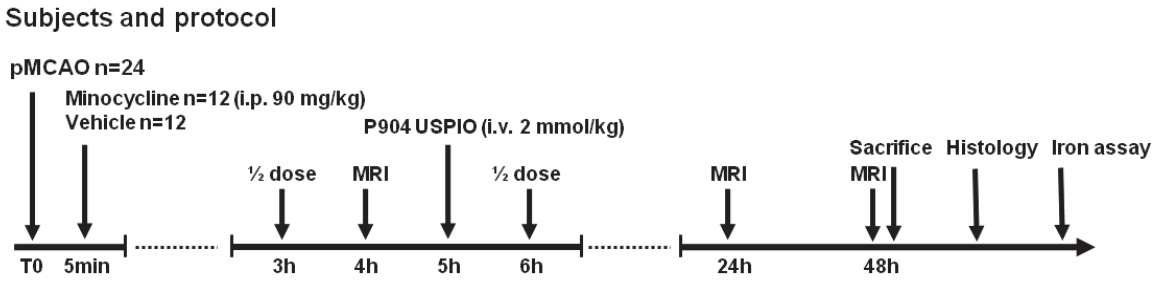


Figure 17*. Experimental design. T0 corresponds to surgery; ½ dose corresponds to 45 mg/kg minocycline administration.*

Animal model

Mice were anesthetized with isofluorane in ambient air. Focal cerebral ischemia was induced as described elsewhere.[189, 190] Briefly, the right MCA was exposed by subtemporal craniotomy and occluded by electrocoagulation. Wounds were then sutured and covered with lidocaine (AstraZeneca, Reims, France) to alleviate pain. During surgery, body temperature was monitored with a rectal probe and maintained at 37°C using a feedback-regulated heating pad.

Treatment

Minocycline is a second generation antibiotic of the tetracycline family. Its half-life in rodents is approximately 2h.[44] Minocycline (Sigma-Aldrich, Lyon, France) was dissolved in phosphate-buffered saline (PBS; 0.1 M, pH 7.4). Three injections were performed intraperitoneally at i) 5 minutes (90 mg/kg), ii) 3 hours (45 mg/kg), and iii) 6 hours (45 mg/kg) after ischemia.[191] Control mice received equivalent volumes (0.1 ml) of vehicle.

Contrast agent

The P904 USPIO contrast agent was provided by Guerbet Research (Aulnay-sous-Bois, France). It is composed of an 8-nm crystalline iron oxide core (maghemite γ-Fe_2O_3) coated with a hydrophilic material for stabilization and biocompatibility. Its mean hydrodynamic diameter is 25 nm (range: 20 to 50 nm). P904 r1 relaxivity is 4 $mM^{-1}s^{-1}$ at 4.7 T in 4% HAS (a medium closed to plasma) at 37°C, and r2 relaxivity is 92 $mM^{-1}s^{-1}$ in the same conditions. A dose of 2 mmol Fe/kg body weight was injected intravenously into the tail vein 5 hours post-pMCAO, i.e. 24h before first follow-up MRI, according to a well-documented protocol.[163, 164, 192]

MRI

Experiments were performed on a 4.7 T/10-cm Bruker Biospec interfaced to a Bruker Paravision 5.0 system. A 50 mm inner-diameter birdcage coil for RF transmission and a 15 mm diameter surface coil for reception were used. The mice were placed on a bed equipped with both ear and bite holders. Body temperature was maintained at 37 ±1°C by an integrated heating system. During image acquisition, anesthesia was maintained using isofluorane 2% in ambient air, and respiration was monitored with a pressure probe. The MR imaging protocol is described in Table 9.

Table 9. MR imaging protocol

Imaging Parameters	Spin-echo T2-WI	Gradient-echo (GRE) FLASH T1-WI	Carr–Purcell–Meiboom–Gill multi-slice multiecho (MSME)
TE / TR (msec/msec)	75/3,500	4/157	15/4,000
Flip angle (degrees)	180	90	180
No. of acquired signals	4	8	8 echoes
Bandwidth (kHz)	50	101	50
Field of view (mm^2)	20x20	20x20	20x20
Slice thickness (mm)	1	1	1
Number of slices	15	15	15
Matrix size	128x128	128x128	64x64

Note: TE = echo time; TR = repetition time; MSME sequence for R2 maps

Animals were not randomized with respect to imaging time, however, they were imaged at the same time at D0, D1 and D2, thus ensuring that data were collected at the same moment post-injury for each animal (see Results).

Histology

After the last MR examination, the animals were deeply anesthetized with isofluorane and decapitated and the brains were dissected out. The brains were then immersed in 4% paraformaldehyde in 100 mmol/L pH=7.4 phosphate buffer for 24 hours at 4°C, bathed for 12 hours in phosphate buffer and kept in 30% sucrose at 4°C until use. When needed, tissues were embedded in polyethylene glycol and cut into 20-µm-thick sections by cryostat. Brain sections were hydrated in PBS and treated with 0.3% hydrogen peroxide and methanol for 10 minutes to exclude any background staining by endogenous peroxidase. Microglia/macrophage detection was performed using a Histostain Plus Bulk kit (Invitrogen). Brain sections were rinsed in PBS and incubated for 10 minutes at room temperature with

serum blocking solution (ready-to-use composition). Rat anti-mouse F4/80 antibody (clone MCA497, Serotec, Oxford, UK) diluted 1/50 in Dako S3022 solvent was applied over the brain sections for 1 hour at room temperature. Sections were then rinsed 3 times in PBS and incubated for 20 minutes at room temperature with a ready-to-use biotinylated secondary antibody solution. After 3 rinses, the sections were treated for 10 minutes with enzyme conjugate followed by another cycle of PBS baths. 50µL diaminobenzidine in 1 mL solvent was used to reveal the activated microglia/macrophage staining. Finally, sections were counterstained with nuclear red so as better to visualize the cytoplasm, and the iron nanoparticles were stained by Prussian blue.

For immunoglobulin deposit detection, brain sections were prepared as previously described [164]. Briefly, biotinylated sheep antimouse secondary antibody was used for brain section incubation, and diaminobenzidine supplemented with nickel ammonium sulfate solution to visualize peroxidase activity.

Brain iron assay

Brain tissue was weighed, and 1 ml of cold water was added per 100 mg of tissue. Homogenization was performed with a Gentle Macs (Myltenyi) device. The sample rested for 2 hours at 4°C to break down the foam produced by homogenization, and then sonicated for 30 seconds at 4°C to lyse the cells completely (so as to remove the effect of compartmentalization of the water). T1 relaxometric measurements were performed at 20 MHz and 37°C (Minispec Bruker). The calibration curve was based on a linear regression of the form: [(1/T1 - 1/T1dia)] / r1 = C. The product of concentration and sample weight provided the amount of iron in the brain. Product R1 in the biological matrix was previously determined by measuring the T1 of non-injected control mouse brain homogenate overloaded with increasing concentrations of P904. The T1dia (diamagnetic) value was derived from measurement in homogenates without injection.

Data analysis

All data were analyzed on a personal computer (1.83 GHz, 2 Gbytes) using MIPAV software (Medical Image Processing and Visualization, NIH, Bethesda, MD, USA; http://mipav.cit.nih.gov/), as detailed below. Apart from lesion volume, all quantitative MRI and histology measurements were made on the central slice of the lesion, at the level of the

corpus callosum (Bregma -1.28 mm, according to Franklin and Paxinos's atlas)[193], where previous studies identified specific USPIO-related changes over time.[164, 166]

MRI analysis

Lesions were manually outlined on T2-weighted images. Volumes were calculated by summation of lesion areas of all brain slices showing brain damage and integration by slice thickness. Brain swelling (increased ipsilateral hemisphere volume compared to contralateral) was assessed by dividing the ipsilateral (IH) by the contralateral hemisphere (CH) value: IH/CH. To avoid overestimation attributable to brain swelling, lesion volume (V) was normalized by the ratio: VxCH/IH.

Transverse relaxation rate maps (R2=1/T2) were generated from MSME native images using MRIUtil software (Penn State Hershey, Hershey, PA, USA; http://www.pennstatehershey.org/web/nmrlab/resources/software/mriutil).

USPIO brain uptake induces hypointense signals on post-contrast T2-weighted images, reflecting higher R2 relaxation rates, which translate in R2 maps as hyperintense signals. Extent of USPIO uptake was defined automatically by thresholding R2 maps so as to encompass the hyperintense zone corresponding to USPIO accumulation areas (Figure 2). A threshold of 35 s^{-1} was applied, based on *in vitro* calibration curves.[194]

Quantitative R2 measurements were made using a 4-pixel (0.39 mm^2) region of interest (ROI) placed on the R2 maps, in systematically identical locations at D0, D1 and D2: (1) in contralateral healthy tissue, (2) lesion core, (3) lesion periphery and (4) the contralateral corpus callosum. The contralateral healthy tissue R2 values were used to normalize those obtained in the other 3 ROIs. Changes in R2 over time were calculated as: $\Delta R2(Di)=R2(Di)-R2(D0)$, with i=1 and 2.

Histology analysis

Extents of F4/80+ cells and BBB permeability to IgG were measured by manually outlining areas of positive staining on respective slices. Count of F4/80+ round-shaped cells was made using a 0.06 mm^2 region of interest placed systematically in the same area in the periphery of the lesion.

Statistical analysis

Statistical analysis was performed with the SPSS 11 statistical software package for Windows (SPSS, Chicago, IL, USA). Data are given as mean values ± standard deviation, and

presented as scatterplots showing individual values. MRI data were evaluated statistically by analysis of variance for repeated measures using the general linear model. Additionnal intra-group comparison (D1 vs D2) was performed using the Wilcoxon signed-rank test. Non-parametric Mann-Whitney tests were used for inter-group comparison of immunohistochemistry at D2. Spearman correlation tests were used to assess the relationship between iron dose and extent of USPIO uptake. P-values less than 0.05 were considered significant for all statistical analyses.

III. Results

MRI

All animals survived the protocol. Three mice were excluded because of surgery failure (1 in the vehicle group and 2 in the minocycline group). In all other animals, surgery resulted in a reproducible focal lesion in the cortex and the dorsal part of the striatum (Figure 18, arrowheads). T2-WI obtained at D1 (23h±2h) and D2 (47h±2h) after USPIO administration showed areas of signal loss in the perilesional area, around CSF compartments (ventricles and velum), and along the ipsilateral corpus callosum, in all mice in both the vehicle and minocycline-treated groups (Figure 18, T2-WI). In half of the animals (7/11 in the vehicle group and 5/10 in the minocycline-treated group), the regions of signal loss extended in the contralateral part of the corpus callosum. Acute transcallosal deafferentation might be responsible for this phenomena.[163] The hypointense signal seen on T2-WI was observed as a hyperintense signal on GRE images at D1, which shifted to a hypointense signal at D2 (Figure 18, GRE, arrows). These observations were in line with those of previous studies studying non-treated animals.[163, 164]

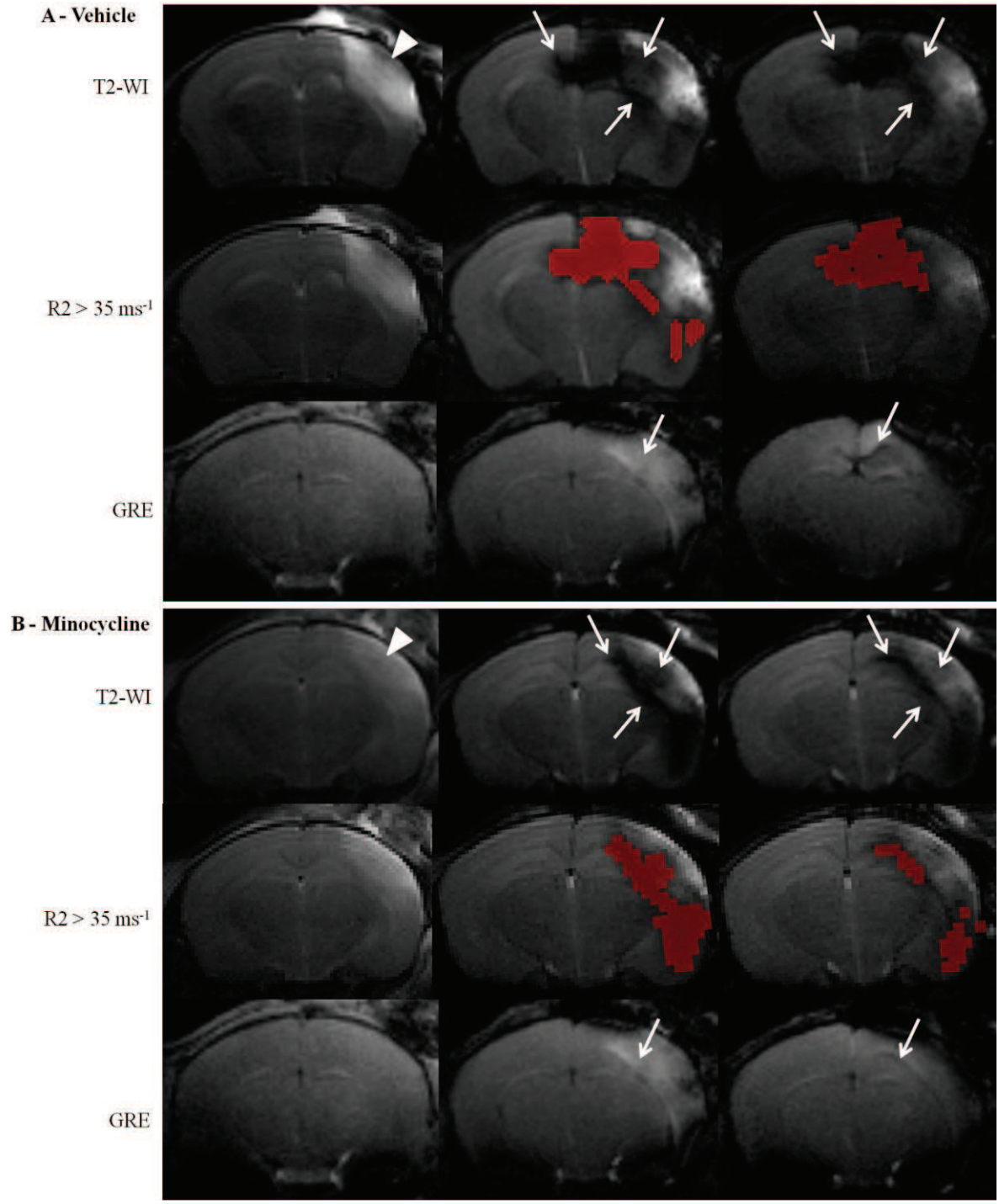


Figure 18. *USPIO distribution over 2 days in a transverse slice through mouse brain (Bregma -1.28, according to Franklin and Paxinos's atlas) observed on multiparametric MRI in a vehicle-treated (A) and a minocycline-treated mouse (B). D0 corresponds to pre-contrast and D1 and D2 to post-contrast data. T2-WI: Note the larger lesion size in the vehicle-treated animal compared to the minocycline-treated animal at D0 (arrowhead) and the marked T2 signal decrease induced by USPIOs in the lesion, the perilesional area, and in the corpus callosum at D1 and D2 (arrows). R2>35 ms^{-1}: Red voxels represent the result of automatic segmentation by thresholding R2 maps. Note how segmented areas visually corresponded to areas of hypointense signals on T2-WI. GRE: Note the transition from hyperintense (D1) to hypointense (D2) signal (arrows), most likely related to USPIOs internalisation. T2-WI: T2-weighted imaging; GRE: gradient echo imaging*

Figure 19 presents lesion volumes and brain swelling, repeatedly measured on D0, D1 and D2, in both groups. Lesion sizes were significantly smaller in minocycline-treated mice than in control mice (p=0.006) (Figure 19A). Brain swelling was also significantly reduced in minocycline-treated compared to control mice (p=0.003) (Figure 19B).

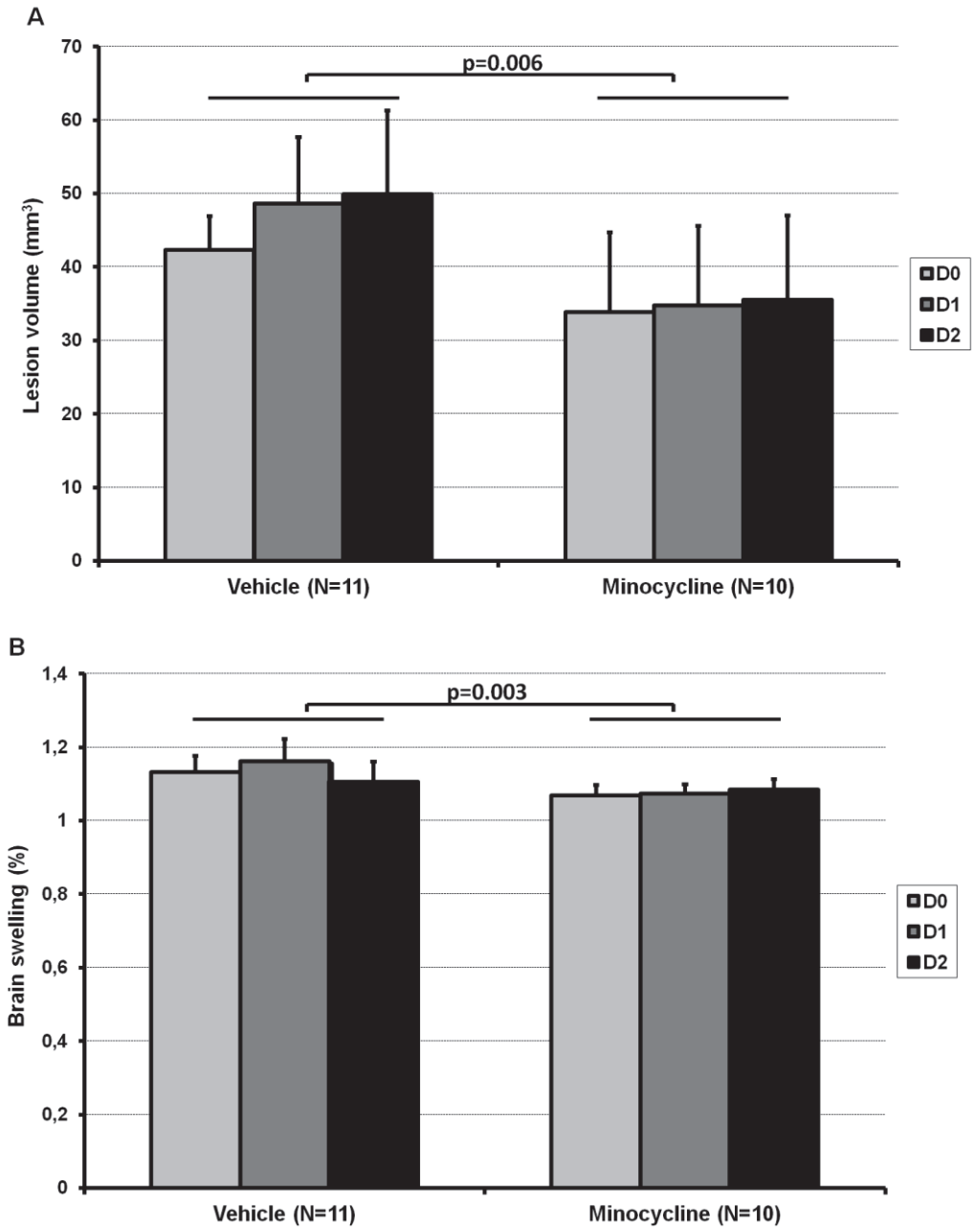
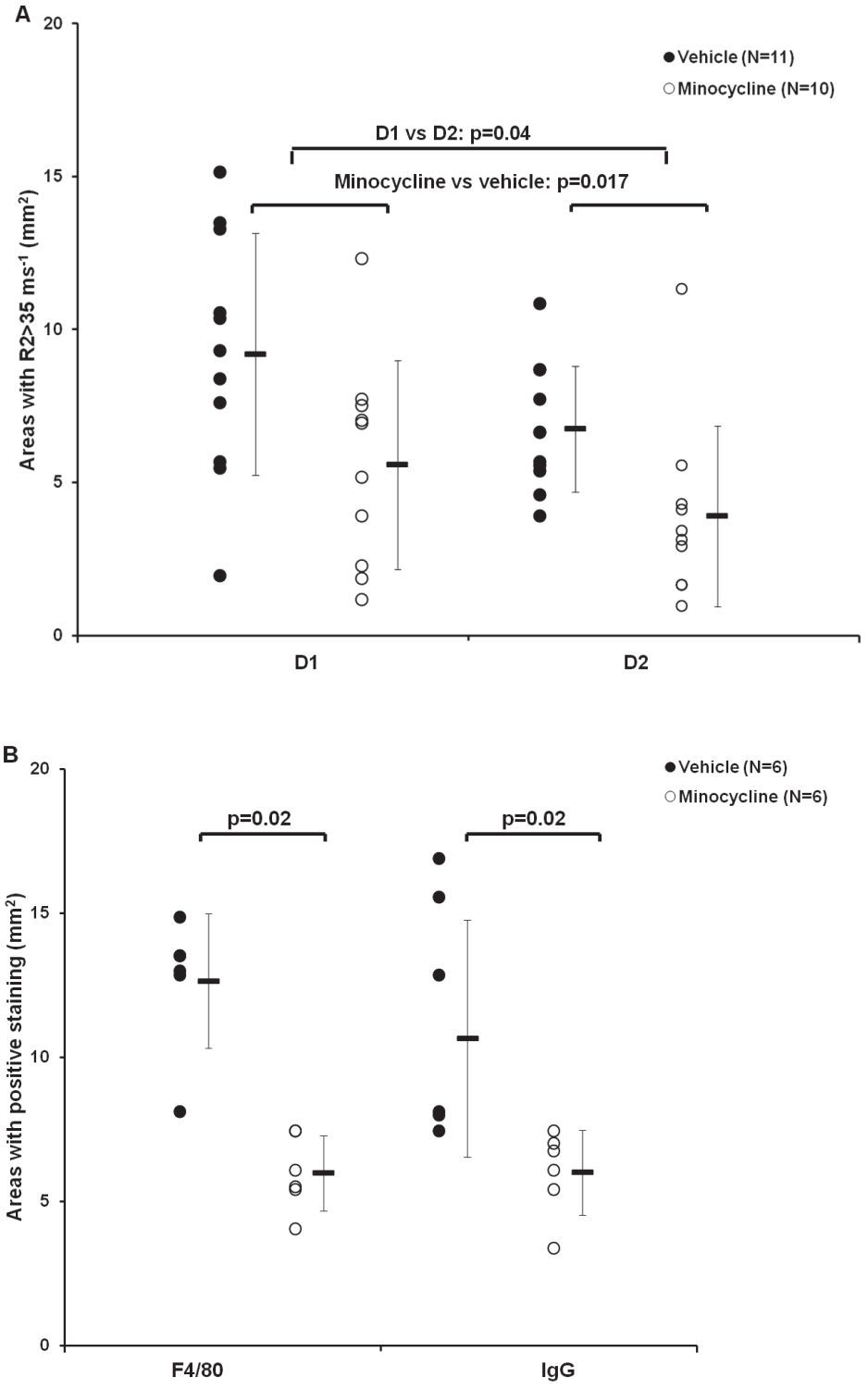


Figure 19. *Evolution in time of lesion volumes (after correction for brain swelling) (A) and brain swelling (B) in vehicle-treated (N=11) and minocycline-treated (N=10) groups.*

USPIO uptake was significantly affected by time and treatment: thresholded areas were lower on D2 than on D1 (p=0.04), and were decreased by minocycline treatment (D1, vehicle: 9±4 mm^2 vs minocycline: 6±3 mm^2; D2, vehicle: 7±2 mm^2 vs minocycline: 4±3 mm^2; p=0.017) (Figure 20A).



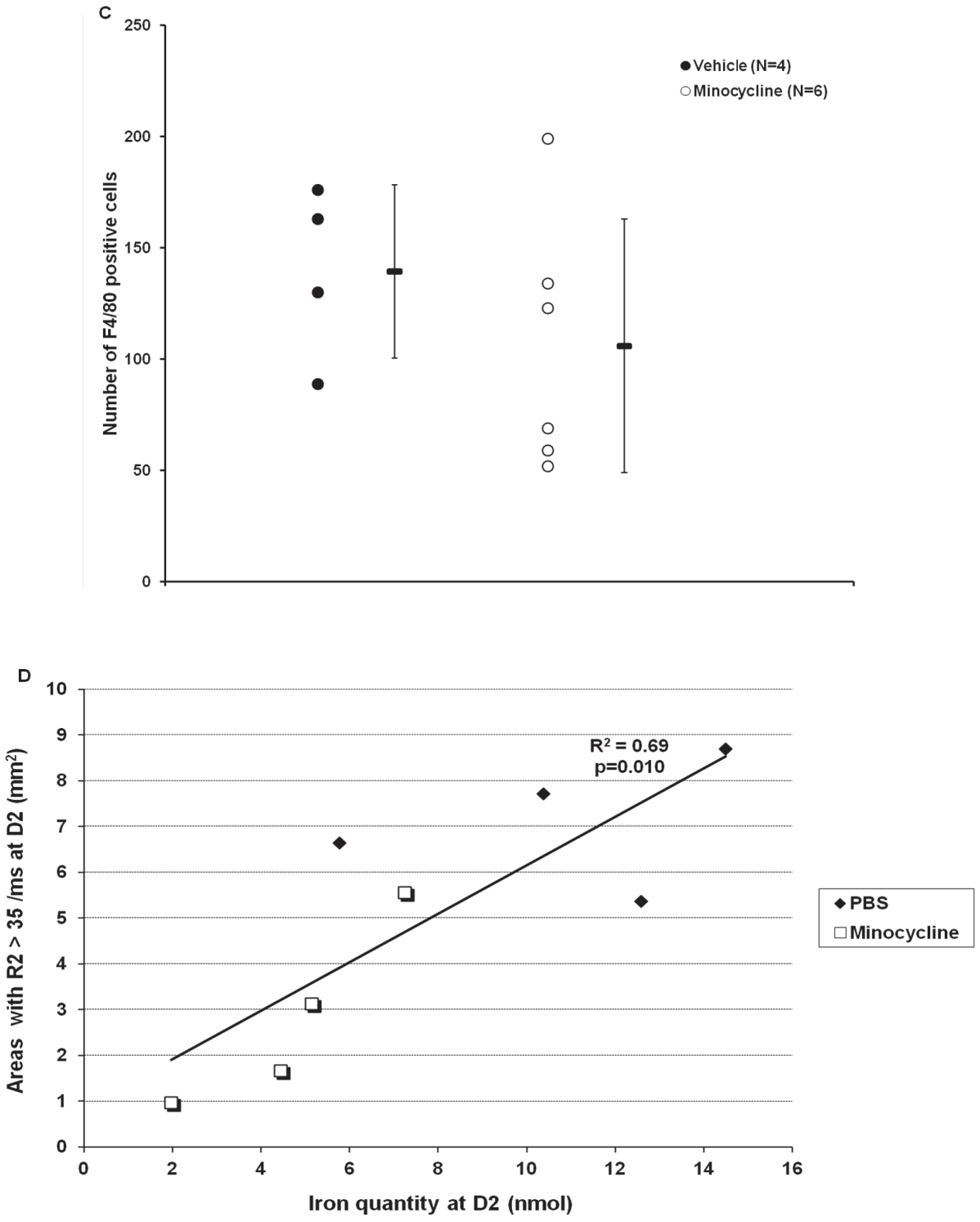


Figure 20. *MRI, immunohistological, and iron assay endpoints (A) Areas of USPIO uptake quantified from thresholding R2 maps at D1 and D2; (B) Areas of F4/80 and IgG staining measured from histological slices at D2. (C) F4/80+ round-shaped cells count at D2; (D) Correlation between postmortem relaxometric iron dosage and R2 maps thresholded areas at D2*

Pre-contrast R2 values in healthy tissue and ΔR2 values are shown in Table 10. R2 values in healthy tissue did not significantly vary over time, indicating that USPIOs had been washed out of the circulating blood by D1. No significant difference between the 2 groups was found at any of the time points in the lesion (p=0.68) or in the corpus callosum (p=0.175). Perilesional measurements tended to show a treatment effect (p=0.063), in addition to a significant time effect (p=0.005). Indeed, deltaR2 values at D2 were significantly decreased compared to D1 values in the vehicle-treated group (p=0.016), but not in the minocycline group (p=0.386).

Table 10. R2 (in healthy tissue) and ΔR2 measurements in s^{-1} given as mean ± standard deviation.

Measure	R2			ΔR2					
Locus	Contralateral healthy tissue			Lesion		Perilesional area		Corpus callosum	
Time point	D0	D1	D2	D1	D2	D1	D2	D1	D2
Vehicle (N=11)	22±2	21±1	20±1	17±15	12±11	13±8	5±3*	18±17	13±9
Minocycline (N=10)	19±2	20±1	20±1	13±14	12±15	7±3	5±5	9±14	8±12

*D2 vs D1, Wilcoxon signed-rank test: p=0.008

Histology

F4/80-positive cells with round morphological features of phagocytic cells were detected in the lesion, on the periphery of the lesion, around CSF compartments (ventricles and velum) and in the corpus callosum, for both vehicle and treated groups (Figure 21A), in co-localization with areas of signal loss on T2-WI. Double staining with Prussian Blue and F4/80 suggested that iron particles were internalized by macrophages (Figure 21, A2 and A3). IgG immunostaining was found in the lesion, the perilesional area, around CSF compartments and in the ipsilateral corpus callosum, in both groups (Figure 21B). Again, these findings reproduced results of a previous study using the same animal model.[164]

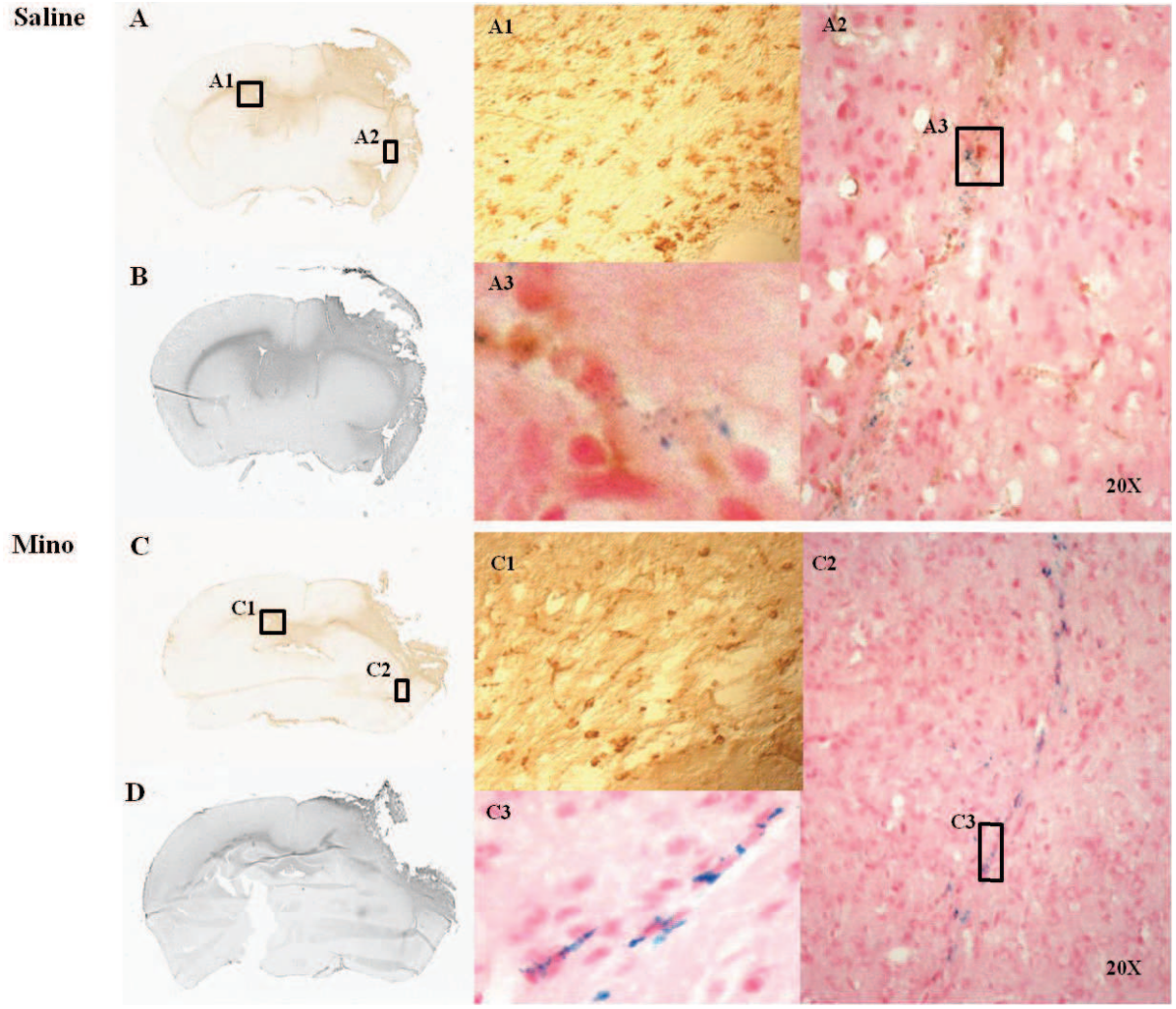


Figure 21. *Representative snapshots of immunohistology in a vehicle-treated mouse (A and B) and a minocycline-treated mouse (C and D). Positive staining can be seen in the lesion, perilesional area, corpus callosum, and around the ventricles with F4/80 immunostaining for microglia/macrophages (A and C) and IgG as a marker of BBB disruption (B and D). Magnification of a region in the corpus callosum shows brown F4/80+ reactive cells (A1, C1). Prussian blue and F4/80 double staining shows multiple Prussian Blue+ spots associated with F4/80+ cells (A2, C2). Prussian Blue staining around nucleus suggests USPIO cell internalization (A3, C3).*

The necrotic part of the lesion tended to fall apart during brain dissection, making quantitative damage assessment difficult. One brain in the vehicle group could not be analyzed, and 6 animals were finally included in each group. Despite this limitation, areas of F4/80+ cells were found to be significantly smaller in the minocycline-treated group (6±1 mm²) than in the vehicle-treated group (13±2 mm²; p=0.020) (Figure 20B). There was also a significant difference in IgG-positive area between the 2 groups (vehicle: 11±4 mm² vs minocycline-treated: 6±1 mm²; p=0.020) (Figure 20B). There were less F4/80+ round-shaped

cells in the minocycline-treated group; however, the difference was not statistically significant (vehicle: 140±39 vs minocycline-treated: 106±57; p=0,352) (Figure 20C).

Brain iron assay

On relaxometric assay, iron uptake in brain tissue was 11±4 nmol in the control group (n=4) and 5±2 nmol in the minocycline-treated group (n=4); this difference did not reach significance (p=0.2). On the other hand, there was a fair correlation between iron assay results and USPIO uptake measured at D2 (Figure 20D, R^2= 0.69, P=0.010).

IV. Discussion

Post-stroke inflammation is a therapeutic target of considerable interest because its therapeutic window is potentially wider than that offered by thrombolysis. Imaging biomarkers are urgently needed to monitor such therapy so as to finely tune the complex inflammatory cascade. Inflammation imaging currently relies on macrophage detection. This can be achieved by PET, using PBR/TSPO radioligands, or by MRI, using iron oxide nanoparticles. As MRI is increasingly used for the management and selection of stroke patients for thrombolysis, surrogate MRI outcome measures are becoming an important component of translational research. We here show, for the first time to our knowledge, that MRI enhanced with USPIO enables monitoring of anti-inflammatory treatment.

Several studies suggested that minocycline treatment could inhibit ischemia-induced activation of microglia through postmortem immunohistochemical staining [46, 53, 111]. Recently, Martin et al. measured a significant decrease in macrophage-specific radiotracer uptake after minocycline treatment in a rat model of transient focal cerebral ischemia [56]. In their study, however, PET data were not validated against immunohistochemistry. The present study combined i) *in vivo* imaging by USPIO-enhanced MRI, ii) *in vitro* measurement of brain contrast-agent uptake on relaxometry, and iii) *post-mortem* detection of both contrast agent and one of its cellular target on immunohistochemistry. As expected, minocycline treatment induced a decrease in: i) lesion size, ii) BBB permeability to IgG, and iii) F4/80 immunostaining for macrophage/microglia.

A significant difference in lesion size was observed at the earliest time point (D0). Although this early time point (4h post-occlusion) was not evaluated in previous studies, this result was not expected, as anti-inflammatory mechanisms are considered to occur later at the acute stage. Alternatively, antioxidant mechanisms, involved in the very first hours after cerebral

ischemia, may explain a difference in lesion initiation between minocycline-treated mice and controls. MRI could not be performed before treatment initiation to check if distribution of initial lesion sizes was similar in each group because delayed minocycline administration shows no significant benefit after insult unlike early administration [49]. To minimize this bias, allocation was randomized and concealed to the investigator responsible for stroke induction, according to STAIR recommendations for preclinical trials [195]. Lesion size was not the primary endpoint of the current work, in which minocycline was chosen because it represented a drug with both anti-inflammatory properties and clinical relevance [196].

In this specific model of pMCAO, USPIO enhancement at 24 hours post-injury has been shown to be mainly caused by nonspecific mechanisms such as BBB leakage, rather than by peripheral phagocyte infiltration [164]. At 48 hours, most iron-related signal changes on MRI are indisputably paralleled by phagocyte-associated iron deposition detected on histology [163]. These phagocytic cells are usually thought to be macrophages [122], although it remains unclear which subtype is labelled, and in which proportion. Again, these questions were not primarily addressed in the present work, which confirmed basic findings of previous studies showing that F4/80+ cells had phagocytized USPIOs at D2 post-injury [164, 197].

Despite these unsolved issues of minocycline mechanism of action, and of USPIO mechanism of labelling, we here present a proof-of-concept study validating USPIO uptake as an imaging index sensitive to treatment. However, to date, a major limitation of the technique is clearly the inability to unequivocally discriminate between multiple drug effects on BBB breakdown and on phagocytic activity. Indeed, it could very well be that the extent of USPIO uptake mainly reflected contrast agent leakage into the brain. USPIO ingestion by phagocytic cells might then appear reduced in the minocycline group only because of reduced availability in the brain. To test this hypothesis, one would need to quantify the amount of free USPIO in the brain at D1. However, this could not be done using histological approaches because of the well-known lack of sensitivity of Prussian blue to interstitial USPIO (as opposed to iron compartmentalized in cells), [164, 198, 199] nor using iron dosages since these do not discriminate between free and compartmentalized USPIOs. Even techniques such as electronic microscopy would only provide a visual assessment about the presence of free USPIOs, not, to the best of our knowledge, a quantitative one.

Conversely, what are the arguments in favor of MRI monitoring of phagocytosis inhibition? USPIO cell internalisation induces a decrease in T2 relaxivity. [200] This effect could explain in part the significant decrease in the extent of USPIO uptake between D1 and D2 observed in

both groups, as in some regions, R2 would then fall below the threshold (see thereafter for discussion of this limitation). The decrease in USPIO uptake extent at D2 might also be influenced by migrating and gathering of iron-labeled cells in chemoattracting regions, such as the lesional and/or perilesional area (as seen in Figure 5 for instance). Interestingly, there was a statistically significant reduction in ΔR2 from D1 to D2 in the perilesional area of the vehicle group, while ΔR2 remained constant in the minocycline-treated group. These findings suggested enhanced local phagocytic activity in the non-treated group. The trend towards lower round-shaped cells in the perilesional area of minocycline-treated mice provided an argument in favor of this interpretation, though studies involving more animals are warrant to confirm this result.

One limitation of the segmentation approach is that the result is dependent on choice of threshold. It is therefore mandatory to apply the technique on maps generated from reproducible quantities such as R2. Both phantom and animal studies showed a linear relationship between R2 and USPIO concentration, [200, 201] so that the threshold can be taken as reflecting a given amount of iron oxide. The healthy mouse brain presents homogenous pre-contrast R2 values (around 20 ms^{-1} at 4.7T) that do not substantially vary from one region to another. However, vasogenic edema in the ischemic lesion induces a drop in pre-contrast R2 (around 8 ms^{-1} at 4.7T). As a consequence, a single threshold for post-contrast R2 may in fact reflect a range of iron concentrations ([1.2 -2.4] mmol Fe/ml for free iron, and 30% less for internalized iron [200]). We therefore checked: 1) that thresholding resulted in areas visually corresponding to hypointense signals on T2-WI and 2) that the resultant extent of USPIO uptake was linearly related to the amount of iron in the brain, as measured postmortem on T1 relaxometry. Another drawback of the thresholding approach is represented by a potential loss of sensitivity for internalized cells in regions with low density of phagocytic cells. Areas of R2 hyperintense signals were smaller than areas covered by F4/80+ cells and IgG+ staining (Figure 4), despite the blurring and partial volume effects of MR images. This may be explained by the fact that manual contouring of histological slices encompassed regions of weak (e.g., lesion core) as well as high density (e.g., perilesional area), whereas automatic segmentation specifically highlighted high-spots.

In summary, since minocycline has a broad spectrum of interdependent therapeutic effects, it should be acknowledged that both decrease of BBB permeability and inhibition of phagocytosis may have influenced the USPIO-enhanced MRI findings. Despite this limitation, one might argue that since future strategies for stroke treatment involve

combination of therapies [202], a functional imaging technique providing synthesized information about two of multiple mechanisms of action might still prove useful in a translational prospect. For example BBB protection by minocycline could reduce damage associated with reperfusion, hence the association with thrombolysis in the Minos study [45]. Although there are still several limitations to overcome for widespread application of the technique in clinical practice (such as elucidating the USPIO entrance route into the brain of stroke patients or defining R2 thresholds in the more complex human brain), **USPIO-enhanced MRI appears to be a promising biomarker for detecting a therapeutic effect in pre-clinical studies.**

Practical applications

Despite encouraging results in pre-clinical studies, anti-inflammatory treatment has so far failed in clinical trials. Our study suggests that MRI coupled with USPIO may allow to better evaluate these therapies in experimental models of stroke, and also to facilitate their translation in the clinics, since some USPIOs are approved in humans.

V. Conclusion

Our study suggests that MRI coupled with USPIO may allow to evaluate anti-inflammatory therapies in experimental models of stroke, and also to facilitate their translation in the clinics, since some USPIOs are approved in humans.

A perspective of future work is to see if the modification of contrast is due to a decrease of inflammation, or to a change in iron microenvironment together with its biotransformation. This analysis is possible by means of MET, an imaging technique capable of descending in resolution up to sub-cellular level. However tissue preparation for TEM visualisation is a time consuming process and it also needs an expert handling. Likewise precise localisation of the nanoparticles is hard due to the scale gap between the excised sample size ($1mm^3$) and the size of the MET sample (50 nm thick).

Some limitations of this method are: i) spatial resolution (78µm in plane) and ii) the local magnetic field created by the iron-labeled cells extending well beyond the actual cell radius making USPIOs precise location and quantification difficult. To overcome these limitations Synchrotron Radiation micro-Computed Tomography (SR-µCT) imaging technique is proposed in Chapter IV. This technique possesses a higher spatial resolution (8µm) than the MRI and is sought to allow a better mapping of the USPIO uptake in the brain.

Chapter IV

Detection of iron oxide nanoparticles in the brain using synchrotron radiation X-ray micro-computed tomography

Marinescu M[1,2], Langer M[1, 3], Durand A [1,2], Olivier C[1,3], Riou A[1, 2], Nighoghossian N[1,2], Berthezène Y[1, 2], Peyrin F[1,3], Wiart M[1,2],

[1] Université de Lyon, Lyon 1, France.

[2] CREATIS CNRS, UMR 5220; INSERM, U1044; INSA de Lyon; Lyon, France.

[3] CREATIS CNRS, UMR 5220; INSERM, U1044; INSA de Lyon; Grenoble, France.

To be submitted to Molecular Imaging and Biology (5-9 December)

I. Introduction

Currently, Ultrasmall superparamagnetic particles of iron oxide (USPIO) are widely evaluated as Magnetic resonance imaging (MRI) markers for the assessment of inflammatory and degenerative disorders associated with high phagocytic activity.[123] USPIO-enhanced MRI is based on the *in vivo* internalization of USPIOs by phagocytic cells, followed by the *in situ* detection of strong MR effects induced by iron-laden cells. This technique has been successfully applied for pre-clinical and clinical studies of cerebral inflammation following stroke.[187] Current limitations of stroke imaging using this approach consist in the difficulty of interpreting post-USPIO MR signal changes. For example, the precise location of iron-labeled cells is hampered by the low spatial resolution (50-100 μm in plane) and by the "blooming" effects (the local magnetic field created by the iron-labeled cells extending well beyond the actual cell radius). Furthermore, quantification of iron-laden cells is a desirable yet unmet goal, because of the non-linear relationship between iron concentration and T2 relaxivity.[203]

In this chapter, we introduce Synchrotron radiation micro-computed tomography (SR-μCT) as a new method to visualize USPIO distribution in the mouse brain. SR-μCT uses monochromatic x-ray beams, allowing acquisition of high-resolution 3D images (5-10 μm) with high signal to noise ratio. This technique also offers the possibility of obtaining a quantification of contrast agent concentrations.[204] To date, the vast majority of studies reported with SR-μCT were conducted on bone specimens.[205-208] To the best of our knowledge, very few studies were performed on soft tissue.[209, 210] The feasibility of detecting cells labeled with iron oxide nanoparticles has been recently established in the myocardium,[211] the muscle[212] and in tumors.[213] We here aim to assess the suitability of coupling MR imaging and SR-μCT for noninvasive dual mapping of USPIO distribution into the whole brain of healthy and ischemic mice.

II. Materials and Methods

Contrast agents

P904 is a prototype USPIO provided by Guerbet (Aulnay-sous-Bois, France). It is composed of an 8-nm crystalline iron oxide core (maghemite γ-Fe_2O_3) coated with a hydrophilic material for stabilization and biocompatibility. Its mean hydrodynamic diameter is 25 nm

(range: 20 to 50 nm). P904 r1 relaxivity is 4 $mM^{-1}s^{-1}$ at 4.7 T in 4% HAS (a medium closed to plasma) at 37°C, and r2 relaxivity is 92 $mM^{-1}s^{-1}$ in the same conditions.

Because of the low cellular uptake of P904,[200] anionic maghemite nanoparticles (AMNP, CNRS UMR 7612, Paris, France) were used for *ex vivo* labeling of macrophages. These are negatively charged superparamagnetic nanocrystals of maghemite with a mean hydrodynamic diameter of 35 nm with a high and non-specific affinity for cellular membrane, enabling efficient cell labeling, as demonstrated in a wide variety of cells.[144] T1 relaxivity is 6 $mM^{-1}s^{-1}$ at 4.7 T in 0.75% agarose gel at 25°C, and T2 relaxivity is 262 $mM^{-1}s^{-1}$ in the same conditions.[214, 215] Generation of bone-marrow derived macrophages and labeling with AMNP resulting in a load of iron of 8 pg/cell were performed according to a previously published protocol.[164]

Phantom study

To evaluate SR-µCT limit of detection for P904, 10 samples of different iron concentrations were prepared using saline solution for dilution. The iron concentrations were: 1,500, 1,000, 500, 150, 15, 1.5, 0.15, 0.015, 0.0015 and 0 µmol Fe/l.

Mouse study

Animal experiments were performed in accordance with institutional guidelines. Twenty-five Swiss mice were included (weight: 25 to 30 g; Charles River, l'Arbresle, France). All experiments were performed under deep anesthesia with isofluorane, while maintaining body temperature at 37°C by a feedback-regulated heating pad. Sutures were covered with lidocaine (AstraZeneca, Reims, France) to alleviate pain.

In a first series of experiment, 16 mice were stereotaxically injected with either free USPIO or USPIO-labeled macrophages at given iron concentrations (as detailed thereafter). Animals were sacrificed one hour after injections and brains were prepared for *post-morte*m imaging with MRI and SR-µCT.

In a second series of experiment, 9 mice underwent permanent middle cerebral artery occlusion (pMCAO). Of these, 8 received intravenous injection of USPIOs 5h after pMCAO at the dose of 2 mmol Fe/kg, according to a well-documented protocol.[164, 190] These mice are the same animals used for brain iron assay in the previous study. The one animal that was not

injected served as control. Mice were imaged *in vivo* by MRI 48h after surgery. They were then sacrificed and their brain was prepared for *post-mortem* imaging with SR-μCT.

Stereotaxic injections

For free USPIO, stereotaxic injections were performed in the right hemisphere (0.8 mm anterior to bregma, 2.0 mm laterally, and 2.5 mm deep from the cortical surface) with 3 μL saline containing a given concentration of iron as shown in Table 1 (5 concentrations x 2 animals per concentration, for a total of 10 mice).

For USPIO-labeled cells, stereotaxic injections were performed in both hemispheres (0.8 mm anterior to bregma, ±2.0 mm laterally, and 2.5 mm deep from the cortical surface) with 3 μL saline containing a given quantity of cells: 10^6, 10^5, 10^4 and 10^3 cells (6 animals, Table 2).

Animal model of cerebral ischemia

Focal cerebral ischemia was induced by as described in the previous chapter. Briefly, the right middle cerebral artery was exposed by subtemporal craniotomy and occluded by electrocoagulation.

Brain preparation

Mice were sacrificed by decapitation. Brains were then extracted, fixed in 4% paraformaldehyde for 12h, bathed in 0,1N phosphate buffer for 12h and placed in a 5ml sealed tube filled with 30% sucrose.

MRI imaging protocol

All experiments were performed on a 4.7 T/10-cm Bruker Biospec interfaced to a Bruker Paravision 5.0 system. A 50 mm inner-diameter birdcage coil for RF transmission and a 15 mm diameter surface coil for reception were used. For *in vivo* experiments, mice were placed on a bed equipped with both ear and bite holders. Body temperature was maintained at 37 ±1°C by an integrated heating system. During image acquisition, anesthesia was maintained using isofluorane 2% in ambient air, and respiration was monitored with a pressure probe. The MR imaging protocol comprised spin-echo T2-weighted images (T2-WI) using a RARE sequence, with time of echo/time of repetition (TE/TR) = 75/3,500 ms and 50-kHz acquisition bandwidth (BW), and T2*-weighted gradient-echo images (GRE) using a FLASH sequence, with TE/TR = 4/157 ms, flip angle 90°, and 101-kHz acquisition BW.

Fifteen axial images were acquired for both sequences with field of view (FOV) 20×20 mm^2, matrix size 128×128, and slice thickness 1.0 mm. An additional T2*-weighted gradient-echo sequence was acquired for *post-mortem* samples using multi-gradient echo (MGE) with TE/TR = 10/300 ms, flip angle 30°, 1 echo, and 80-kHz acquisition BW. Seven coronal slices were acquired with FOV 24.4×24.4 mm^2, matrix size 128×128, and slice thickness 1.0 mm.

SR imaging protocol

All experiments using synchrotron radiation were performed on beam line ID19 at the European Synchrotron Radiation Facility (ESRF) in Grenoble, France. Four acquisition techniques were first tested using a single sample (mouse brain stereotaxically injected with 1,5 mmol Fe/l of free USPIO) in order to establish the more appropriate technique to image our samples: absorption and phase contrast grating interferometry on the one hand; absorption and in-line phase contrast imaging on the other hand.

Setup and tomographic reconstruction for interferometry technique

Imaging was performed with 23.5 keV as described elsewhere.[180] Briefly, the pixel size was set to 7.5µm. Mouse brains placed in a 5 cm tube filled with sucrose 30% were placed on a rotation adapted support and then immersed in an aquarium filled with water. X-ray radiographs were taken and processed using the phase stepping technique, with 4 phase steps per view and an exposure time of 5 s per step. Tomographic data were acquired with 1500 projection angles over an interval of 360°. The tomography data were reconstructed by integrating the projection images line by line and then performing a standard tomographic reconstruction, with a normal filtered back projection (FBP) algorithm.

Setup and tomographic reconstruction for µCT

X-ray phase contrast imaging is a relatively new imaging modality that extends the possibilities of standard (absorption) µCT. Specimens were glued on stands adapted to the rotation stage. Imaging was performed with 17.6 keV selected from undulator radiation using Al filters. The X-ray beam transmitted through the specimen was acquired on a detector using a LuAg scintillator screen, visible light optics and a 2048x2048 CCD detector. The pixel size was set to 8µm, which provides a field of view of 16 mm^3. The detector was positioned at one meter from the sample for the in-line phase contrast imaging. For each specimen, two adjacent scans were acquired in the vertical direction with an overlap of 0.8 mm. Finally, by merging these two data sets, a total reconstructed volume representing 15x15x20 mm^3 was obtained for each specimen. For each scan, 1999 radiographs were taken at different angles

evenly distributed between 0 and 360 degrees. Finally, the Filtered Back Projection algorithm[216] was applied to obtain a reconstructed 3D volume, i.e. a stack of 2048 slices of 2048x2048. Note that since the voxel is isotropic, the slice thickness is equal to the pixel size, i.e. 8 µm.

Phase retrieval was performed from a single phase contrast image at each projection angle using Paganin's method [216]. The d/b (delta/beta)-ratio was set to correspond to the highest concentration of iron particles used in the study. This ratio was calculated using the XPOWER application in the XOP software [217]. The algorithm is implemented in-house at the ID19 beamline at the ESRF to run on graphical processing units (GPU). Images were cropped using the same interval [0.75 -1.05] for all the samples.

Absorption X-ray µCT was employed to image one sample. The same setup as the one for the phase contrast SR-µCT was used, the only difference was the samples distance from the camera (19 mm).

Image analysis

MRI

Regions of hypointense signals and ipsilateral hemisphere were manually outlined on T2-weighted images. Volumes were calculated by summation of areas of all brain slices with regions of interest and integration by slice thickness.

SR-µCT

Regions of hyperdense signals were manually outlined using VGStudio Max 21 on reconstructed phase contrast images. Volumes were calculated by summation of areas of all brain slices with regions of interest and integration by slice thickness.

Brain iron assay

At the end of the imaging session stereotaxically injected with free USPIO and ischemic brains were analyzed for iron concentration as described in the previous chapter (page 67).

Immunohistochemistry

At the end of the imaging sessions, F4/80 and Prussian Blue staining were performed on 20µm brain sections as previously described in the previous chapter (page 66).

Statistical analysis

Statistical analysis was performed with the SPSS 11 statistical software package for Windows (SPSS, Chicago, IL, USA). Data are given as mean values ± standard deviation. Spearman correlation tests were used to assess the relationship between iron concentration and volumes of USPIO. P-values less than 0.05 were considered significant for all statistical analyses.

III. Results

SR-µCT acquisition techniques

Absorption X-ray grating interferometry allowed iron oxide nanoparticles detection (figure 22 a). However the image showed only marginal contrast and no brain structure could be identified due to the similar composition of the different types of brain tissue. Phase contrast grating interferometry provided exquisite brain structure depiction as well as excellent USPIO detection, but with a very long acquisition times (6h) (figure 22 b). Absorption X-ray µCT, typically used for bone structure imaging[207], did not provide a satisfactory image neither of soft tissue nor of the contrast agent (data not shown). Synchrotron radiation X-ray phase contrast imaging (XPCI), an alternative to standard (absorption) SR-µCT imaging is known for its much better discrimination of soft tissues. In this study, it allowed both USPIO detection and identification of brain structures such as ventricles, corpus callosum, and hippocampus layers, in a reasonable amount of time (20 minutes/scan) and was therefore used to image the rest of the samples (Figure 22 c).

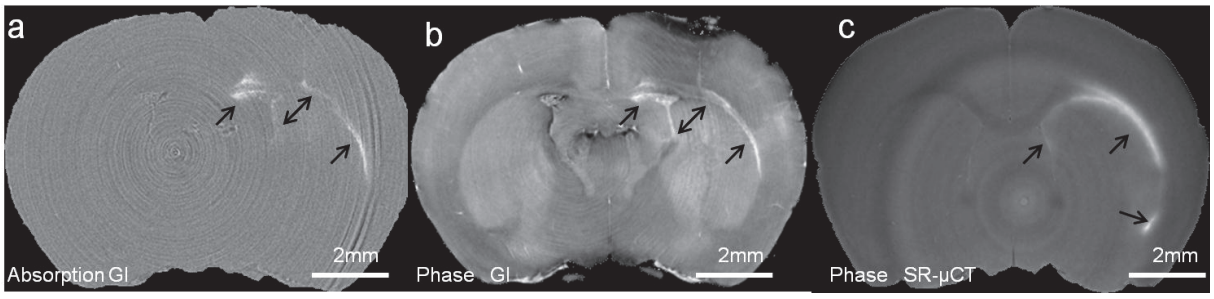


Figure 22. Examples of SR imaging techniques. Absorption (a) and phase contrast (b) X-ray grating interferometry and phase contrast X-ray micro-CT (c) showing a stereotaxic injection of P904 contrast agent in a mouse brain.

Phantom study

Figure 23 shows the relationship between absorption coefficients and iron concentrations on phase SR-µCT images according to the phantom study. As expected, this

relation was linear. A detection limit of $1.5 \cdot 10^{-2}$ µM of iron was derived from these measurements.

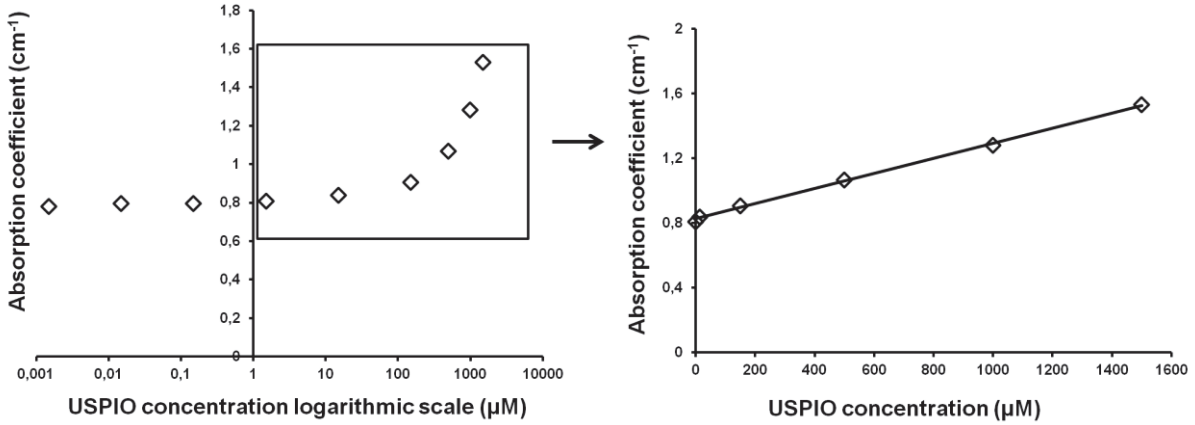


Figure 23. Absorption-iron concentration graphs corresponding to P904 phantoms imaged using SR-µCT. A) Logarithmic scale of USPIO concentrations going from 1500µM to $1.5 \cdot 10^{-3}$ µM. B) Linear relation between iron concentration superior to 10µM and absorption coefficient

Mouse study

- Stereotaxic injections of free USPIOs

Figure 24 shows a series of axial T2-WI (A1, B1, C1, D1, E1), axial T2*-WI (A2, B2, C2, D2, E2), coronal T2*-WI (A3, B3, C3, D3, E3) and SR micro-CT images (A4, B4, C4, D4, E4) of *post mortem* mouse brains injected with free USPIOs. MRI appeared very sensitive for iron detection, with all concentrations inducing large hypointense areas on axial T2-WI and T2*-WI. Coronal T2*-WI showed a cloverleaf artifact typical of signal dephasing caused by USPIOs. XPCI, on the other hand, allowed a visually more precise localization of USPIOs with respect to the brain topography than MRI: it could thus be seen that some contrast agent diffused along needle track, the corpus callosum and the lateral ventricles (Figure 24, arrows). XPCI was sensitive enough to allow detection of all iron concentrations, including the smallest.

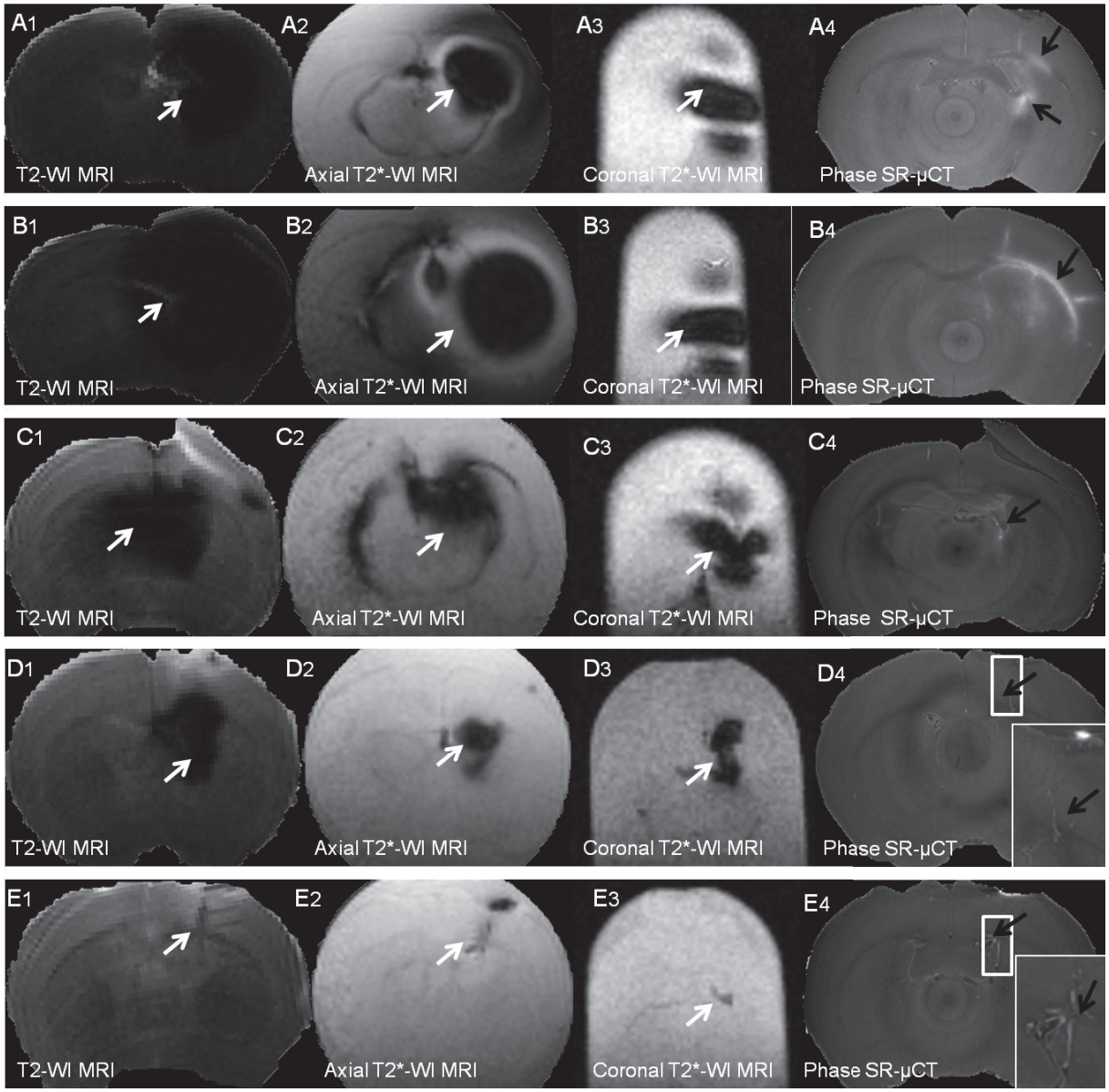


Figure 24. Spin echo T2-weighted MRI (A1, B1, C1, D1 and E1), axial T2-WI (A2, B2, C2, D2 and E2), coronal T2*-WI (A3, B3, C3, D3, E3) and SR-µCT (A4, B4, C4, D4 and E4) imaging of a series of ex vivo mouse brain sterotaxically injected with different concentrations of P904 USPIO. Iron concentrations in µM are: A) 1,500, B) 1,000, C) 500, D) 150, E) 15*

Iron assay revealed that iron concentrations in the striatum differed radically from what was theoretically injected (Table 11).

Table 11- Iron concentration measurements and bi-modality volumes of USPIO uptake for stereotaxic injections of free USPIOs

Theoretical iron concentration in injection vial (μmol Fe/l)	**Measured iron concentration in injection vial (μmol Fe/l)**	**Measured iron concentration in striatum (μmol Fe/l)**	**Volume of hypointense signal (MRI) (mm^3)**	**Volume of hyperdense signal (SR-μCT) (mm^3)**
1,500	1,190	54	34	0,49
1,500	1,363	119	69	1,58
1,000	958	242	83	1,68
1,000	850	411	120	4,90
500	451	10	43	0,16
500	419	8	33	0,25
150	142	1	12	0,23
150	181	7	52	0,01
15	11	0	1	0,25
15	18	1	27	0,05

There was no correlation between signal intensity measured on XPCI and theoretical or measured iron concentrations (Figure 25 A, B).

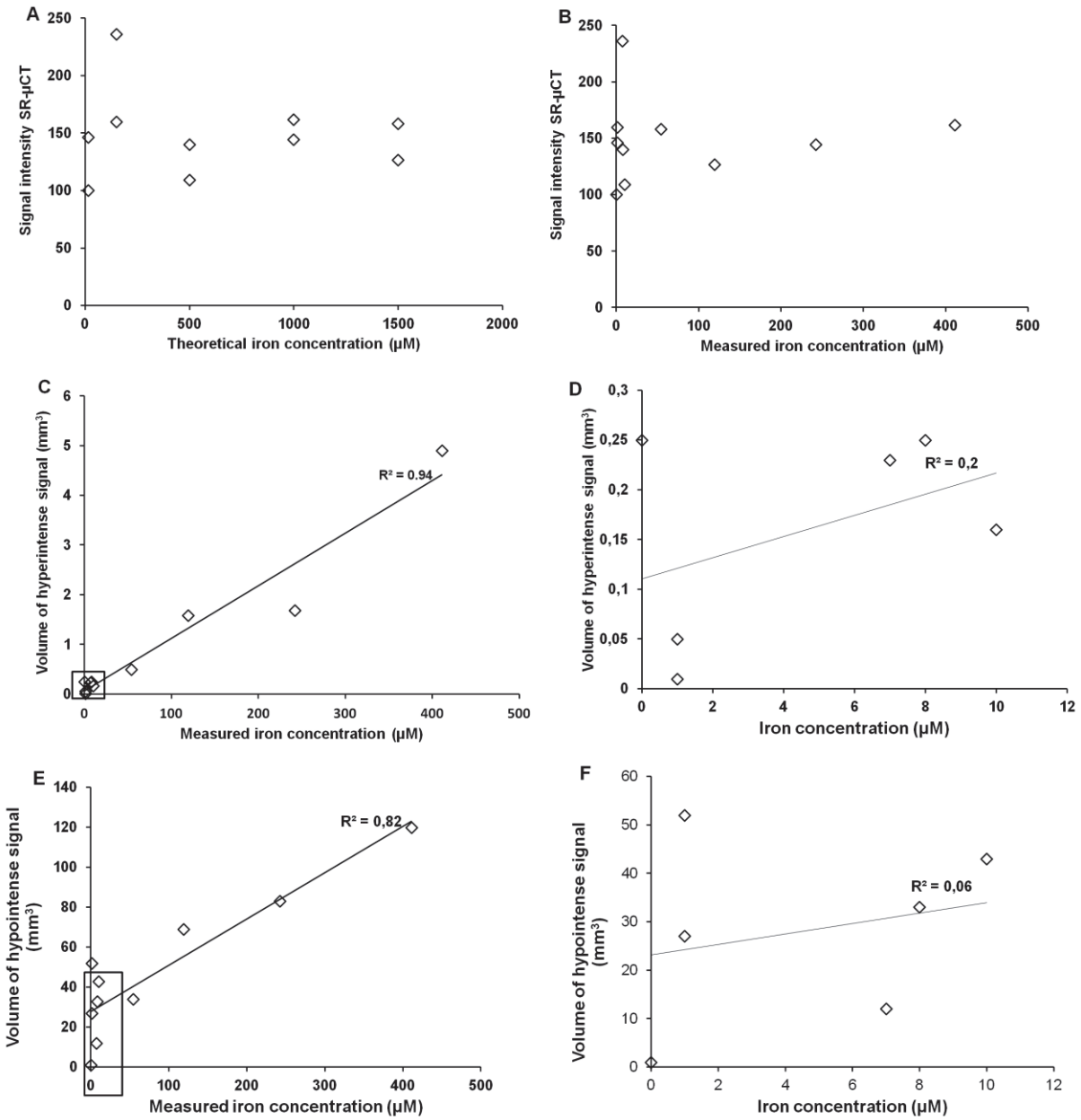


Figure 25. Signal intensity measured on SR-µCT images – theoretical (A) and measured (B) iron concentration graph. C) Volume of hyperintense signal on SR-µCT images-measured iron concentration graph, D) region from graph C, E) volume of hypointense signal on MRI-measured iron concentration graph, F) region from graph E; R^2correspond to Pearson correlation.

Table 11 gives the extent of signals due to USPIO on T2-WI and XPCI for individual animals. The mean extent of USPIO-induced hypointense signals on T2-weighted images was as high as 47 ± 35 mm^3 (32%±21% of the ipsilateral hemisphere), while it was only 0.96 ± 1.51 mm^3 on SR-µCT images. There was no correlation between volumes of USPIO-induced signals and theoretical iron concentrations using either technique. In contrast, there was an excellent correlation between iron concentrations as determined by iron dosage and volumes of hyperintense signals on XPCI (p=0.005; R=0.85) (Figure 25C). However, this correlation relied only on half of the data (i.e. 5 points), the other half corresponding to iron concentrations < 10 µM where correlation was lost (p=0.800; R=0.2) (Figure 25D).

The volume of hypointense signals on T2-WI was linearly correlated with iron concentration (p=0.004; R=0.82) (Figure 25E). This relationship was not verified for iron concentrations < 10 µM (p=0.493; R=0.4) (Figure 25F).

- Stereotaxic injections of USPIO-labeled cells

Figure 26 shows a series of T2-WI (A1, B1), axial (A2, B2) and coronal (A3, B3) T2*-WI and XPCI (A4, B4) of *post mortem* mouse brains injected with USPIO-labeled cells. Again, visual examination showed that extent of USPIO-induced signals on axial T2-WI and T2*-WI far exceeded that of XPCI. As before, XPCI allowed observation of USPIOs along the needle track, the corpus callosum and the lateral ventricles. All cell quantities, including the smallest, could be detected with both techniques.

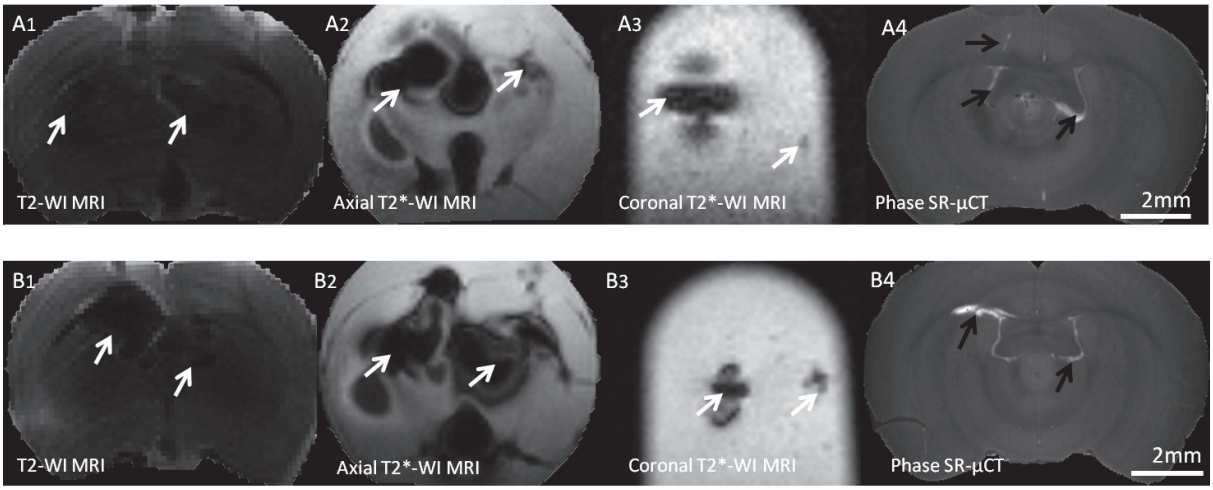


Figure 26. A Spin echo T2-weighted MRI (A1, B1), axial T2-WI (A2, B2), coronal T2*-WI (A3, B3) and SR-µCT (A4, B4) imaging of a series of ex vivo mouse brain sterotaxically injected with different number of AMNP-marked cells. Each brain received two stereotaxic injections corresponding to different number of iron-labeled cells as follow: A) 10^6 cells on the left, 10^3 on the right; B) 10^5 cells on the left, 10^4 cells on the right.*

Because of diffusion along the corpus callosum, it was difficult with this set-up to differentiate signals induced by injection in the left or in the right hemisphere. One injection with 10^6 cells was thus excluded from analysis.

There was no correlation between signal intensity measured on XPCI and theoretical or measured iron concentrations (Figure 27A). Table 12 gives the extent of signals due to USPIO on T2-WI and XPCI for individual animals. The mean extent of USPIO-induced hypointense signals on T2-W images was 34±14 mm^3, while it was only 0.31 ± 0.30 mm^3 on SR-μCT images.

Table 12- Iron concentration measurements and bi-modality volumes of UPSIO uptake for stereotaxic injections of USPIO-labeled macrophages

Number of injected cells	**Theoretical iron concentration (μmol Fe/l)**	**Volume of hypointense signal (MRI) (mm^3)**	**Volume of hyperdense signal (SR-μCT) (mm^3)**
10^6	47,619	54	0.29
10^6		33	0,08
10^5	4,762	64	0,67
10^5		44	0,35
10^5		39	0,19
10^4	47,6	35	0,04
10^4		34	0,1
10^4		21	0,07
10^3	47,6	24	0,15
10^3		20	0,44

There was no correlation between volumes of USPIO-induced signals and number of cells using either technique (Figures 27 B, C). This may be due in part to USPIO-labeled cells injections failure.

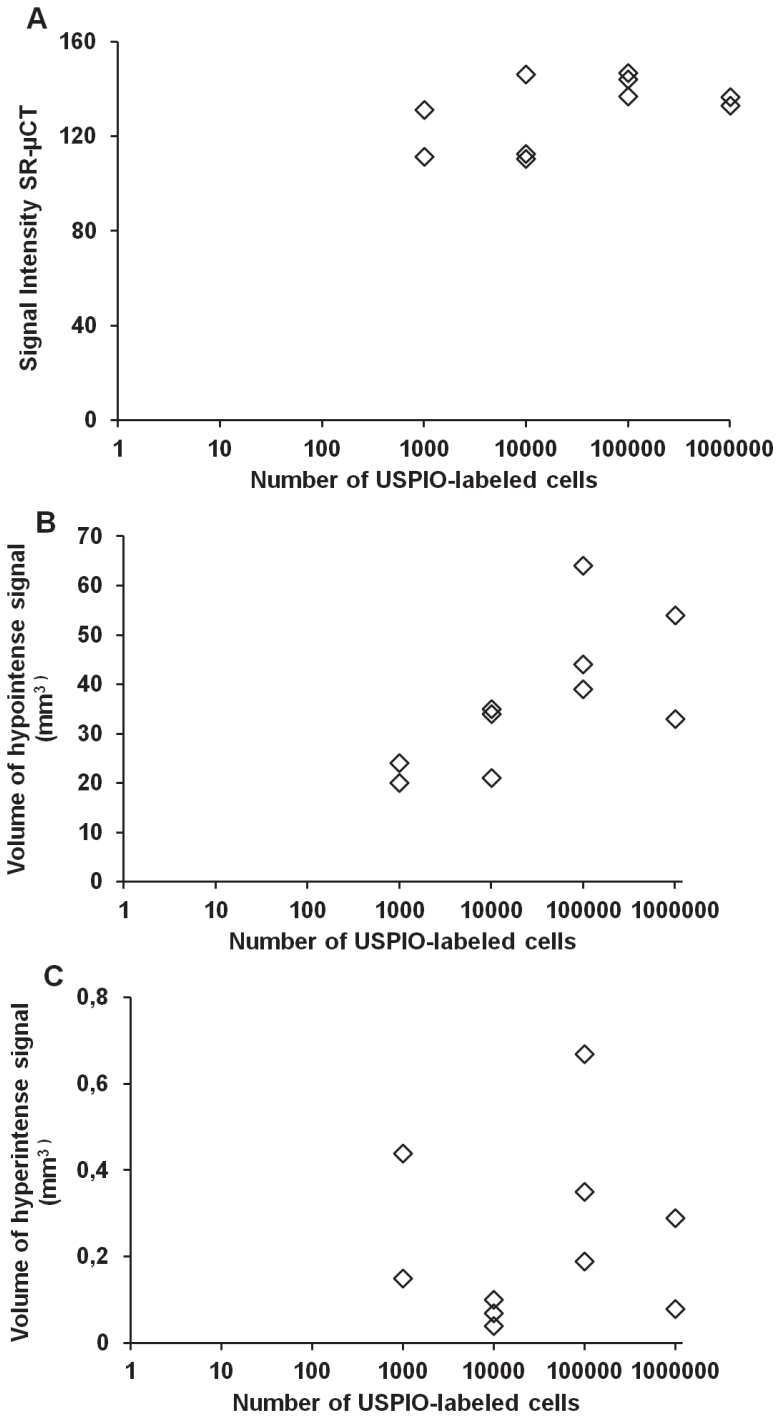


Figure 27. A) Graph corresponding to signal intensity acquired on SR-µCT depending on number of injected cells, B)Graph corresponding to volume of hypointense signal obtained from MRI depending on number of cells, C)Graph corresponding to volume of hyperintense signal obtained from SR-µCT images depending on number of cells

- Animal model of cerebral ischemia

Surgery resulted in a reproducible focal lesion in the cortex and the dorsal part of the striatum that could be seen as a hyperintense signal on T2-WI (vasogenic edema) and as a hypointense signal on XPCI (Figure 28, arrowheads). Two patterns of hypointense signal layouts (corresponding to USPIO presence) were observed on MRI data: i) in the corpus callosum and ii) in the core and periphery of the lesion (figure 28 A1, B1, C1 white arrows). Sparse hyperintense spots were seen on XPCI in the regions of signal loss (figure 28 A3, B3, C3 black arrows). Immunohistology performed in these regions revealed F4/80 positive cells (figure 28 D) with Prussian Blue staining (figure 28 E). Control animal did not show any hyperintense spots in or around the lesion (Figure 28 C3). In pMCAO animals, we did not succeed to specifically delineate hyperintense spots so quantification could not be achieved.

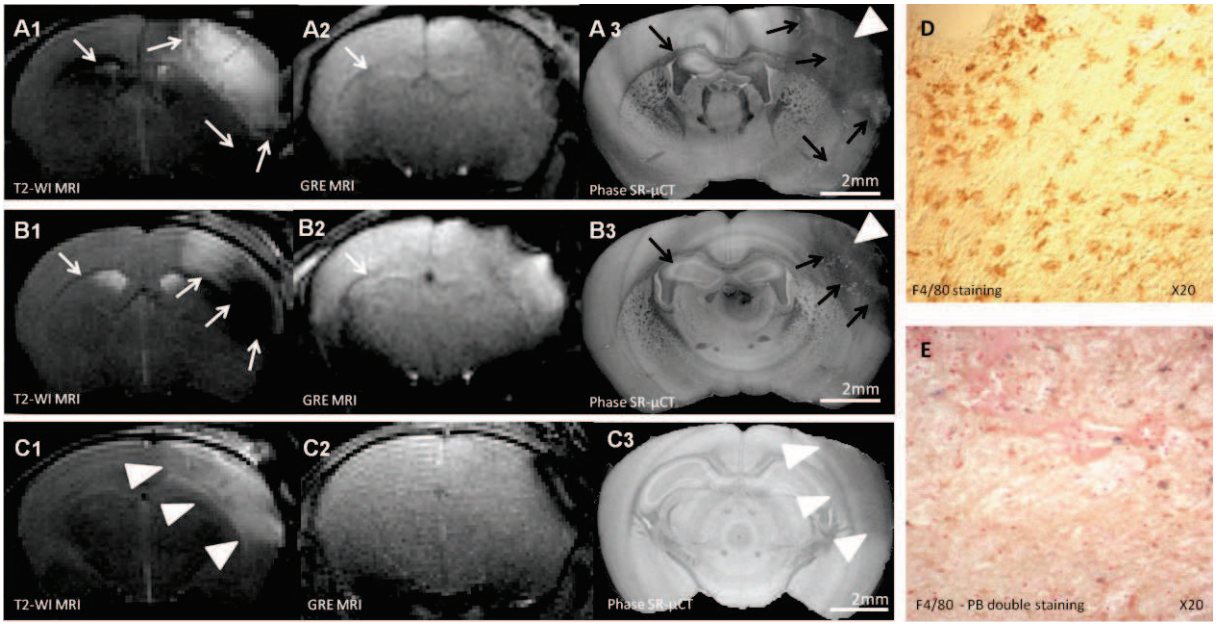


Figure 28. Spin echo T2-weighted MRI (A-C1), GRE MRI(A- C2), SR-µCT (A-C3) imaging and immunohistochemistry (D, E) of two ex-vivo ischemic mouse brains intravenously injected with 2mmol Fe/kg P904 USPIO.

IV. Discussion

In this paper, we have demonstrated how SR-μCT can be used to map cerebral USPIO distribution, in healthy animals and in an experimental model of stroke. XPCI provided sufficient anatomical details as to identify both healthy and pathological brain structures such as the ischemic lesion. The X-ray refractive index of USPIOs was higher than that of brain tissues, allowing their visualization as bright spots in the 2D images. Though this study was performed on *post mortem* mouse brains, data were obtained in an amount of time compatible with imaging in living animals (20 minutes per scan).

We also investigated the sensitivity of XPCI in USPIO detection, and analyzed brain tissues stereotaxically injected with different iron concentrations. The mismatch between iron concentrations that were injected, and iron concentrations that were measured *post mortem* in the brain by relaxometry, was unexpected. One possible explanation is the rapid resorption of the injected solution, most likely by cerebrospinal fluid. This hypothesis was corroborated by diffusion of the solution along the corpus callosum (as previously reported[200]) and by the hyperdense signals observed inside the ventricles. This phenomenon clearly limited the quantitative analysis, by drifting the iron concentrations towards smaller values than what had been planned. Furthermore, quantitative signal intensities did not correlate with measured iron concentrations, probably because of dilution of the solution due to the diffusion process. This underlines the difficulty of designing an experiment to evaluate the quantitative performances of XPCI in the cerebral environment.

Nevertheless, quantitative evaluation of the extent of USPIO uptake appeared as a promising indicator of iron content for concentrations >10 μM. Lower quantities were still detected with both methods, but areas of hyperdense signals were not anymore linearly related to iron concentrations. In summary, both methods showed a potential for quantification of USPIO presence in the brain, but the current setting failed to prove superiority of XPCI over MRI in this prospect. However, XPCI allowed a very accurate visual localization of USPIO, when MRI data showed only potato-like signal loss. In this study, we used the MR sequences that are usually performed for examining stroke-induced animals. The impact of imaging parameters (TE in particular) should be assessed in future studies to better compare the two approaches.

A crucial goal in the development of USPIO-enhanced imaging is to detect the contrast agent in animal models. The low spatial resolution of MR microscopy is compensated by its extreme sensitivity to small quantity of superparamagnetic iron oxide, due to the induction of an inhomogeneous local magnetic field. The dark side of this mechanism is that, in the vicinity of contrast agent, anatomical information is also lost. XPCI in ischemic mice provided a clear depiction of regions with USPIO uptake that were small and disconnected, in agreement with immunohistological slices and in contrast with T2-WI that showed large patches of hypointense signals. Partial volume effects were in part responsible for this, since slice thickness was 1-mm for MR imaging, i.e. ten times that of XPCI. Three-dimensional imaging with isometric voxels is feasible with MRI, however, at the expense of acquisition time. Though hyperintense regions could be readily observed on XPCI, these revealed difficult to delineate, because ischemic lesion signal was heterogeneous.and therefore manual drawing of each spot would have been very time-consuming with these large sets of data. As a consequence, quantitative analysis could not be obtained in the pMCAO model in the current study. Specific post-processing methods using graph-based approaches rather than thresholding,[218] might help overcome this problem (in progress).

In conclusion, XPCI is a new and promising approach to visualize USPIO in the brain. It showed a good sensitivity to USPIO detection, while allowing an accurate localization. We further demonstrated how this method can be used to quantitatively evaluate iron concentration, above a certain threshold. Further studies are warranted to investigate quantitative performance for small quantities of iron, as encountered in animal models of cerebral ischemia. Despite this limitation, we believe that microtomography with XPCI represents a promising tool for future preclinical studies of neuroinflammation, as a complement to USPIO-enhanced MRI.

Chapter V

TEM study of long term spleen storage of P904

I. Introduction

As stated before, our team developed a method to analyze inflammatory reaction in mouse brain after stroke based on in vivo phagocyte labeling with ultrasmall superparamagnetic particles of iron oxide. This approach allowed us to demonstrate non-invasively the progressive extension of the inflammatory response from the infarct to the contralateral hemisphere in focal cerebral ischemia. MR-tracking of phagocytic cells was proved feasible in mice. Furthermore, we showed during this PhD thesis the ability of USPIO-enhanced MRI not only to follow the natural history of the disease but also to monitor therapeutic effects.

The decreased of R2 between D1 and D2 in the first study was interpreted as indicative of ingestion of USPIO by phagocytic cells. However, it raised the question whether the modification of contrast was due to a change in iron microenvironment together with its biotransformation. Thus in this last part of our work, our aim was to study iron oxide nanoparticles at cellular and subcellular level using Transmission electron microscopy (TEM) technique. Unfortunately the scale difference between MRI (78µm in plane) and TEM (0.18 nm) made the tracking of the nanoparticles impossible due to time limitation in this thesis. We have performed tests on brains of mice stereotaxically injected with USPIO, but we failed to detect the nanoparticles in the brain samples prepared for TEM.

To overcome this difficulty, we used the spleen (major recycling organ) as a model to study P904 storage in time with TEM. Since atherosclerosis is a known co-morbidity factor of stroke, the study was performed using Apo-lipoprotein E deficient mice (ApoE -/-). This work was done in collaboration with Adrian Maraloiu at the PMCN laboratory under supervision of Marie-Geneviève Blanchin.

II. Materials and methods

All animals were treated in strict accordance with international and institutional guidelines.

II.1 Contrast agent

The P904 USPIO contrast agent was provided by Guerbet Research (Aulnay-sous-Bois, France). It is composed of a 6 to 8-nm crystalline iron oxide core (maghemite γ-Fe_2O_3) coated with a hydrophilic material for stabilization and biocompatibility. Its mean hydrodynamic diameter is 25 nm (range: 20 to 50 nm).

II.2 Study design

In this study, we aimed to assess the spleen outcome of P904 intravenously injected to mice. TEM analysis of P904 solution was made before administration. Four mice (ApoE $^{-/-}$, C57BL/6 background) received from Guerbet Research, France were included in the study. Animals were started on a high-fat diet (Western Diet, 0.5% cholique acid and 1.25% cholesterol) at 6 weeks of age. At 28 weeks of age animals were intravenously administered a dose of 1 mmol Fe/kg of P904 contrast agent. Mouse spleens were harvested at different time points after USPIO administration: i) 3 hours, ii) 2 days, iii) 20 days and iv) 40 days and prepared for TEM visualization.

II.3 Sample preparation for TEM visualization

Spleen samples were obtained following a chemical protocol of mammalian tissues preparation. Several steps were made as detailed below, including: i) tissue sampling, ii) fixation and postfixation, iii) dehydration in alcohol baths of increasing concentrations, iv) inclusion in Epon resin. Afterwards, 50 nm sections were cut out of the resin blocks with a microtome apparatus. These sections were placed on a Formvar or carbon film coated grids and stained with heavy metals before TEM observation. All the chemical products used met the pH of the cells.

In brief, mice were dissected; spleen was removed and placed in a Petri dish containing a fixative solution (2 ml of 1.5% glutaraldehyde and 1% paraformaldehyde in 0.15 M cacodylate buffer). Under a dissecting microscope, 1 mm^3 samples were recovered and placed in the fixative solution for four hours at room temperature. Afterwards the ex-vivo tissues underwent four successive 0.15 M cacodylate buffer baths (15 minutes each bath) and then a 12 hours bath in the same buffer. The following step was the 45 minutes osmium tetroxide (OsO_4) bath. Then the tissues were immersed in distilled water before starting the dehydration. The purpose of dehydration was to replace the aqueous solutions with solvents miscible with the resin. After a quick wash with distilled water, dehydration was performed at room temperature in seven alcohol baths of increasing concentration as follows: i) one 5 minutes baths for 30º, 50º, 70º, 95º and ii) three 10 minutes baths of 100º alcohol. Dehydration was completed with two 10 minutes baths in pure propylene oxide. Samples were immersed in a resin (Epon A, Epon B, BMDA catalyzer (1.7% of the mixture A + B)) and pure propylene oxide mixture for one hour to substitute the alcohol with the resin. The

impregnation was carried out in the epoxy resin for one hour and then a 12 hours baths followed. Next, another one hour freshly prepared epoxy resin bath was done. Finally, samples were placed in moulds and covered with a freshly prepared impregnation mixture. Hard blocks of resin containing the spleen tissue were obtained after polymerization at 37°C for one day followed by a three days polymerization at 60°C.

Ultrathin sections were obtained from the resin blocks by means of Reichert-Jung (Leica) Ultra-cut 701701 ultra-microtome. The sections were deposited on nickel or copper grids coated with Formvar or carbon film. One day before TEM observation the grids were stained with uranyl acetate (10 minutes) and lead citrate (5 minutes).

II.4 TEM visualization

Tissue and solution samples were placed on 3 mm TEM grids and observed using a TOPCON EM-002B microscope with 0.18 nm point to point resolution, a range of magnification between 980 and 6.10^5, at a 200 kV accelerating voltage. The modes used were: conventional transmission electron microscopy (CTEM), high resolution transmission electron microscopy (HRTEM) and selected area electron diffraction (SAED).

III. Results

- *Iron oxide nanoparticles characterization before administration.*

CTEM image (figure 29 a) gives an overview from a set of P904 nanoparticle as received from the manufacturer dispersed on a carbon film grid. A typical HRTEM image (figure 29 b) of these nanoparticles reveals the atomic arrangement within particles. Furthermore, SAED diagram in a selected area (Figure 29a) shows that the core of the nanoparticles is crystallized in the maghemite structure. The size distribution analysis reproduced in figure 29 (d) reveals that most of the nanoparticles (65%) exhibit a diameter between 6 and 9 nm, thus confirming the information provided by the manufacturer.

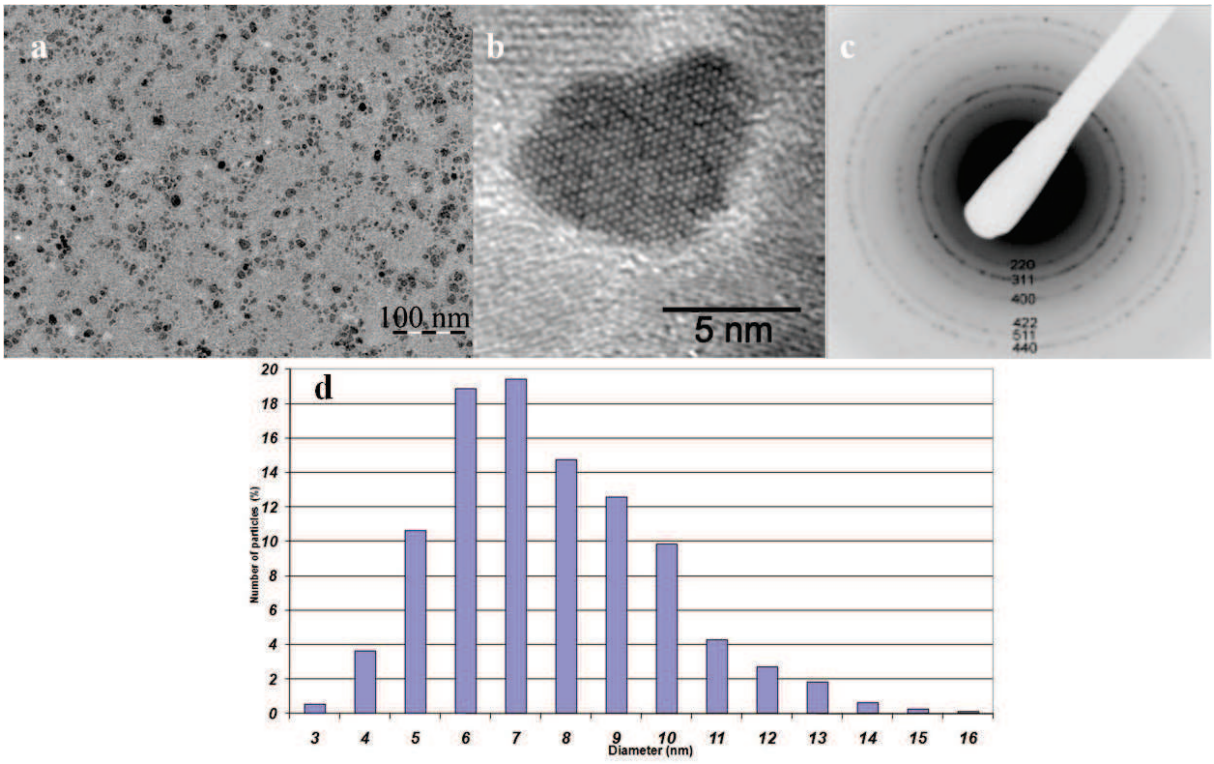


Figure 29. Transmission electron microscopy analysis of P904 before administration. Conventional (a) and high resolution (b) TEM images of P904. Selected area electron diffraction (c) showing the maghemite structure of USPIO. (d) size distribution of nanoparticles showing the mean core size of 7 nm.

- *Characterization of the P904 in spleen tissue*

At the cellular scale, images recorded from the spleen harvested three hours and two days after P904 intravenous administration showed nanoparticle agglomerations into a few cells, likely macrophages. At the subcellular scale, quite large densities of nanoparticles were observed into intracellular lysosomes like in figure Figure 30A. Corresponding SAED patterns points out structural parameters consistent with the maghemite structure (figure 30, A1). At day 2, some of the vesicle-like substructures exhibited electron-dense contrast and other ones blanker contrasted corresponding to more monodisperse nanoparticles (figure 30B). The nanoparticles in the electron-dense area were well crystallized in the maghemite structure as shown by the corresponding SAED patterns (figure 30 B1). SAED patterns from the border and central region of C were all as reproduced in C1. Loss of electron density and ring configuration in the pattern suggested transition between maghemite and a more poorly-crystalline structure, most probably ferritine (figure 30 C1). This last assumption is

consistent with the features of the nanoparticles seen in C, which exhibited a smaller average size together with a weaker image contrast.

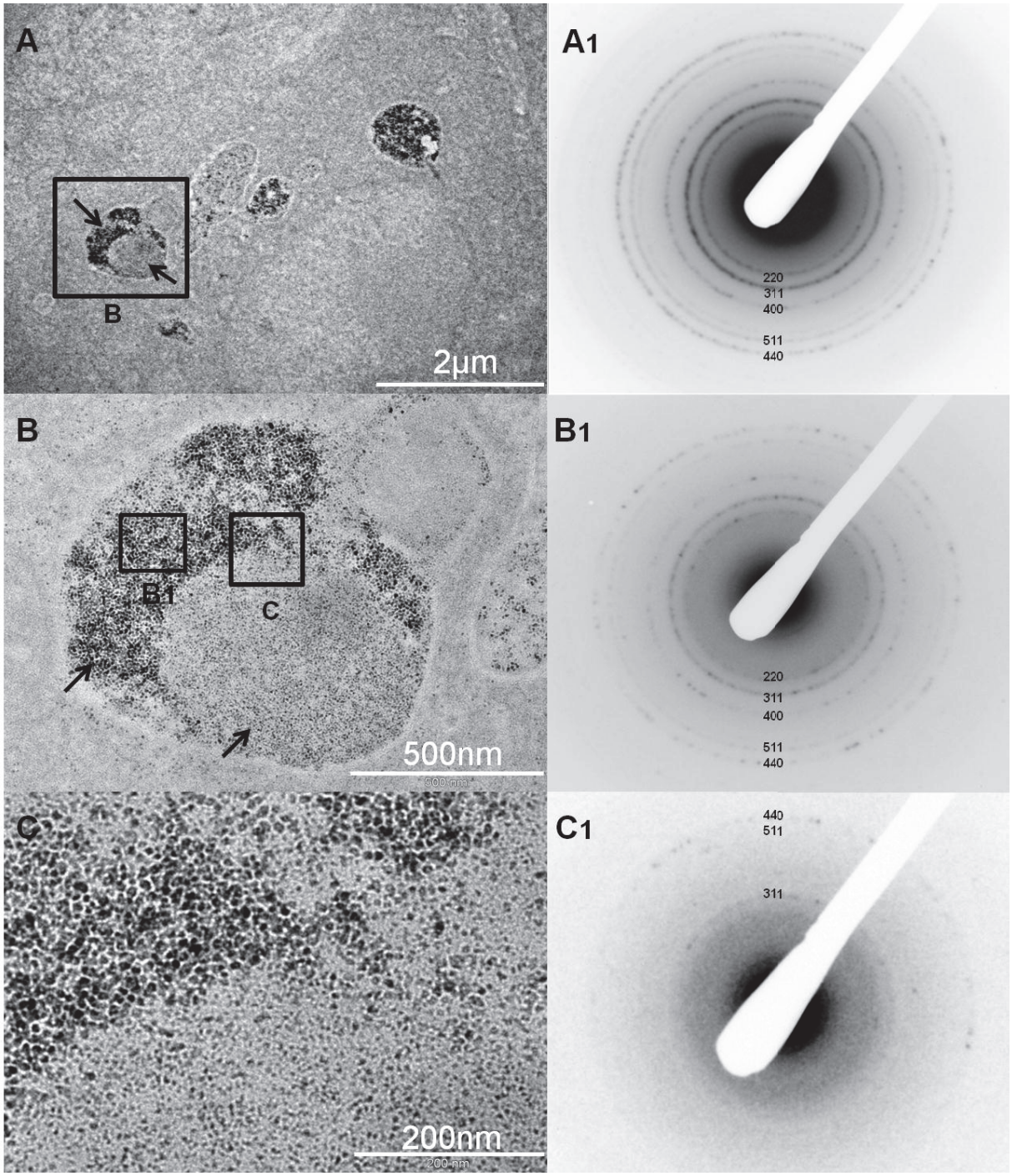


Figure 30. CTEM and SAED observations of a mouse spleen harvested at day 2 after administration of P904 USPIO. Image A corresponds to an overview of nanoparticle agglomerations, A1 corresponds to its diffraction pattern. Image B corresponds to an enlargement of the area B outlined in A, B1 corresponds to the diffraction from the darker zone in B. Image C corresponds to an enlargement in the area C outlined in B, (C1) SAED from (C). Note the difference in density of dark spots on diffraction rings in A1, B1 and C1.

Agglomerations of P904 nanoparticles were also found at longer periods of time after contrast agent administration (30 and 40 days). The pattern of nanoparticle localization (inside the lysosomes of sparse cells) was rather similar compared to early days post-injection. “Some vesicles” still contained electron-dense clusters of nanoparticles, while others ones in the vicinity contained more dispersed ones in the same vicinity (Figure 31). As before, diffraction pattern from electron-dense areas corresponded to maghemite structure (Figure 31b), while diffraction rings in SAED pattern like in figure 31A were more discontinuous as expected from more disperse particles.

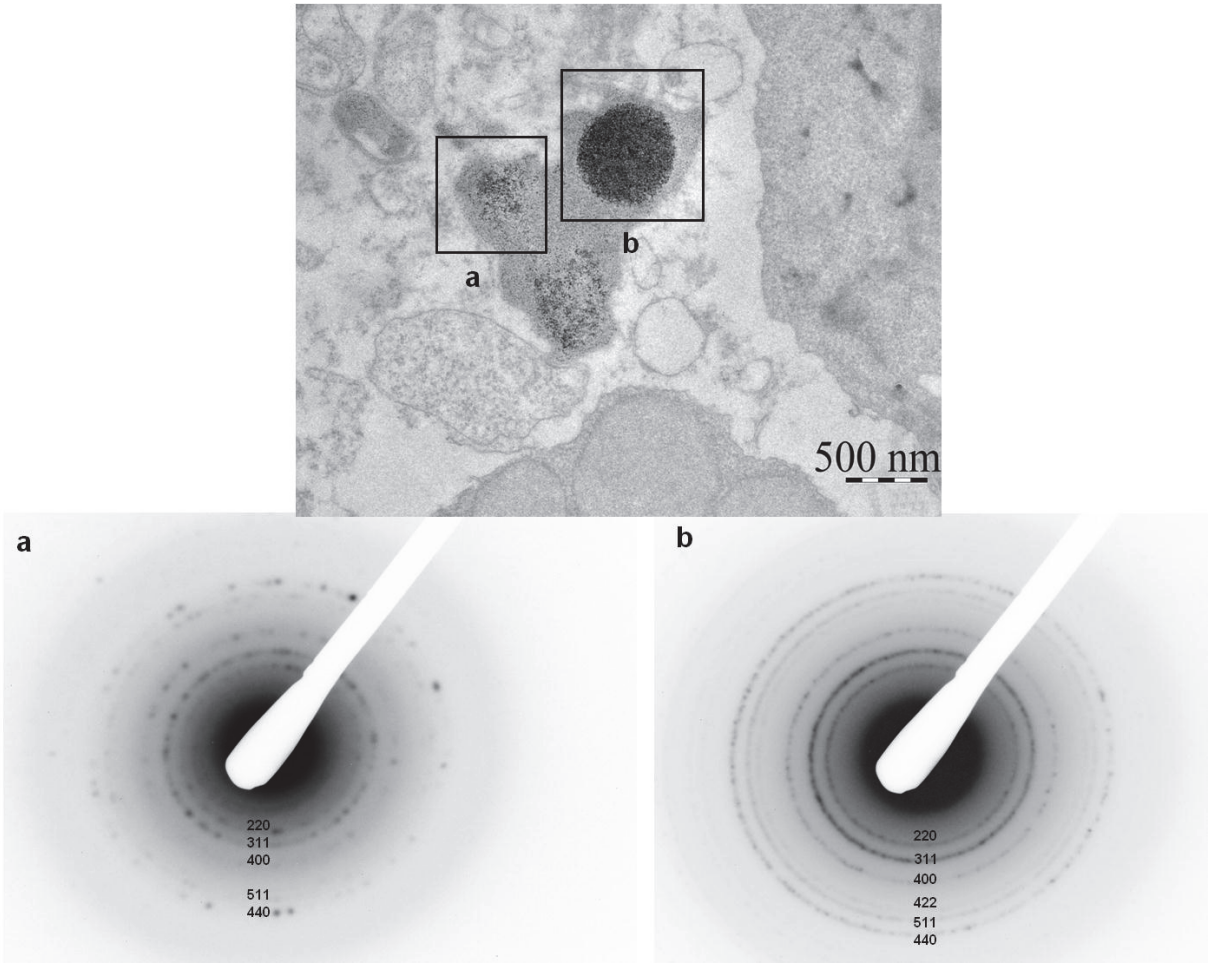


Figure 31. CTEM and SAED (a, b) from a mouse spleen harvested 40 days after administration of P904. Groups of nanoparticles with different electron density and their corresponding SAED (a, b). Note the density difference in density of dark spots on the diffraction rings between the two diffraction patterns..

IV. Discussion

In this study, we have performed a nanoscale structural analysis of mice spleen by electron microscopy for up to 40 days after intravenous administration of USPIO. Clusters of P904 nanoparticles sequestered into cellular lysosomes were found at all time points. From D2 post-injection, electron-dense areas with diffraction pattern of maghemite and more dispersed areas with less-defined diffraction pattern co-existed in many lysosomes. These findings suggested local continuous biotransformation of iron oxide nanoparticles, most probably into ferritine as reported by Lopez-Castro et al. determination of the ferritine structure in nanoparticles is more surely achieved by STEM-HAADF electron microscopy.

These present results are in agreement with the frame of a study by Levy M. et al,[182] which studied P904 nanoparticles in healthy mice (C57Bl6, the background of ApoE-/- mice) and in an obese mouse model using the same high dose of 1000 µmol Fe/kg, with a multimodal approach that included TEM. In their study, intact nanoparticles of P904 were still present in the spleen 3 months after their intravenous injection. The recycling of iron into ferritine thus seems to be a slow and long process, that might be additionally dependent on the availability of iron storage chelates.

They are several limitations to this study. Firstly, we did not include any healthy animals, therefore it was not possible to determine whether structural changes in ApoE-/- mice were different from that of healthy animals. Secondly, the present TEM approach is structural but qualitative because limited and further coupling with quantitative methods such as Ferromagnetic Resonance (FMR) and superconducting quantum interference device (SQUID) would be needed in order to determine the kinetics of P904 biotransformation as in [182]. For example, the current setting did not allow us to conclude about an increase or a decrease of USPIO in the spleen with time. Thirdly, we studied the spleen only, while it is well-known that liver plays a crucial role in USPIO metabolism. In fact, Levy et al hypothesized that a majority of P904 nanoparticles were processed in the liver, with products of degradation being transferred to the spleen to increase the iron storage tank. Additional investigation is therefore necessary to corroborate this hypothesis with our data.

In conclusion, this work gave evidence of the degradation of USPIO in the spleen of ApoE-/- mice. The fact that this process takes time provides new and interesting insights into

our previous works, since spleen (as well as liver) could act as a reservoir for iron-labeled cells, which might migrate to the brain following injury.

Conclusion and perspectives

Cerebral ischemia research is oriented toward improving clinical patient care. In this regard, the aim of numerous specific preclinical studies, performed on animal models, is the development and the evaluation of novel contrast and pharmaceutical agents. The work presented here integrates this concept by a multimodal approach using:

1. USPIO-enhanced MRI to monitor a therapeutic effect of a treatment;
2. SR-μCT imaging technique for a more precise mapping of USPIOs
3. TEM for cellular and subcellular assessment of iron bio-transformation.

Inflammation is a complex process and imaging of neuroinflammation is obviously a challenging objective. Though USPIO-enhanced MRI has brought a lot of promises in this field, there are still a number of unanswered questions related to the exact mechanisms involved: for instance how USPIO are taken up into the brain, which cell type or subtype are labeled, how long does the labeling persists.... Though we did not directly address these questions in our work, we believe that a multimodal and multiscale approach as developed here might help answer these questions in the future. However, for the time being, the difficulty to go back and forth between the different scales remains a clear limitation. Each technique necessitates a given preparation and therefore the same sample cannot be imaged with SR-μCT and TEM for example. Therefore there is a need to design protocols providing very reproducible data in order to compare observation in the very same locations. We have seen during this thesis that this was not easy when working with living animals, even with stereotaxic injections. Segmentation and quantification of the effects of USPIO also appears as a difficult goal, although mandatory for statistical analyses. More investigations are clearly needed to demonstrate the potential of SR-μCT for mapping neuroinflammation and these will most certainly rely on the development of robust algorithms allowing to efficiently process large volumes of data. Also *in vivo* imaging with this technique should be feasible and might provide exciting monitoring of animal models of stroke. The better depiction of iron location may then help sample the brain to study USPIO at the nanoscale with electron microscopy. All together, these approaches should provide a better understanding of USPIO-enhanced MRI, which is still crucially needed for translation into the clinics at a larger scale.

References

1. Hatano S. Experience from a multicentre stroke register: A preliminary report. *Bull World Health Organ*. 1976;54:541-553
2. Roger VL, Go AS, Lloyd-Jones DM, Adams RJ, Berry JD, Brown TM, Carnethon MR, Dai S, de Simone G, Ford ES, Fox CS, Fullerton HJ, Gillespie C, Greenlund KJ, Hailpern SM, Heit JA, Ho PM, Howard VJ, Kissela BM, Kittner SJ, Lackland DT, Lichtman JH, Lisabeth LD, Makuc DM, Marcus GM, Marelli A, Matchar DB, McDermott MM, Meigs JB, Moy CS, Mozaffarian D, Mussolino ME, Nichol G, Paynter NP, Rosamond WD, Sorlie PD, Stafford RS, Turan TN, Turner MB, Wong ND, Wylie-Rosett J. Heart disease and stroke statistics--2011 update: A report from the american heart association. *Circulation*.123:e18-e209
3. Pendlebury ST, Rothwell PM. Prevalence, incidence, and factors associated with pre-stroke and post-stroke dementia: A systematic review and meta-analysis. *Lancet Neurol*. 2009;8:1006-1018
4. Strong K, Mathers C, Bonita R. Preventing stroke: Saving lives around the world. *Lancet Neurol*. 2007;6:182-187
5. Murray CJ, Lopez AD. Global mortality, disability, and the contribution of risk factors: Global burden of disease study. *Lancet*. 1997;349:1436-1442
6. Johnston SC, Mendis S, Mathers CD. Global variation in stroke burden and mortality: Estimates from monitoring, surveillance, and modelling. *Lancet Neurol*. 2009;8:345-354
7. Heidenreich PA, Trogdon JG, Khavjou OA, Butler J, Dracup K, Ezekowitz MD, Finkelstein EA, Hong Y, Johnston SC, Khera A, Lloyd-Jones DM, Nelson SA, Nichol G, Orenstein D, Wilson PW, Woo YJ. Forecasting the future of cardiovascular disease in the united states: A policy statement from the american heart association. *Circulation*.123:933-944
8. Powers WJ, Grubb RL, Jr., Raichle ME. Physiological responses to focal cerebral ischemia in humans. *Ann Neurol*. 1984;16:546-552
9. Astrup J, Siesjo BK, Symon L. Thresholds in cerebral ischemia - the ischemic penumbra. *Stroke*. 1981;12:723-725
10. Baron JC. Perfusion thresholds in human cerebral ischemia: Historical perspective and therapeutic implications. *Cerebrovasc Dis*. 2001;11 Suppl 1:2-8
11. Fisher M. The ischemic penumbra: Identification, evolution and treatment concepts. *Cerebrovasc Dis*. 2004;17 Suppl 1:1-6
12. Heiss WD. Ischemic penumbra: Evidence from functional imaging in man. *J Cereb Blood Flow Metab*. 2000;20:1276-1293
13. Nighoghossian N. Imagerie de la pénombre au cours de l'ischémie cérébrale : Évolution des concepts. Correspondances en neurologie vasculaire. 2005;Vol (V) 2:24-28
14. Guadagno JV, Calautti C, Baron JC. Progress in imaging stroke: Emerging clinical applications. *Br Med Bull*. 2003;65:145-157

15. Furlan M, Marchal G, Viader F, Derlon JM, Baron JC. Spontaneous neurological recovery after stroke and the fate of the ischemic penumbra. *Ann Neurol*. 1996;40:216-226

16. Heiss WD, Sobesky J, Hesselmann V. Identifying thresholds for penumbra and irreversible tissue damage. *Stroke*. 2004;35:2671-2674

17. Baird AE, Warach S. Magnetic resonance imaging of acute stroke. *J Cereb Blood Flow Metab*. 1998;18:583-609

18. Darby DG, Barber PA, Gerraty RP, Desmond PM, Yang Q, Parsons M, Li T, Tress BM, Davis SM. Pathophysiological topography of acute ischemia by combined diffusion-weighted and perfusion mri. *Stroke*. 1999;30:2043-2052

19. Baird AE, Benfield A, Schlaug G, Siewert B, Lovblad KO, Edelman RR, Warach S. Enlargement of human cerebral ischemic lesion volumes measured by diffusion-weighted magnetic resonance imaging. *Ann Neurol*. 1997;41:581-589

20. Jansen O, Schellinger P, Fiebach J, Hacke W, Sartor K. Early recanalisation in acute ischaemic stroke saves tissue at risk defined by mri. *Lancet*. 1999;353:2036-2037

21. Kidwell CS, Saver JL, Starkman S, Duckwiler G, Jahan R, Vespa P, Villablanca JP, Liebeskind DS, Gobin YP, Vinuela F, Alger JR. Late secondary ischemic injury in patients receiving intraarterial thrombolysis. *Ann Neurol*. 2002;52:698-703

22. Schlaug G, Benfield A, Baird AE, Siewert B, Lovblad KO, Parker RA, Edelman RR, Warach S. The ischemic penumbra: Operationally defined by diffusion and perfusion mri. *Neurology*. 1999;53:1528-1537

23. Stejskal E, JE. T. Spin diffusion measurements : Spin echoes in the presence of a time-dependent field gradient. *J Chem Phys*. 1965;42:288-292.

24. Hjort N, Christensen S, Solling C, Ashkanian M, Wu O, Rohl L, Gyldensted C, Andersen G, Ostergaard L. Ischemic injury detected by diffusion imaging 11 minutes after stroke. *Ann Neurol*. 2005;58:462-465

25. Moseley ME, Wendland MF, Kucharczyk J. Magnetic resonance imaging of diffusion and perfusion. *Top Magn Reson Imaging*. 1991;3:50-67

26. Kidwell CS, Alger JR, Saver JL. Beyond mismatch: Evolving paradigms in imaging the ischemic penumbra with multimodal magnetic resonance imaging. *Stroke*. 2003;34:2729-2735

27. Fisher M. Is penumbral imaging useful for extending the treatment window for intravenous tissue plasminogen activator? *Ann Neurol*. 2006;60:499-501

28. Friedlander RM. Apoptosis and caspases in neurodegenerative diseases. *N Engl J Med*. 2003;348:1365-1375

29. Okada H, Mak TW. Pathways of apoptotic and non-apoptotic death in tumour cells. *Nat Rev Cancer*. 2004;4:592-603

30. Smale G, Nichols NR, Brady DR, Finch CE, Horton WE, Jr. Evidence for apoptotic cell death in alzheimer's disease. *Exp Neurol*. 1995;133:225-230

31. Troost D, Aten J, Morsink F, de Jong JM. Apoptosis in amyotrophic lateral sclerosis is not restricted to motor neurons. Bcl-2 expression is increased in unaffected post-central gyrus. *Neuropathol Appl Neurobiol*. 1995;21:498-504

32. Ferrer I. Apoptosis: Future targets for neuroprotective strategies. *Cerebrovasc Dis*. 2006;21 Suppl 2:9-20

33. Han BH, Xu D, Choi J, Han Y, Xanthoudakis S, Roy S, Tam J, Vaillancourt J, Colucci J, Siman R, Giroux A, Robertson GS, Zamboni R, Nicholson DW, Holtzman DM. Selective, reversible caspase-3 inhibitor is neuroprotective and reveals distinct pathways of cell death after neonatal hypoxic-ischemic brain injury. *J Biol Chem*. 2002;277:30128-30136

34. Sussman B, Fitch T. Thrombolysis with fibrinolysin in cerebral arterial occlusion. *J Am Med Assoc*. 1958;167(14):1705-1709

35. Meretoja A, Tatlisumak T. Thrombolytic therapy in acute ischemic stroke - basic concepts. *Curr Vasc Pharmacol*. 2006;4:31-44

36. Hacke W, Kaste M, Bluhmki E, Brozman M, Davalos A, Guidetti D, Larrue V, Lees KR, Medeghri Z, Machnig T, Schneider D, von Kummer R, Wahlgren N, Toni D. Thrombolysis with alteplase 3 to 4.5 hours after acute ischemic stroke. *N Engl J Med*. 2008;359:1317-1329

37. Wardlaw JM, Murray V, Berge E, Del Zoppo GJ. Thrombolysis for acute ischaemic stroke. *Cochrane Database Syst Rev*. 2009:CD000213

38. Tissue plasminogen activator for acute ischemic stroke. The national institute of neurological disorders and stroke rt-pa stroke study group. *N Engl J Med*. 1995;333:1581-1587

39. Kaur J, Zhao Z, Klein GM, Lo EH, Buchan AM. The neurotoxicity of tissue plasminogen activator? *J Cereb Blood Flow Metab*. 2004;24:945-963

40. Hill MD, Buchan AM. Methodology for the canadian activase for stroke effectiveness study (cases). Cases investigators. *Can J Neurol Sci*. 2001;28:232-238

41. Albers GW, Atkinson RP, Kelley RE, Rosenbaum DM. Safety, tolerability, and pharmacokinetics of the n-methyl-d-aspartate antagonist dextrorphan in patients with acute stroke. Dextrorphan study group. *Stroke*. 1995;26:254-258

42. Emsley HC, Smith CJ, Tyrrell PJ, Hopkins SJ. Inflammation in acute ischemic stroke and its relevance to stroke critical care. *Neurocrit Care*. 2008;9:125-138

43. Clark WM, Lessov N, Lauten JD, Hazel K. Doxycycline treatment reduces ischemic brain damage in transient middle cerebral artery occlusion in the rat. *J Mol Neurosci*. 1997;9:103-108

44. Andes D, Craig WA. Animal model pharmacokinetics and pharmacodynamics: A critical review. *Int J Antimicrob Agents*. 2002;19:261-268

45. Planas AM, Traystman RJ. Advances in translational medicine 2010. *Stroke*.42:283-284

46. Yrjanheikki J, Tikka T, Keinanen R, Goldsteins G, Chan PH, Koistinaho J. A tetracycline derivative, minocycline, reduces inflammation and protects against focal cerebral ischemia with a wide therapeutic window. *Proc Natl Acad Sci U S A*. 1999;96:13496-13500

47. Wang CX, Yang T, Shuaib A. Effects of minocycline alone and in combination with mild hypothermia in embolic stroke. *Brain Res*. 2003;963:327-329

48. Xu L, Fagan SC, Waller JL, Edwards D, Borlongan CV, Zheng J, Hill WD, Feuerstein G, Hess DC. Low dose intravenous minocycline is neuroprotective after middle cerebral artery occlusion-reperfusion in rats. *BMC Neurol*. 2004;4:7

49. Morimoto N, Shimazawa M, Yamashima T, Nagai H, Hara H. Minocycline inhibits oxidative stress and decreases in vitro and in vivo ischemic neuronal damage. *Brain Res*. 2005;1044:8-15

50. Koistinaho M, Malm TM, Kettunen MI, Goldsteins G, Starckx S, Kauppinen RA, Opdenakker G, Koistinaho J. Minocycline protects against permanent cerebral ischemia in wild type but not in matrix metalloprotease-9-deficient mice. *J Cereb Blood Flow Metab*. 2005;25:460-467

51. Tang XN, Wang Q, Koike MA, Cheng D, Goris ML, Blankenberg FG, Yenari MA. Monitoring the protective effects of minocycline treatment with radiolabeled annexin v in an experimental model of focal cerebral ischemia. *J Nucl Med*. 2007;48:1822-1828

52. Murata Y, Rosell A, Scannevin RH, Rhodes KJ, Wang X, Lo EH. Extension of the thrombolytic time window with minocycline in experimental stroke. *Stroke*. 2008;39:3372-3377

53. Machado LS, Sazonova IY, Kozak A, Wiley DC, El-Remessy AB, Ergul A, Hess DC, Waller JL, Fagan SC. Minocycline and tissue-type plasminogen activator for stroke: Assessment of interaction potential. *Stroke*. 2009;40:3028-3033

54. Kim BJ, Kim MJ, Park JM, Lee SH, Kim YJ, Ryu S, Kim YH, Yoon BW. Reduced neurogenesis after suppressed inflammation by minocycline in transient cerebral ischemia in rat. *J Neurol Sci*. 2009;279:70-75

55. Matsukawa N, Yasuhara T, Hara K, Xu L, Maki M, Yu G, Kaneko Y, Ojika K, Hess DC, Borlongan CV. Therapeutic targets and limits of minocycline neuroprotection in experimental ischemic stroke. *BMC Neurosci*. 2009;10:126

56. Martin A, Boisgard R, Kassiou M, Dolle F, Tavitian B. Reduced pbr/tspo expression after minocycline treatment in a rat model of focal cerebral ischemia: A pet study using [(18)f]dpa-714. *Mol Imaging Biol*. 2010

57. Chu LS, Fang SH, Zhou Y, Yin YJ, Chen WY, Li JH, Sun J, Wang ML, Zhang WP, Wei EQ. Minocycline inhibits 5-lipoxygenase expression and accelerates functional recovery in chronic phase of focal cerebral ischemia in rats. *Life Sci*. 2010;86:170-177

58. Gordon S, Taylor PR. Monocyte and macrophage heterogeneity. *Nat Rev Immunol*. 2005;5:953-964

59. Gehrmann J, Matsumoto Y, Kreutzberg GW. Microglia: Intrinsic immuneffector cell of the brain. *Brain Res Brain Res Rev*. 1995;20:269-287

60. Aloisi F. Immune function of microglia. *Glia*. 2001;36:165-179

61. Raivich G, Bohatschek M, Kloss CU, Werner A, Jones LL, Kreutzberg GW. Neuroglial activation repertoire in the injured brain: Graded response, molecular mechanisms and cues to physiological function. *Brain Res Brain Res Rev*. 1999;30:77-105

62. Papadopoulos V, Baraldi M, Guilarte TR, Knudsen TB, Lacapere JJ, Lindemann P, Norenberg MD, Nutt D, Weizman A, Zhang MR, Gavish M. Translocator protein

(18kda): New nomenclature for the peripheral-type benzodiazepine receptor based on its structure and molecular function. *Trends Pharmacol Sci*. 2006;27:402-409

63. Iadecola C, Alexander M. Cerebral ischemia and inflammation. *Curr Opin Neurol*. 2001;14:89-94

64. Ekdahl CT, Kokaia Z, Lindvall O. Brain inflammation and adult neurogenesis: The dual role of microglia. *Neuroscience*. 2009;158:1021-1029

65. Petty MA, Wettstein JG. Elements of cerebral microvascular ischaemia. *Brain Res Brain Res Rev*. 2001;36:23-34

66. Wang Q, Tang XN, Yenari MA. The inflammatory response in stroke. *J Neuroimmunol*. 2007;184:53-68

67. Gelderblom M, Leypoldt F, Steinbach K, Behrens D, Choe CU, Siler DA, Arumugam TV, Orthey E, Gerloff C, Tolosa E, Magnus T. Temporal and spatial dynamics of cerebral immune cell accumulation in stroke. *Stroke*. 2009;40:1849-1857

68. Iadecola C, Ross ME. Molecular pathology of cerebral ischemia: Delayed gene expression and strategies for neuroprotection. *Ann N Y Acad Sci*. 1997;835:203-217

69. Danton GH, Dietrich WD. Inflammatory mechanisms after ischemia and stroke. *J Neuropathol Exp Neurol*. 2003;62:127-136

70. Price CJ, Warburton EA, Menon DK. Human cellular inflammation in the pathology of acute cerebral ischaemia. *J Neurol Neurosurg Psychiatry*. 2003;74:1476-1484

71. Gong C, Qin Z, Betz AL, Liu XH, Yang GY. Cellular localization of tumor necrosis factor alpha following focal cerebral ischemia in mice. *Brain Res*. 1998;801:1-8

72. Huang J, Upadhyay UM, Tamargo RJ. Inflammation in stroke and focal cerebral ischemia. *Surg Neurol*. 2006;66:232-245

73. Allan SM, Rothwell NJ. Cytokines and acute neurodegeneration. *Nat Rev Neurosci*. 2001;2:734-744

74. Um JY, Moon KS, Lee KM, Yun JM, Cho KH, Moon BS, Kim HM. Association of interleukin-1 alpha gene polymorphism with cerebral infarction. *Brain Res Mol Brain Res*. 2003;115:50-54

75. Yoshimoto T, Houkin K, Tada M, Abe H. Induction of cytokines, chemokines and adhesion molecule mrna in a rat forebrain reperfusion model. *Acta Neuropathol*. 1997;93:154-158

76. Liu T, Clark RK, McDonnell PC, Young PR, White RF, Barone FC, Feuerstein GZ. Tumor necrosis factor-alpha expression in ischemic neurons. *Stroke*. 1994;25:1481-1488

77. Offner H, Vandenbark AA, Hurn PD. Effect of experimental stroke on peripheral immunity: Cns ischemia induces profound immunosuppression. *Neuroscience*. 2009;158:1098-1111

78. Barone FC, Arvin B, White RF, Miller A, Webb CL, Willette RN, Lysko PG, Feuerstein GZ. Tumor necrosis factor-alpha. A mediator of focal ischemic brain injury. *Stroke*. 1997;28:1233-1244

79. Wang X, Yue TL, Young PR, Barone FC, Feuerstein GZ. Expression of interleukin-6, c-fos, and zif268 mrnas in rat ischemic cortex. *J Cereb Blood Flow Metab*. 1995;15:166-171

80. Strle K, Zhou JH, Shen WH, Broussard SR, Johnson RW, Freund GG, Dantzer R, Kelley KW. Interleukin-10 in the brain. *Crit Rev Immunol*. 2001;21:427-449

81. Liesz A, Suri-Payer E, Veltkamp C, Doerr H, Sommer C, Rivest S, Giese T, Veltkamp R. Regulatory t cells are key cerebroprotective immunomodulators in acute experimental stroke. *Nat Med*. 2009;15:192-199

82. Wiessner C, Gehrmann J, Lindholm D, Topper R, Kreutzberg GW, Hossmann KA. Expression of transforming growth factor-beta 1 and interleukin-1 beta mrna in rat brain following transient forebrain ischemia. *Acta Neuropathol*. 1993;86:439-446

83. Lehrmann E, Kiefer R, Finsen B, Diemer NH, Zimmer J, Hartung HP. Cytokines in cerebral ischemia: Expression of transforming growth factor beta-1 (tgf-beta 1) mrna in the postischemic adult rat hippocampus. *Exp Neurol*. 1995;131:114-123

84. Pang L, Ye W, Che XM, Roessler BJ, Betz AL, Yang GY. Reduction of inflammatory response in the mouse brain with adenoviral-mediated transforming growth factor-ss1 expression. *Stroke*. 2001;32:544-552

85. Gourmala NG, Buttini M, Limonta S, Sauter A, Boddeke HW. Differential and time-dependent expression of monocyte chemoattractant protein-1 mrna by astrocytes and macrophages in rat brain: Effects of ischemia and peripheral lipopolysaccharide administration. *J Neuroimmunol*. 1997;74:35-44

86. Minami M, Satoh M. Chemokines and their receptors in the brain: Pathophysiological roles in ischemic brain injury. *Life Sci*. 2003;74:321-327

87. Schilling M, Strecker JK, Schabitz WR, Ringelstein EB, Kiefer R. Effects of monocyte chemoattractant protein 1 on blood-borne cell recruitment after transient focal cerebral ischemia in mice. *Neuroscience*. 2009;161:806-812

88. Zhang R, Chopp M, Zhang Z, Jiang N, Powers C. The expression of p- and e-selectins in three models of middle cerebral artery occlusion. *Brain Res*. 1998;785:207-214

89. Okada Y, Copeland BR, Mori E, Tung MM, Thomas WS, del Zoppo GJ. P-selectin and intercellular adhesion molecule-1 expression after focal brain ischemia and reperfusion. *Stroke*. 1994;25:202-211

90. Suzuki H, Abe K, Tojo S, Kimura K, Mizugaki M, Itoyama Y. A change of p-selectin immunoreactivity in rat brain after transient and permanent middle cerebral artery occlusion. *Neurol Res*. 1998;20:463-469

91. del Zoppo GJ. Inflammation and the neurovascular unit in the setting of focal cerebral ischemia. *Neuroscience*. 2009;158:972-982

92. Haring HP, Akamine BS, Habermann R, Koziol JA, Del Zoppo GJ. Distribution of integrin-like immunoreactivity on primate brain microvasculature. *J Neuropathol Exp Neurol*. 1996;55:236-245

93. Huang Z, Huang PL, Panahian N, Dalkara T, Fishman MC, Moskowitz MA. Effects of cerebral ischemia in mice deficient in neuronal nitric oxide synthase. *Science*. 1994;265:1883-1885

94. Iadecola C. Bright and dark sides of nitric oxide in ischemic brain injury. *Trends Neurosci*. 1997;20:132-139

95. Brouns R, De Deyn PP. The complexity of neurobiological processes in acute ischemic stroke. *Clin Neurol Neurosurg*. 2009;111:483-495

96. Hamann GF, Okada Y, Fitridge R, del Zoppo GJ. Microvascular basal lamina antigens disappear during cerebral ischemia and reperfusion. *Stroke*. 1995;26:2120-2126

97. Belayev L, Busto R, Zhao W, Ginsberg MD. Quantitative evaluation of blood-brain barrier permeability following middle cerebral artery occlusion in rats. *Brain Res*. 1996;739:88-96

98. Kastrup A, Engelhorn T, Beaulieu C, de Crespigny A, Moseley ME. Dynamics of cerebral injury, perfusion, and blood-brain barrier changes after temporary and permanent middle cerebral artery occlusion in the rat. *J Neurol Sci*. 1999;166:91-99

99. Zhang Z, Chopp M, Powers C. Temporal profile of microglial response following transient (2 h) middle cerebral artery occlusion. *Brain Res*. 1997;744:189-198

100. Schroeter M, Jander S, Huitinga I, Witte OW, Stoll G. Phagocytic response in photochemically induced infarction of rat cerebral cortex. The role of resident microglia. *Stroke*. 1997;28:382-386

101. Rupalla K, Allegrini PR, Sauer D, Wiessner C. Time course of microglia activation and apoptosis in various brain regions after permanent focal cerebral ischemia in mice. *Acta Neuropathol*. 1998;96:172-178

102. van Rossum D, Hanisch UK. Microglia. *Metab Brain Dis*. 2004;19:393-411

103. Vila N, Reverter JC, Yague J, Chamorro A. Interaction between interleukin-6 and the natural anticoagulant system in acute stroke. *J Interferon Cytokine Res*. 2000;20:325-329

104. Relton JK, Martin D, Thompson RC, Russell DA. Peripheral administration of interleukin-1 receptor antagonist inhibits brain damage after focal cerebral ischemia in the rat. *Exp Neurol*. 1996;138:206-213

105. Lai AY, Todd KG. Microglia in cerebral ischemia: Molecular actions and interactions. *Can J Physiol Pharmacol*. 2006;84:49-59

106. Clark WM, Rinker LG, Lessov NS, Hazel K, Hill JK, Stenzel-Poore M, Eckenstein F. Lack of interleukin-6 expression is not protective against focal central nervous system ischemia. *Stroke*. 2000;31:1715-1720

107. Giulian D, Vaca K, Corpuz M. Brain glia release factors with opposing actions upon neuronal survival. *J Neurosci*. 1993;13:29-37

108. Block ML, Zecca L, Hong JS. Microglia-mediated neurotoxicity: Uncovering the molecular mechanisms. *Nat Rev Neurosci*. 2007;8:57-69

109. Kaushal V, Schlichter LC. Mechanisms of microglia-mediated neurotoxicity in a new model of the stroke penumbra. *J Neurosci*. 2008;28:2221-2230

110. Yrjanheikki J, Keinanen R, Pellikka M, Hokfelt T, Koistinaho J. Tetracyclines inhibit microglial activation and are neuroprotective in global brain ischemia. *Proc Natl Acad Sci U S A*. 1998;95:15769-15774

111. Yenari MA, Xu L, Tang XN, Qiao Y, Giffard RG. Microglia potentiate damage to blood-brain barrier constituents: Improvement by minocycline in vivo and in vitro. *Stroke*. 2006;37:1087-1093

112. Hanisch UK, Kettenmann H. Microglia: Active sensor and versatile effector cells in the normal and pathologic brain. *Nat Neurosci*. 2007;10:1387-1394

113. Lalancette-Hebert M, Gowing G, Simard A, Weng YC, Kriz J. Selective ablation of proliferating microglial cells exacerbates ischemic injury in the brain. *J Neurosci*. 2007;27:2596-2605

114. Denes A, Vidyasagar R, Feng J, Narvainen J, McColl BW, Kauppinen RA, Allan SM. Proliferating resident microglia after focal cerebral ischaemia in mice. *J Cereb Blood Flow Metab*. 2007;27:1941-1953

115. Weston RM, Jones NM, Jarrott B, Callaway JK. Inflammatory cell infiltration after endothelin-1-induced cerebral ischemia: Histochemical and myeloperoxidase correlation with temporal changes in brain injury. *J Cereb Blood Flow Metab*. 2007;27:100-114

116. Wake H, Moorhouse AJ, Jinno S, Kohsaka S, Nabekura J. Resting microglia directly monitor the functional state of synapses in vivo and determine the fate of ischemic terminals. *J Neurosci*. 2009;29:3974-3980

117. Ishibashi M, Tanabe Y, Miyoshi H, Matusue E, Kaminou T, Ogawa T. Intrathoracic splenosis: Evaluation by superparamagnetic iron oxide-enhanced magnetic resonance imaging and radionuclide scintigraphy. *Jpn J Radiol*. 2009;27:371-374

118. Daldrup-Link HE, Mohanty A, Cuenod C, Pichler B, Link T. New perspectives on bone marrow contrast agents and molecular imaging. *Semin Musculoskelet Radiol*. 2009;13:145-156

119. Nakai G, Matsuki M, Harada T, Tanigawa N, Yamada T, Barentsz J, Narumi Y. Evaluation of axillary lymph nodes by diffusion-weighted mri using ultrasmall superparamagnetic iron oxide in patients with breast cancer: Initial clinical experience. *J Magn Reson Imaging*.

120. Howarth SP, Tang TY, Trivedi R, Weerakkody R, J UK-I, Gaunt ME, Boyle JR, Li ZY, Miller SR, Graves MJ, Gillard JH. Utility of uspio-enhanced mr imaging to identify inflammation and the fibrous cap: A comparison of symptomatic and asymptomatic individuals. *Eur J Radiol*. 2009;70:555-560

121. Ito A, Shinkai M, Honda H, Kobayashi T. Medical application of functionalized magnetic nanoparticles. *J Biosci Bioeng*. 2005;100:1-11

122. Corot C, Petry KG, Trivedi R, Saleh A, Jonkmanns C, Le Bas JF, Blezer E, Rausch M, Brochet B, Foster-Gareau P, Baleriaux D, Gaillard S, Dousset V. Macrophage imaging in central nervous system and in carotid atherosclerotic plaque using ultrasmall superparamagnetic iron oxide in magnetic resonance imaging. *Invest Radiol*. 2004;39:619-625

123. Corot C, Robert P, Idee JM, Port M. Recent advances in iron oxide nanocrystal technology for medical imaging. *Adv Drug Deliv Rev*. 2006;58:1471-1504

124. Di Marco M, Sadun C, Port M, Guilbert I, Couvreur P, Dubernet C. Physicochemical characterization of ultrasmall superparamagnetic iron oxide particles (uspio) for biomedical application as mri contrast agents. *Int J Nanomedicine*. 2007;2:609-622

125. Laurent S, Bridot JL, Elst LV, Muller RN. Magnetic iron oxide nanoparticles for biomedical applications. *Future Med Chem*.2:427-449

126. Thorek DL, Weisshaar CL, Czupryna JC, Winkelstein BA, Tsourkas A. Superparamagnetic iron oxide-enhanced magnetic resonance imaging of neuroinflammation in a rat model of radicular pain. *Mol Imaging*.10:206-214

127. Taupitz M, Schnorr J, Abramjuk C, Wagner S, Pilgrimm H, Hunigen H, Hamm B. New generation of monomer-stabilized very small superparamagnetic iron oxide particles (vsop) as contrast medium for mr angiography: Preclinical results in rats and rabbits. *J Magn Reson Imaging*. 2000;12:905-911

128. Sun R, Dittrich J, Le-Huu M, Mueller MM, Bedke J, Kartenbeck J, Lehmann WD, Krueger R, Bock M, Huss R, Seliger C, Grone HJ, Misselwitz B, Semmler W, Kiessling F. Physical and biological characterization of superparamagnetic iron oxide- and ultrasmall superparamagnetic iron oxide-labeled cells: A comparison. *Invest Radiol*. 2005;40:504-513

129. Raynal I, Prigent P, Peyramaure S, Najid A, Rebuzzi C, Corot C. Macrophage endocytosis of superparamagnetic iron oxide nanoparticles: Mechanisms and comparison of ferumoxides and ferumoxtran-10. *Invest Radiol*. 2004;39:56-63

130. Metz S, Bonaterra G, Rudelius M, Settles M, Rummeny EJ, Daldrup-Link HE. Capacity of human monocytes to phagocytose approved iron oxide mr contrast agents in vitro. *Eur Radiol*. 2004;14:1851-1858

131. Taupitz M, Wagner S, Schnorr J, Kravec I, Pilgrimm H, Bergmann-Fritsch H, Hamm B. Phase i clinical evaluation of citrate-coated monocrystalline very small superparamagnetic iron oxide particles as a new contrast medium for magnetic resonance imaging. *Invest Radiol*. 2004;39:394-405

132. Wagner S, Schnorr J, Pilgrimm H, Hamm B, Taupitz M. Monomer-coated very small superparamagnetic iron oxide particles as contrast medium for magnetic resonance imaging: Preclinical in vivo characterization. *Invest Radiol*. 2002;37:167-177

133. Shapiro EM, Sharer K, Skrtic S, Koretsky AP. In vivo detection of single cells by mri. *Magn Reson Med*. 2006;55:242-249

134. Shapiro EM, Skrtic S, Koretsky AP. Sizing it up: Cellular mri using micron-sized iron oxide particles. *Magn Reson Med*. 2005;53:329-338

135. Shapiro EM, Skrtic S, Sharer K, Hill JM, Dunbar CE, Koretsky AP. Mri detection of single particles for cellular imaging. *Proc Natl Acad Sci U S A*. 2004;101:10901-10906

136. Weissleder R, Elizondo G, Wittenberg J, Lee AS, Josephson L, Brady TJ. Ultrasmall superparamagnetic iron oxide: An intravenous contrast agent for assessing lymph nodes with mr imaging. *Radiology*. 1990;175:494-498

137. Laurent S, Forge D, Port M, Roch A, Robic C, Vander Elst L, Muller RN. Magnetic iron oxide nanoparticles: Synthesis, stabilization, vectorization, physicochemical characterizations, and biological applications. *Chem Rev*. 2008;108:2064-2110

138. Modo M, JWM. B. Molecular and cellular mr imaging: Taylor & francis group, llc, 2007.

139. Jung CW, Jacobs P. Physical and chemical properties of superparamagnetic iron oxide mr contrast agents: Ferumoxides, ferumoxtran, ferumoxsil. *Magn Reson Imaging*. 1995;13:661-674

140. Bourrinet P, Bengele HH, Bonnemain B, Dencausse A, Idee JM, Jacobs PM, Lewis JM. Preclinical safety and pharmacokinetic profile of ferumoxtran-10, an ultrasmall superparamagnetic iron oxide magnetic resonance contrast agent. *Invest Radiol*. 2006;41:313-324

141. Kalish H, Arbab AS, Miller BR, Lewis BK, Zywicke HA, Bulte JW, Bryant LH, Jr., Frank JA. Combination of transfection agents and magnetic resonance contrast agents for cellular imaging: Relationship between relaxivities, electrostatic forces, and chemical composition. *Magn Reson Med*. 2003;50:275-282

142. Muller K, Skepper JN, Posfai M, Trivedi R, Howarth S, Corot C, Lancelot E, Thompson PW, Brown AP, Gillard JH. Effect of ultrasmall superparamagnetic iron oxide nanoparticles (ferumoxtran-10) on human monocyte-macrophages in vitro. *Biomaterials*. 2007;28:1629-1642

143. Billotey C, Wilhelm C, Devaud M, Bacri JC, Bittoun J, Gazeau F. Cell internalization of anionic maghemite nanoparticles: Quantitative effect on magnetic resonance imaging. *Magn Reson Med*. 2003;49:646-654

144. Wilhelm C, Gazeau F. Universal cell labelling with anionic magnetic nanoparticles. *Biomaterials*. 2008;29:3161-3174

145. Schulze E, Ferrucci JT, Jr., Poss K, Lapointe L, Bogdanova A, Weissleder R. Cellular uptake and trafficking of a prototypical magnetic iron oxide label in vitro. *Invest Radiol*. 1995;30:604-610

146. Gaasch JA, Lockman PR, Geldenhuys WJ, Allen DD, Van der Schyf CJ. Brain iron toxicity: Differential responses of astrocytes, neurons, and endothelial cells. *Neurochem Res*. 2007;32:1196-1208

147. Lauffer RB. Paramagnetic metal complexes as water proton relaxation agents for nmr imaging: Theory and design. *Chem Rev*. 1987;87:901-927

148. Bjornerud A, Johansson L. The utility of superparamagnetic contrast agents in mri: Theoretical consideration and applications in the cardiovascular system. *NMR Biomed*. 2004;17:465-477

149. Simon GH, Bauer J, Saborovski O, Fu Y, Corot C, Wendland MF, Daldrup-Link HE. T1 and t2 relaxivity of intracellular and extracellular uspio at 1.5t and 3t clinical mr scanning. *Eur Radiol*. 2006;16:738-745

150. Gref R, Minamitake Y, Peracchia MT, Trubetskoy V, Torchilin V, Langer R. Biodegradable long-circulating polymeric nanospheres. *Science*. 1994;263:1600-1603

151. Moghimi SM, Hunter AC. Recognition by macrophages and liver cells of opsonized phospholipid vesicles and phospholipid headgroups. *Pharm Res*. 2001;18:1-8

152. Gaur U, Sahoo SK, De TK, Ghosh PC, Maitra A, Ghosh PK. Biodistribution of fluoresceinated dextran using novel nanoparticles evading reticuloendothelial system. *Int J Pharm*. 2000;202:1-10

153. Lacava LM, Lacava ZG, Da Silva MF, Silva O, Chaves SB, Azevedo RB, Pelegrini F, Gansau C, Buske N, Sabolovic D, Morais PC. Magnetic resonance of a dextran-coated magnetic fluid intravenously administered in mice. *Biophys J*. 2001;80:2483-2486

154. Liu W, Frank JA. Detection and quantification of magnetically labeled cells by cellular mri. *Eur J Radiol*. 2009;70:258-264

155. Bowen CV, Zhang X, Saab G, Gareau PJ, Rutt BK. Application of the static dephasing regime theory to superparamagnetic iron-oxide loaded cells. *Magn Reson Med*. 2002;48:52-61

156. Doerfler A, Engelhorn T, Heiland S, Knauth M, Wanke I, Forsting M. Mr contrast agents in acute experimental cerebral ischemia: Potential adverse impacts on neurologic outcome and infarction size. *J Magn Reson Imaging*. 2000;11:418-424

157. Rausch M, Sauter A, Frohlich J, Neubacher U, Radu EW, Rudin M. Dynamic patterns of uspio enhancement can be observed in macrophages after ischemic brain damage. *Magn Reson Med*. 2001;46:1018-1022

158. Kleinschnitz C, Bendszus M, Frank M, Solymosi L, Toyka KV, Stoll G. In vivo monitoring of macrophage infiltration in experimental ischemic brain lesions by magnetic resonance imaging. *J Cereb Blood Flow Metab*. 2003;23:1356-1361

159. Schroeter M, Saleh A, Wiedermann D, Hoehn M, Jander S. Histochemical detection of ultrasmall superparamagnetic iron oxide (uspio) contrast medium uptake in experimental brain ischemia. *Magn Reson Med*. 2004;52:403-406

160. Saleh A, Schroeter M, Jonkmanns C, Hartung HP, Modder U, Jander S. In vivo mri of brain inflammation in human ischaemic stroke. *Brain*. 2004;127:1670-1677

161. Kleinschnitz C, Schutz A, Nolte I, Horn T, Frank M, Solymosi L, Stoll G, Bendszus M. In vivo detection of developing vessel occlusion in photothrombotic ischemic brain lesions in the rat by iron particle enhanced mri. *J Cereb Blood Flow Metab*. 2005;25:1548-1555

162. Engberink RD, Blezer EL, Hoff EI, van der Pol SM, van der Toorn A, Dijkhuizen RM, de Vries HE. Mri of monocyte infiltration in an animal model of neuroinflammation using spio-labeled monocytes or free uspio. *J Cereb Blood Flow Metab*. 2008;28:841-851

163. Wiart M, Davoust N, Pialat JB, Desestret V, Moucharaffie S, Cho TH, Mutin M, Langlois JB, Beuf O, Honnorat J, Nighoghossian N, Berthezene Y. Mri monitoring of neuroinflammation in mouse focal ischemia. *Stroke*. 2007;38:131-137

164. Desestret V, Brisset JC, Moucharrafie S, Devillard E, Nataf S, Honnorat J, Nighoghossian N, Berthezene Y, Wiart M. Early-stage investigations of ultrasmall superparamagnetic iron oxide-induced signal change after permanent middle cerebral artery occlusion in mice. *Stroke*. 2009;40:1834-1841

165. Rausch M, Baumann D, Neubacher U, Rudin M. In-vivo visualization of phagocytotic cells in rat brains after transient ischemia by uspio. *NMR Biomed*. 2002;15:278-283

166. Wiart M, Davoust N, Pialat JB, Desestret V, Moucharrafie S, Cho TH, Mutin M, Langlois JB, Beuf O, Honnorat J, Nighoghossian N, Berthezene Y. Mri monitoring of neuroinflammation in mouse focal ischemia. *Stroke*. 2007;38:131-137

167. Kim J, Kim DI, Lee SK, Kim DJ, Lee JE, Ahn SK. Imaging of the inflammatory response in reperfusion injury after transient cerebral ischemia in rats: Correlation of superparamagnetic iron oxide-enhanced magnetic resonance imaging with histopathology. *Acta Radiol*. 2008;49:580-588

168. Henning EC, Ruetzler CA, Gaudinski MR, Hu TC, Latour LL, Hallenbeck JM, Warach S. Feridex preloading permits tracking of cns-resident macrophages after transient middle cerebral artery occlusion. *J Cereb Blood Flow Metab*. 2009;29:1229-1239

169. Farr TD, Seehafer JU, Nelles M, Hoehn M. Challenges towards mr imaging of the peripheral inflammatory response in the subacute and chronic stages of transient focal ischemia. *NMR Biomed*.

170. Saleh A, Schroeter M, Jonkmanns C, Hartung HP, Modder U, Jander S. In vivo mri of brain inflammation in human ischaemic stroke. *Brain*. 2004;127:1670-1677.

171. Nighoghossian N, Wiart M, Cakmak S, Berthezene Y, Derex L, Cho TH, Nemoz C, Chapuis F, Tisserand GL, Pialat JB, Trouillas P, Froment JC, Hermier M. Inflammatory response after ischemic stroke: A uspio-enhanced mri study in patients. *Stroke*. 2007;38:303-307

172. Saleh A, Schroeter M, Ringelstein A, Hartung HP, Siebler M, Modder U, Jander S. Iron oxide particle-enhanced mri suggests variability of brain inflammation at early stages after ischemic stroke. *Stroke*. 2007;38:2733-2737

173. Cho TH, Nighoghossian N, Wiart M, Desestret V, Cakmak S, Berthezene Y, Derex L, Louis-Tisserand G, Honnorat J, Froment JC, Hermier M. Uspio-enhanced mri of neuroinflammation at the sub-acute stage of ischemic stroke: Preliminary data. *Cerebrovasc Dis*. 2007;24:544-546

174. Villa C, Erratico S, Razini P, Fiori F, Rustichelli F, Torrente Y, Belicchi M. Stem cell tracking by nanotechnologies. *Int J Mol Sci*.11:1070-1081, 2010

175. Giuliani A, Frati C, Rossini A, Komlev VS, Lagrasta C, Savi M, Cavalli S, Gaetano C, Quaini F, Manescu A, Rustichelli F. High-resolution x-ray microtomography for three-dimensional imaging of cardiac progenitor cell homing in infarcted rat hearts. *J Tissue Eng Regen Med*.5:e168-178, 2011

176. Betz O, Wegst U, Weide D, Heethoff M, Helfen L, Lee WK, Cloetens P. Imaging applications of synchrotron x-ray phase-contrast microtomography in biological morphology and biomaterials science. I. General aspects of the technique and its advantages in the analysis of millimetre-sized arthropod structure. *J Microsc*. 2007;227:51-71

177. CLOETENS P., PATEYRON-SALOME M., BUFFIERE J.Y, PEIX G., BARUCHEL J., PEYRIN F., M. S. Observation of microstructure and damage in materials by phase sensitive radiography and tomography. *Journal of Applied Physics*. 1997;vol 81:p. 5878-5886

178. LANGER M., CLOETENS P., GUIGAY J.P., PEYRIN F. Quantitative comparison of direct phase retrieval algorithms in in-line phase tomography,. *Med Phys*. 2008;vol 35:pp. 4556- 4566

179. P. Cloetens, W. Ludwig, J. Baruchel, D. Van Dyck, J. Van Landuyt, J. P. Guigay, M. Schlenker, , . "holotomography: Quantitative phase tomography with micrometer

resolution using hard synchrotron radiation x rays,". *Appl Phys Lett,*. 1999;vol. 75:pp. 2912–2914

180. Weitkamp T, David C, Bunk O, Bruder J, Cloetens P, Pfeiffer F. X-ray phase radiography and tomography of soft tissue using grating interferometry. *Eur J Radiol*. 2008;68:S13-17

181. Gutierrez L, Quintana C, Patino C, Bueno J, Coppin H, Roth MP, Lazaro FJ. Iron speciation study in hfe knockout mice tissues: Magnetic and ultrastructural characterisation. *Biochim Biophys Acta*. 2009;1792:541-547

182. Levy M, Wilhelm C, Luciani N, Deveaux V, Gendron F, Luciani A, Devaud M, Gazeau F. Nanomagnetism reveals the intracellular clustering of iron oxide nanoparticles in the organism. *Nanoscale*.3:4402-4410

183. Krumeich F. Properties of electrons, their interactions with matter and applications in electron microscopy.

184. Voutou B. Electron microscopy: The basics.

185. Dirnagl U, Iadecola C, Moskowitz MA. Pathobiology of ischaemic stroke: An integrated view. *Trends Neurosci*. 1999;22:391-397

186. Durukan A, Tatlisumak T. Acute ischemic stroke: Overview of major experimental rodent models, pathophysiology, and therapy of focal cerebral ischemia. *Pharmacol Biochem Behav*. 2007;87:179-197

187. Chauveau F, Cho TH, Berthezene Y, Nighoghossian N, Wiart M. Imaging inflammation in stroke using magnetic resonance imaging. *Int J Clin Pharmacol Ther*. 2011;48:718-728

188. Emsley HC, Tyrrell PJ. Inflammation and infection in clinical stroke. *J Cereb Blood Flow Metab*. 2002;22:1399-1419

189. Chauveau F, Moucharrafie S, Wiart M, Brisset JC, Berthezene Y, Nighoghossian N, Cho TH. In vivo mri assessment of permanent middle cerebral artery occlusion by electrocoagulation: Pitfalls of procedure. *Exp Transl Stroke Med*. 2011;2:4

190. Pialat JB, Cho TH, Beuf O, Joye E, Moucharaffie S, Langlois JB, Nemoz C, Janier M, Berthezene Y, Nighoghossian N, Desvergne B, Wiart M. Mri monitoring of focal cerebral ischemia in peroxisome proliferator-activated receptor (ppar)-deficient mice. *NMR Biomed*. 2007;20:335-342

191. Homsi S, Federico F, Croci N, Palmier B, Plotkine M, Marchand-Leroux C, Jafarian-Tehrani M. Minocycline effects on cerebral edema: Relations with inflammatory and oxidative stress markers following traumatic brain injury in mice. *Brain Res*. 2009;1291:122-132

192. Rausch M, Sauter A, Frohlich J, Neubacher U, Radu EW, Rudin M. Dynamic patterns of uspio enhancement can be observed in macrophages after ischemic brain damage. *Magn Reson Med*. 2001;46:1018-1022.

193. Franklin. The mouse brain in stereotaxic coordinates. *San Diego, Calif:Academic Press*

1997

194. Brisset JC, Sigovan M, Chauveau F, Riou A, Devillard E, Desestret V, Touret M, Nataf S, Honnorat J, Canet-Soulas E, Nighoghossian N, Berthezene Y, Wiart M.

Quantification of iron-labeled cells with positive contrast in mouse brains. *Mol Imaging Biol*. 2011;13:672-678

195. Fisher M, Feuerstein G, Howells DW, Hurn PD, Kent TA, Savitz SI, Lo EH. Update of the stroke therapy academic industry roundtable preclinical recommendations. *Stroke*. 2009;40:2244-2250

196. Fagan SC, Waller JL, Nichols FT, Edwards DJ, Pettigrew LC, Clark WM, Hall CE, Switzer JA, Ergul A, Hess DC. Minocycline to improve neurologic outcome in stroke (minos): A dose-finding study. *Stroke*. 2010;41:2283-2287

197. Wiart M, Curiel L, Gelet A, Lyonnet D, Chapelon JY, Rouviere O. Influence of perfusion on high-intensity focused ultrasound prostate ablation: A first-pass mri study. *Magn Reson Med*. 2007;58:119-127

198. Rausch M, Baumann D, Neubacher U, Rudin M. In-vivo visualization of phagocytotic cells in rat brains after transient ischemia by uspio. *NMR Biomed*. 2002;15:278-283.

199. Stroh A, Zimmer C, Werner N, Gertz K, Weir K, Kronenberg G, Steinbrink J, Mueller S, Sieland K, Dirnagl U, Nickenig G, Endres M. Tracking of systemically administered mononuclear cells in the ischemic brain by high-field magnetic resonance imaging. *Neuroimage*. 2006;33:886-897

200. Brisset JC, Desestret V, Marcellino S, Devillard E, Chauveau F, Lagarde F, Nataf S, Nighoghossian N, Berthezene Y, Wiart M. Quantitative effects of cell internalization of two types of ultrasmall superparamagnetic iron oxide nanoparticles at 4.7t and 7t. *European Radiology*. 2009; (in press)

201. Sigovan M, Boussel L, Sulaiman A, Sappey-Marinier D, Alsaid H, Desbleds-Mansard C, Ibarrola D, Gamondes D, Corot C, Lancelot E, Raynaud JS, Vives V, Lacledere C, Violas X, Douek PC, Canet-Soulas E. Rapid-clearance iron nanoparticles for inflammation imaging of atherosclerotic plaque: Initial experience in animal model. *Radiology*. 2009;252:401-409

202. Fisher M, Davalos A, Rogalewski A, Schneider A, Ringelstein EB, Schabitz WR. Toward a multimodal neuroprotective treatment of stroke. *Stroke*. 2006;37:1129-1136

203. Brisset JC, Sigovan M, Chauveau F, Riou A, Devillard E, Desestret V, Touret M, Nataf S, Honnorat J, Canet-Soulas E, Nighoghossian N, Berthezene Y, Wiart M. Quantification of iron-labeled cells with positive contrast in mouse brains. *Mol Imaging Biol*.13:672-678

204. Adam JF, Nemoz C, Bravin A, Fiedler S, Bayat S, Monfraix S, Berruyer G, Charvet AM, Le Bas JF, Elleaume H, Esteve F. High-resolution blood-brain barrier permeability and blood volume imaging using quantitative synchrotron radiation computed tomography: Study on an f98 rat brain glioma. *J Cereb Blood Flow Metab*. 2005;25:145-153

205. Salome M, Peyrin F, Cloetens P, Odet C, Laval-Jeantet AM, Baruchel J, Spanne P. A synchrotron radiation microtomography system for the analysis of trabecular bone samples. *Med Phys*. 1999;26:2194-2204

206. Bousson V, Peyrin F, Bergot C, Hausard M, Sautet A, Laredo JD. Cortical bone in the human femoral neck: Three-dimensional appearance and porosity using synchrotron radiation. *J Bone Miner Res*. 2004;19:794-801

207. Larrue A, Rattner A, Peter ZA, Olivier C, Laroche N, Vico L, Peyrin F. Synchrotron radiation micro-ct at the micrometer scale for the analysis of the three-dimensional morphology of microcracks in human trabecular bone. *PLoS One*.6:e21297

208. Langer M, Liu Y, Tortelli F, Cloetens P, Cancedda R, Peyrin F. Regularized phase tomography enables study of mineralized and unmineralized tissue in porous bone scaffold. *J Microsc*.238:230-239

209. Lu W, Dong Z, Liu Z, Fu W, Peng Y, Chen S, Xiao T, Xie H, Du G, Deng B, Zhang X. Detection of microvasculature in rat hind limb using synchrotron radiation. *J Surg Res*.164:e193-199

210. Jensen TH, Bech M, Bunk O, Menzel A, Bouchet A, Le Duc G, Feidenhans'l R, Pfeiffer F. Molecular x-ray computed tomography of myelin in a rat brain. *Neuroimage*.57:124-129

211. Giuliani A, Frati C, Rossini A, Komlev VS, Lagrasta C, Savi M, Cavalli S, Gaetano C, Quaini F, Manescu A, Rustichelli F. High-resolution x-ray microtomography for three-dimensional imaging of cardiac progenitor cell homing in infarcted rat hearts. *J Tissue Eng Regen Med*. 2011;5:e168-178

212. Torrente Y, Gavina M, Belicchi M, Fiori F, Komlev V, Bresolin N, Rustichelli F. High-resolution x-ray microtomography for three-dimensional visualization of human stem cell muscle homing. *FEBS Lett*. 2006;580:5759-5764

213. Brunke O, Odenbach S, Fritsche C, Hilger I, Kaiser WA. Determination of magnetic particle distribution in biomedical applications by x-ray microtomography. *Journal of Magnetism and Magnetic Materials*. 2005;289:428-430

214. Brisset JC, Desestret V, Marcellino S, Devillard E, Chauveau F, Lagarde F, Nataf S, Nighoghossian N, Berthezene Y, Wiart M. Quantitative effects of cell internalization of two types of ultrasmall superparamagnetic iron oxide nanoparticles at 4.7 t and 7 t. *Eur Radiol*.20:275-285

215. Wilhelm C, Billotey C, Roger J, Pons JN, Bacri JC, Gazeau F. Intracellular uptake of anionic superparamagnetic nanoparticles as a function of their surface coating. *Biomaterials*. 2003;24:1001-1011

216. Paganin D, Mayo SC, Gureyev TE, Miller PR, Wilkins SW. Simultaneous phase and amplitude extraction from a single defocused image of a homogeneous object. *J Microsc*. 2002;206:33-40

217. Dejus RJ, Sanchez del Rio M. Xop: A graphical user interface for spectral calculations and x-ray optics utilities. *Rev Sci Instrum*. 1996;Vol. 67, p. 3356

218. Frindel C, Robini M, Schaerer J, Croisille P, Zhu YM. A graph-based approach for automatic cardiac tractography. *Magn Reson Med*. 2010;64:1215-1229

Publications and Communications

Articles in journals

1. Monitoring minocycline therapy in experimental stroke using USPIO-enhanced MRI

M. Marinescu, A. Durand, F. Chauveau, A. Dencausse, A. Riou, N. Nighoghossian, M. Wiart and Y. Berthezène - Submitted to Radiology

2. Detection of iron oxide nanoparticles in the brain using synchrotron radiation X-ray micro-computed tomography – in preparation (Molecular Imaging and Biology)

M. Marinescu, M. Langer, C. Olivier, F. Peyrin, F. Chauveau, A. Riou, A. Durand, Y. Berthezène, M. Wiart

3. MRI assessment of intra-carotid route for macrophage delivery after transient cerebral ischemia.

Riou A, Chauveau F, Cho TH, **Marinescu M**, Nataf S, Berthezène Y, Nighoghossian N, Wiart M. Submitted to European Radiology.

4. Suivi par IRM de macrophages marqués et étude de la biotransformation cellulaire de l'agent de contraste.

A. Riou, **M. Marinescu**, F. Chauveau, T.-H. Cho, M.-G. Blanchin, S. Nataf, N. Nighoghossian , M. Wiart, Y. Berthezène. IRBM 2011 April; 32 (2):126-129.

Book chapter

MRI assessment of post-ischemic neuroinflammation in stroke: experimental and clinical studies

Chauveau Fabien, **Marinescu Marilena**, Cho Tae-Hee, Wiart Marlène, Berthezène Yves, Nighoghossian Norbert , Neuroimaging / Book 1. Edited by Intech; 2011

Conference Proceedings

1. Monitoring minocycline therapy in experimental stroke using USPIO-enhanced MRI

M. Marinescu, A. Durand, F. Chauveau, A. Dencausse, A. Riou, N. Nighoghossian, M. Wiart and Y. Berthezène.

WMIC, San Diego, USA, September 2011(Travel award) [P]

2. Treatment with bone marrow-derived alternatively activated (M2) macrophages after transient ischemia: A USPIO-Enhanced longitudinal MRI study in rats

A. Riou, F. Chauveau, T. H. Cho, M. Marinescu, S. Nataf, C. Remy, E. Barbier, N. Nighoghossian, M. Wiart, Y. Berthezène

WMIC, San Diego, USA. September 2011 (Travel award) [P]

3. MRI monitoring of intra-arterial delivery of bone marrow-derived macrophages after transient ischemia

A. Riou, F. Chauveau, T. H. Cho, **M. Marinescu**, S. Nataf, Y. Berthezène, N. Nighoghossian, and M. Wiart,

World Molecular Imaging Congress, Kyoto, Japan, 8-10 September, 2010. [P]

4. Monitoring stroke therapy using magnetic resonance imaging in the mouse brain

M. Marinescu, A. Durand, A. Riou, F. Chauveau, N. Nighoghossian, M. Wiart, Y. Berthèzene

RITS, Rennes, France April 2011. [P]

5. Biotransformation study of iron oxide contrast agents used for MRI of inflammation

M. Marinescu, VA Maraloiu, M. Hillenkamp, A. Tamion, A. Hillion, V. Dupuis, Y. Berthezene, M. Wiart, MG Blanchin.

Transalp'Nano, Como, Italy, June 2010. [O]

6. MRI study of intra-arterial bone marrow-derived macrophage administration after acute focal ischemic stroke in rats

A. Riou, F. Chauveau, T. H. Cho, M. Marinescu, S. Nataf, Y. Berthezène, N. Nighoghossian, and M. Wiart, "",

5th European Molecular Imaging Meeting, Warsaw, Poland, May, 2010 [O]

Curriculum Vitae



Marilena Ioana MARINESCU

EDUCATION and RESEARCH ACTIVITIES

2012 – 2014	**Post doctoral position within Neurology department of University of Massachussets Medical School, Worcester, Massachusetts, USA**
Oct 2008 – 2011	PhD**, Lyon 1 University, Creatis-LRMN Laboratory, Bron, France** Subject: "Multi-modal characterisation of superparamagnetic iron oxide nanoparticles used as contrast agents in MRI of an ischemic stroke mouse model." Activities: MRI of ischemic stroke mouse model, histology on ex-vivo mouse brain tissue, MR and TEM characterization of contrast agents; X-Ray imaging using synchrotron radiation
June 2011	**University Diploma** "Animal experiments, level 1: Training course on animal models for biological and medical research and technologies for animal care and housing", Lyon 1 University, France.
Sep 2009 – Aug 2010	Master of Science**, Lyon 1 University, France** **Genetics and cell biology Department, Option: Microstructure Imaging** **Coursework focusing on different microscopy techniques (confocal microscopy, scanning and transmission electron microscopy) for imaging micro and nanostructures; biological tissue preparation techniques for TEM visualization** **Internship work on: characterization by TEM of mouse spleen samples obtained at different time points after the administration of an iron oxide based MR contrast agent. The purpose was to monitor iron particles agglomeration and biotransformation in the spleen.**
Mar 2008 – Jul 2008	Erasmus – Socrates Program **Internship at the Lyon 1 University, LPMCN Laboratory, France** **Work on characterization by TEM of mouse aortic arch samples obtained at different time points after the administration of an iron oxide based MR contrast agent. The purpose was 2-folded: 1) to determine the nature of the atherosclerosis plaque and 2) to characterize iron particles inside inflammatory cells present in atherosclerosis lesions.** **Supervisor: PhD. Marie Genevieve Blanchin**
Sep 2003 – Jul 2008	Diploma degree**, Politechnique University, Romania,** **Biomedical Department** **Majors: Medical Engineering** **Thesis: "Atherosclerosis plaque characterization by MRI and TEM"**

SKILLS

MRI **high field, small animal imaging, quantitative image analysis, contrast agents, biomarker**

Transmission and Scanning Electron Microscopy

Immunohistochemical analysis

References

Yves BERTHEZENE, PhD Professor
E-mail : yves.berthezene@chu.fr

Marlène Wiart, PhD
E-mail: marlene.wiart@creatis.univ-lyon1.fr

Marie - Geneviève BLANCHIN, research director
E-mail: blanchin@lpmcn.univ-lyon1.fr